
Attosecond Physics in Strong-Field Photoemission from Metal Nanotips

Michael Krüger



München 2013

Attosecond Physics in Strong-Field Photoemission from Metal Nanotips

Michael Krüger

Dissertation
an der Fakultät für Physik
der Ludwig-Maximilians-Universität
München

vorgelegt von
Michael Krüger
aus Burghausen

München, den 30. August 2013

Erstgutachter: Prof. Dr. P. Hommelhoff

Zweitgutachter: Prof. Dr. A. Scrinzi

Tag der mündlichen Prüfung: 4. Oktober 2013

Na chwałę Boga

*Albowiem Bóg, Ten, który rozkazał ciemnościom,
by zajaśniały światłem, zabłysnął w naszych sercach,
by olśnić nas jasnością poznania chwały Bożej
na obliczu Chrystusa.*

2 Kor 4,6

Zusammenfassung

Diese Arbeit befasst sich mit der Untersuchung von Rekollision und Attosekundendynamik in Elektronenemission aus einem Metall, genauer gesagt aus einer scharfen Metallspitze. Spektral aufgelöste Messungen von Photoelektronen, die durch Wenig-Zyklus-Laserpulse erzeugt werden, weisen das Auftreten von Rückstreuung, Materiewelleninterferenz und Elektronendynamik auf der Attosekundenzeitskala an der Spitze nach. Rückgestreute Elektronen werden in einer ersten Anwendung der beobachteten Prozesse dazu benutzt, um nanooptische Effekte an Metallspitzen zu untersuchen.

In unserem Experiment werden Laserpulse aus einem Titan:Saphir-Oszillator mit einer Pulslänge von 6 fs auf eine scharfe Wolframspitze fokussiert, um Elektronen aus dem Metall auszulösen. Das optische Feld wird dabei am scharfen Ende der Spitze verstärkt und ermöglicht somit lokale Lichtintensitäten auf der Größenordnung von $10^{13} \text{ W cm}^{-2}$. Messungen mit spektraler Auflösung zeigen, dass Mehrphotonenprozesse (im weiteren Sinn) zur Emission führen, welche sich in Elektronenspektren in klar aufgelösten Maxima niederschlagen. Bei steigender Lichtintensität beobachten wir die Unterdrückung des Maximums bei der niedrigsten Energie und eine Verschiebung der spektralen Maxima hin zu niedriger Energie. Diese Effekte, die im dynamischen Starkeffekt begründet sind, zeigen an, dass das Starkfeldregime in unserem Photoemissionsexperiment erreicht wurde. Außerdem beobachten wir elastische Rückstreuung: Ausgelöste Elektronen werden vom Laserfeld zurück zur Oberfläche der Spitze getrieben und kollidieren mit dieser; dabei werden Elektronen elastisch an der Oberfläche gestreut und schließlich bei hohen kinetischen Energien detektiert. Dies führt zur Ausbildung einer plateauartigen Struktur im Elektronenspektrum. Wir beschreiben Theoriemodelle, die diese Interpretation unserer experimentellen Ergebnisse untermauern. Elektronen, die rückgestreut werden, sind sehr empfindlich auf die räumliche und zeitliche Struktur des verstärkten Nahfelds an der Spitze. Wir wenden daher Rückstreuung dazu an, die Stärke des Nahfelds an Spitzen verschiedener Größe und Materialien auszumessen.

Rückstreuung ist von Natur aus ein Effekt, der sich auf der Zeitskala von Attosekunden abspielt. Laserpulse mit kontrollierter Träger-Einhüllenden-Phase werden verwendet, um die zeitliche Dynamik dieses Prozesses zu studieren. Phasenaufgelöste Messungen zeigen, dass der Phasenwert der Pulse die maximale kinetische Energie der Elektronen bestimmt und damit als extrem schneller Schalter für hochenergetische Elektronen fungiert. Außerdem wird der Kontrast der Maxima im Plateaubereich des Elektronenspektrums stark von der Phase beeinflusst. Diese Beobachtung stellt das Ergebnis eines Interferenzexperiments mit Materiewellen dar: Ein zeitlicher Doppelspalt führt zu Interferenzstrukturen in der Energie, nämlich den erwähnten Maxima, während ein Einfachspalt diese nicht zulässt und ein breites Kontinuum resultiert. Die zeitliche Form des Pulses gibt mit Attosekundenpräzision vor, welcher Fall vorliegt. Unsere Untersuchung zeigt, dass der Einzugsbereich der Attosekundenphysik, die üblicherweise mit Atomen und Molekülen in der Gasphase untersucht wird, auch auf Nanostrukturen aus Metall erweitert werden kann.

Abstract

This work is concerned with the first observation and investigation of electron recollision and attosecond dynamics in photoemission from a metal, specifically from a sharp metallic nanotip. Spectrally resolved measurements demonstrate electron rescattering, matter-wave interference effects and attosecond control of electron motion in few-cycle laser driven photoemission. As a first application, rescattered electrons were used as a probe to investigate nano-optical field enhancement effects at tips.

In our experiment, 6-fs laser pulses from a Titanium:sapphire laser oscillator are focused on a sharp tungsten nanotip and induce electron emission. The optical field is strongly enhanced at the tip apex and allows for high local intensities on the order of $10^{13} \text{ W cm}^{-2}$. Spectral measurements reveal above-threshold photoemission with clearly resolved multiphoton peaks. At increasing intensity we observe the suppression of the lowest order peak and a shift of the spectral peaks to lower energy. These effects are caused by the AC Stark shift and indicate that the strong-field photoemission regime has been reached in our system. Furthermore, we observe electron recollision and elastic rescattering. Photoelectrons are driven back to the tip surface by the laser field and recollide there. Elastic scattering takes place and leads to high kinetic energies, resulting in a plateau structure in photoelectron spectra. We present theory models that support this notion. Rescattered electrons are sensitive to the spatial and temporal shape of the enhanced nano-optical near-field at the tip. In a first application, we use rescattering to measure the strength of the near-field at tips of different size and material.

The natural time scale of the rescattering process is the attosecond time scale. Carrier-envelope phase stable laser pulses are employed to study its temporal dynamics. Phase-resolved measurements show that the phase of the pulses determines the maximum kinetic energy of photoelectrons and serves as an ultrafast switch for high-energy electrons. Moreover, the contrast of the peaks in the plateau is strongly modulated with the phase. This observation is the result of a matter-wave interference experiment: A temporal single slit or a double slit leads to absence or presence of spectral interference in the energy domain, respectively. In the case of a single slit, a broad spectral continuum results. The temporal shape of the pulse determines with attosecond precision if rescattered electrons are generated during one or two optical cycles. Our investigation shows that attosecond science – usually performed with atomic and molecular gases – can be extended to metal nanostructures.

Contents

Zusammenfassung	vii
Abstract	ix
1 Introduction	3
2 Theory of strong-field photoemission from metal nanotips	9
2.1 Mechanisms of strong-field photoemission from metal surfaces	9
2.1.1 Multiphoton photoemission	10
2.1.2 The Keldysh theory and light-induced tunneling	10
2.1.3 Above-Threshold Photoemission and strong-field effects	13
2.1.4 Other photoemission mechanisms	16
2.2 Electron recollision and the Three-Step Model	18
2.3 Quantum Orbit Theory of recollision	22
2.3.1 The strong-field approximation	22
2.3.2 Saddle-point approximation and quantum orbits	26
2.3.3 Spectral formation and quantum interference	30
2.3.4 Extended Three-Step Model	35
2.4 Numerical approaches	42
2.4.1 Integration of the time-dependent Schrödinger equation	42
2.4.2 Time-dependent density functional theory	44
2.5 Enhanced optical near-fields at nanotips	46
3 Experimental methods and setup	51
3.1 Optical setup	51
3.2 Vacuum chamber and detection system	55
3.3 Metal nanotip preparation and characterization	57
3.3.1 Nanotip fabrication	57
3.3.2 Field emission	61
3.3.3 In-situ tip characterization methods	62
4 Strong-field above-threshold photoemission from nanotips	69
4.1 Above-threshold photoemission	69
4.2 Strong-field effects: Peak suppression and peak shifting	72
5 Electron rescattering at nanotips	75
5.1 Electron rescattering in strong light fields and static fields	75
5.1.1 Rescattering plateau and high-energy cut-off	75
5.1.2 Comparison with theory models	78

5.1.3	Influence of a static electric field	83
5.1.4	Efficiency of rescattering at a metal surface	84
5.2	Probing of optical near-fields by electron rescattering	86
6	Attosecond control of electrons with the carrier-envelope phase	91
6.1	Phase effects in rescattering	92
6.1.1	Carrier-envelope phase sensing	94
6.2	Attosecond double-slit experiment	95
6.2.1	Carrier-envelope phase spectral interferometry	98
6.3	Attosecond control of electron motion	99
6.4	Comparison with theory models	100
7	Conclusion and outlook	105
	References	109
	Danksagung	125

1 Introduction

The atomic nature of matter has always been a fascinating subject of scientists throughout the centuries. People generally associate with atoms the attribute “small”, but “small” does not only refer to size, but also to time: In Bohr’s famous model of the hydrogen atom [1], it takes an electron 152 attoseconds for one cycle on its orbit around the nucleus ($1 \text{ attosecond} = 1 \text{ as} = 10^{-18} \text{ s}$). The same time scale also governs elementary processes in solid materials. In the first half of the 20th century quantum mechanics brought about a satisfying theoretical understanding of atoms. However, it was beyond imagination that direct measurements of electronic processes in atoms or even solids could be undertaken with attosecond resolution.

The advent of attosecond science [2, 3] changed this perspective. With the help of new light sources, namely high-intensity pulsed laser systems, light-matter interaction could be confined to the natural time scale of electron dynamics in matter. Fundamental to attosecond science is the *recollision mechanism* [4, 5], illustrated in Fig. 1.1: An atom is ionized in a strong laser field and the liberated electron is subsequently driven back to the parent ion after the laser field has changed its sign. It then recollides with the ion core at high velocity. The recollision itself is limited to a small fraction of the optical cycle duration, which translates into several hundred attoseconds for near-infrared light. Upon recollision, several processes can take place within this small time frame. The most prominent among them is high-harmonic generation (HHG) [5, 6, 7], caused by recombination of the electron with the ion and the emission of a high-energy photon.

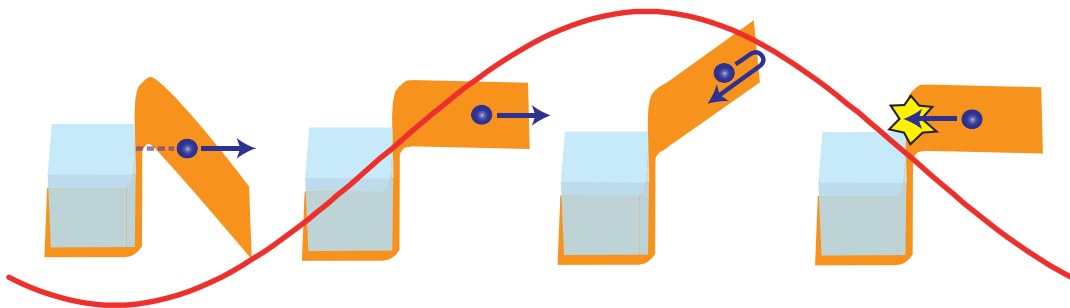


Figure 1.1: Illustration of the recollision mechanism. Recollision is the fundamental effect of attosecond science: A photoelectron (blue) is photoemitted from the parent matter (here from a metal surface) and propagates under the influence of the laser field (red). When the laser field changes sign, the electron returns to the parent matter and recollides with it. Recollision leads to a variety of effects that take place on an attosecond time scale.

Recollision inherently a quantum mechanical process, but is nicely captured by the notion of the electron as a classical point-like particle driven by the laser electric field. The process can be influenced by shaping the waveform of the driving laser pulse. A straightforward way for pulse shaping is controlling the carrier-envelope (CE) phase of

laser pulses, i.e., the phase difference between carrier wave and pulse envelope. Experimentally, the stabilization and control of the CE phase became possible through the successful implementation of the frequency comb [8], a finding that was rewarded with the Nobel Prize for Theodor W. Hänsch and John L. Hall. Shortly thereafter, the control of HHG with the CE phase of laser pulses was demonstrated [9] and applied to generate single isolated attosecond pulses [10, 11]. Attosecond bursts of extreme ultraviolet radiation, with record durations down to 67 as [12], were produced with the help of attosecond dynamics inherent to atomic systems and subsequently used to investigate these dynamics in other systems and settings. Among these investigations was the first direct measurement of electron tunneling from an ionic gas [13] and the timing of the photoelectric effect at a metal surface [14] and at an atomic gas [15], the latter with an unprecedented time resolution of $\sim\pm 5$ as.

Another effect that can take place upon recollision is rescattering. Here the liberated electron scatters elastically with the ionic core and subsequently gains high kinetic energy in the laser field. In photoelectron spectra rescattering manifests itself in a high-energy plateau, a spectral region where the electron count rate stays approximately constant with increasing energy [16, 17]. Both HHG optical spectra and rescattering photoelectron spectra contain encoded information about the temporal dynamics of the recollision mechanism and the structure of the involved matter. Different quantum paths to a given final state in the time domain add up coherently, causing interference in the spectral domain. This fact has been used, for example, by Shafir *et al.* [18] who were able to measure the time when an electron leaves the tunneling barrier in a beautiful experiment based on HHG. Even without employing single isolated attosecond pulses, attosecond dynamics in a wide range of systems can be readily observed due to the coherence that characterizes recollision.

This work is concerned with recollision and attosecond physics at a nanoscale solid-state system. Usually attosecond science is performed with atomic or molecular gases. In contrast, the work presented here extends attosecond science to nanometer-scale electron emitters. In this thesis, a class of nanoemitters was chosen that is well known and thoroughly understood already for decades, namely sharp metal tips. The field of surface science started with the nanotip-based experiments of Erwin W. Müller in the 1930s, who deduced surface properties from field emission patterns [19]. In 1955, he and Kanwar Bahadur were the first to image single atoms on a surface of a metal tip with the field ion microscope [20, 21]. With this new method observation and control of the surface structure became possible on an atomic level. Ubiquitous today are the scanning tunnel microscope (STM) [22], the atomic force microscope (AFM) [23] and the scanning near-field microscope (SNOM) [24], all based on nanoscale structures as probes. The latter technique combines the extremely small size of a nanotip with light fields, localizing the optical field to the length scale of the tip apex (typically ~ 10 nm). The localized optical field (or near-field) at a sharp tip is strongly enhanced. The associated research field of nano-optics [25] aims to push temporal and spatial resolution of optical microscopy to their respective limits. More than a decade ago researchers started to look into the intriguing possibility to combine tips and ultrashort laser pulses in order to add femtosecond time resolution to STM [26]. Another premise of this combination is the creation of a laser-triggered source of ultrashort electron pulses [27]. Among other

applications, this source was envisioned to enable electron interferometry with controlled timing, nanometric imaging and carrier-envelope phase detection [28, 29, 30]. A tip-based photoelectron source was successfully used to demonstrate the absence of a force in the magnetic Aharonov-Bohm effect [31].

In this work, sharp metal tips are irradiated with few-cycle laser pulses in order to explore strong-field photoemission and attosecond physics at solid surfaces (see Fig. 1.2). The presented experiment combines established methods from the fields of strong-field physics, attosecond science, nano-optics and surface science. Due to the near-field enhancement effect at the tips, an enhanced intensity on the order of $10^{13} \text{ W cm}^{-2}$ can be attained with moderate intensities from a laser oscillator. Under the influence of 6-fs laser pulses at 800 nm center wavelength, above-threshold photoemission was observed with clearly resolved photon orders [32]. Peak suppression and peak shifting could be demonstrated with spectrally resolved photoemission measurements at these high intensities. These effects provide clear evidence that a strong-field regime of photoemission has been reached.

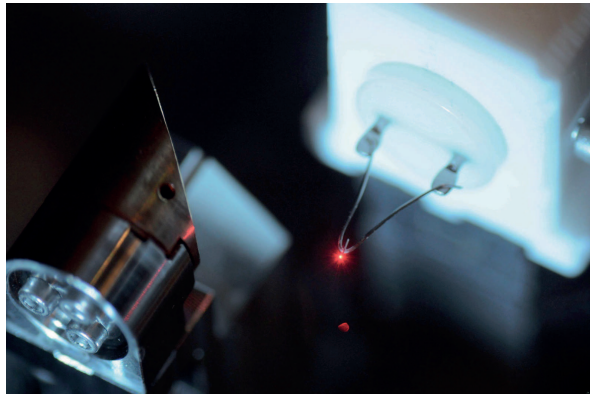


Figure 1.2: Illustration of the experiment. A sharp metal tip is irradiated with near-infrared few-cycle laser pulses. The light is focused by an off-axis parabolic mirror (left) on the tip placed at the end of the v-shaped wire. Courtesy of Th. Naeser.

A high-energy plateau structure was found in photoelectron spectra, a clear sign of the presence of rescattering and recollision [33, 34]. Photoelectrons scatter elastically off the tip surface just as in the atomic case, but here demonstrated at a metal nanostructure for the first time. Theory models from atomic physics [35] as well as a more appropriate solid-state model [34] confirm this notion and allow quantitative modeling of the experiment. Despite its complex solid-state nature, photoemission from nanotips constitutes a model system for strong-field physics [36].

Rescattering is sensitive to the spatial properties of the near-field. By measuring electron spectra for different intensities and hence electron excursion lengths it is possible to determine the spatial field distribution at a nano-structure with a resolution of 1 nm [37]. As a first demonstration, we determine the strength of the optical near-field generated by tips of different size and material and compare the results to a numerical solution of Maxwell's equations. Using rescattered electrons as a probe, it should be possible to map out intensity and phase of optical near-fields at nanoemitters.

The door to attosecond physics is opened by employing laser pulses with stable carrier-envelope phase. Changing the carrier-envelope phase strongly affects the spectral shape of the plateau [33]. The contrast of spectral interference peaks in the plateau is modulated with the phase. Rescattered electrons can be generated during one or two optical cycles, resulting in absence or presence of spectral interference. Furthermore, the phase and thus the field determine if high-energy electrons are observed or not. This switch-like behavior indicates that an attosecond field effect transistor is feasible where the optical field switches electron currents on an attosecond time scale. Also carrier-envelope phase sensing is possible using tip-based photoemission [38]. Attosecond science and recollision physics performed directly with solid-state systems has become an experimental reality.

This thesis is organized as follows:

Chapter 1 gives a brief introduction.

Chapter 2 introduces fundamental theory concepts of strong-field photoemission from solid surfaces. After an overview of emission mechanisms, we present models from atomic physics and apply them to surface photoemission. We also describe more realistic numerical approaches that account for effects in a solid-state system and investigate the excitation of optical near-fields at metallic nanotips.

Chapter 3 gives a comprehensive overview of the experimental techniques and the setup employed for the investigation of tip-based strong-field photoemission.

Chapter 4 presents spectral measurements of photoemitted electrons that show that above-threshold photoemission takes place at metal tips. We present unambiguous experimental evidence of strong-field effects.

Chapter 5 is concerned with systematic studies of electron recollision and rescattering at nanotips in experiment and theory. As a first application, recolliding electrons are used to determine the strength of the optical near-field at nanotips.

Chapter 6 explores the attosecond dynamics involved in recollision at metal nanotips. Experimental and theoretical evidence shows clearly that attosecond science can be extended to solid-state systems. Optical-field-controlled interference effects in the spectral domain give precise information on the timing of recollision and photoemission.

Chapter 7 concludes this thesis with an outlook on future developments.

Manuscripts published in peer-reviewed journals and books

- **Strong-field above-threshold photoemission from sharp metal tips**
M. Schenk, M. Krüger and P. Hommelhoff, *Phys. Rev. Lett.* **105**, 257601 (2010).
- **Production of sharp gold tips with high surface quality**
M. Eisele, M. Krüger, M. Schenk, A. Ziegler and P. Hommelhoff, *Rev. Sci. Instr.* **82**, 026101 (2011).
- **Attosecond control of electrons emitted from a nanoscale metal tip**
M. Krüger[†], M. Schenk[†] and P. Hommelhoff, *Nature* **475**, 78–81 (2011).
- **Attosecond physics in photoemission from a metal nanotip**
M. Krüger, M. Schenk, M. Förster and P. Hommelhoff, *J. Phys. B: At. Mol. Opt. Phys.* **45**, 074006 (2012).
- **Electron rescattering at metal nanotips induced by ultrashort laser pulses**
G. Wachter, Ch. Lemell, J. Burgdörfer, M. Schenk, M. Krüger and P. Hommelhoff, *Phys. Rev. B* **86**, 035402 (2012).
- **Interaction of ultrashort laser pulses with metal nanotips: a model system for strong-field phenomena**
M. Krüger, M. Schenk, P. Hommelhoff, G. Wachter, Ch. Lemell and J. Burgdörfer, *New J. Phys.* **14**, 085019 (2012).
- **Field localization and rescattering in tip-based photoemission**
S. V. Yalunin, G. Herink, D. R. Solli, M. Krüger, P. Hommelhoff, M. Diehn, A. Munk and C. Ropers, *Annalen der Physik* **525**, L12–L18 (2013).
- **From Above-Threshold Photoemission to Attosecond Physics at a Nanometric Tungsten Tip**
M. Krüger, M. Schenk, J. Breuer, M. Förster, J. Hammer, J. Hoffrogge, S. Thomas, and P. Hommelhoff, book chapter in *Progress in Ultrafast Intense Laser Science Vol. IX*, edited by K. Yamanouchi and K. Midorikawa (Springer 2013).
- **Two-dimensional spectral interferometry using the carrier-envelope phase**
Ch. Ott, M. Schönwald, Ph. Raith, A. Kaldun, G. Sansone, M. Krüger, P. Hommelhoff, Y. Patil, Y. Zhang, K. Meyer, M. Laux and Th. Pfeifer, *New J. Phys.* **15**, 073031 (2013).
- **Probing of optical near-fields by electron rescattering on the 1 nm scale**
S. Thomas[†], M. Krüger[†], M. Förster, M. Schenk and P. Hommelhoff, *Nano Lett.* **13**, 4790–4794 (2013).

[†]These authors contributed equally.

Manuscripts submitted to peer-reviewed journals

- **A tip-based source of femtosecond electron pulses at 30keV**
J. Hoffrogge, J.-P. Stein, M. Krüger, M. Förster, J. Hammer, D. Ehberger, P. Baum and P. Hommelhoff, *manuscript submitted*, preprint at arXiv:1303.2383 (2013).
- **Ultrashort laser oscillator pulses meet nano-structures: from attosecond physics at metal tips to dielectric laser accelerators**
S. Thomas, M. Krüger, J. Breuer, M. Förster and P. Hommelhoff, *accepted for publication in Proceedings of the XXIst International Conference on Laser Science ICOLS* (2013).

Patent applications

- **Method and device for sensing a carrier envelope characteristic of laser pulses, and applications thereof**
P. Hommelhoff, M. Krüger, M. Schenk, International patent application no. PCT/EP2010/006990 (2010).

2 Theory of strong-field photoemission from metal nanotips

Most of the available literature on strong-field photoemission concentrates on ionization of gas-phase atoms and molecules. This chapter aims to familiarize the reader with theory concepts applicable to photoemission from solids.

2.1 Mechanisms of strong-field photoemission from metal surfaces

Strong-field physics takes place when the force exerted by a light field on a bound electron becomes comparable to the binding force acting on the electron. In this regime, the laser field cannot be simply regarded as a weak perturbation anymore, but gives rise to (highly) nonlinear effects. High-intensity laser light is required to enter the strong-field regime, as a simple example shows: The electric field strength experienced by an electron in the ground state of hydrogen is on the order of 10^{11} GV m⁻¹. In order to match this field strength a light field of enormous intensity of $\sim 10^{16}$ W cm⁻² is required. To give a comparison, sun light focused by a burning glass reaches about 100 W cm⁻².

Using light from the sun, Heinrich Hertz demonstrated in 1886 that ultraviolet light caused an increase of current flow in a spark gap between metal electrodes [39]. It was found later that photoemission of electrons is the nature of the observed effect and that the number of detected photoelectrons linearly increases with light intensity. Albert Einstein could explain the findings with the absorption of single energy quanta of light, called nowadays photons [40]. He proposed the following equation for the maximum kinetic energy of the photoelectrons $E_{\text{kin,max}}$, the so-called law of photoelectric emission:

$$E_{\text{kin,max}} = \hbar\omega - \phi. \quad (2.1)$$

Here \hbar is the reduced Planck constant, ω the (circular) light frequency and ϕ the material work function. A potential barrier with height ϕ has to be overcome in order for an electron to be liberated from the material. Following Einstein's insight, the photoelectric effect demonstrated the particle nature of light and the quantization of energy. A discovery of nonlinear effects in light-matter interaction, however, was out of reach for decades.

The demonstration of the first laser by Theodore H. Maiman in 1960 gave thrust to theoretical and experimental efforts towards strong-field physics. Now nonlinear effects beyond Hertz's and Einstein's photoelectric effect could be discovered, such as two-photon absorption [41] and the two-photon photoelectric effect [42]. The former had been predicted by Maria Göppert-Mayer in her dissertation already in 1931 [43]. Multiphoton

photoemission was established as an experimental reality: Two or more energy quanta are absorbed by the target system, resulting in electron emission. We will now take a closer look at multiphoton photoemission.

2.1.1 Multiphoton photoemission

The fundamental effect of nonlinear photoemission from solid-state materials and atomic gases is multiphoton photoemission (MPP), a process where a number of photons is absorbed quasi-simultaneously. The picture that one can draw is analogous to Einstein's photoelectric effect: n photons are absorbed by the target system and their energy is transferred to an electron, promoting it to a free continuum state (see Fig. 2.1(a)). The process can be described within the framework of time-dependent perturbation theory in the n th order, given that the light field causes only a weak perturbation of the system¹. A simple derivation involving an integration over all possible intermediate states gives the following dependence of the total photoemission rate $P(I)$ on intensity I :

$$P(I) = \sigma_n I^n. \quad (2.2)$$

The photoemission rate follows a power-law dependence, with n the number of photons. σ_n is a proportionality constant, related to the dipole matrix elements involved in the transition and to material properties. Einstein's photoelectric effect simply follows by setting $n = 1$. In the case of a metal surface under irradiation from a continuous wave (cw) light field at grazing incidence, the maximum kinetic energy of a photoelectron released by a multiphoton process of order n is given by

$$E_{\text{kin,max}} = n\hbar\omega - \phi, \quad (2.3)$$

in full analogy to Eq. 2.1. For a pulsed laser field, the resulting spectrum smears out due to the large bandwidth in available photon energies $\hbar\omega$. Multiphoton photoemission can be strongly enhanced if it involves a resonant or near-resonant intermediate state. In this case, step-wise excitation is possible: Population is transferred to an intermediate state and can remain there for a finite time before further excitation. In a metal, many unoccupied states above the Fermi level are found and direct and step-wise transitions compete with each other. Throughout this thesis, however, only non-resonant MPP is considered. Of high importance at low light intensities is the lowest possible order $n = n_{\text{min}}$, the minimum required number of photons in order to overcome the potential barrier. The presented theory approach is therefore called lowest-order perturbation theory (LOPT). The photoemission regime where LOPT can describe the emission mechanism is called multiphoton regime. LOPT naturally breaks down for high light intensities when entering the strong-field regime. We will now introduce the Keldysh theory that provides a sound description of photoemission for a larger range of light intensities and other characteristic parameters.

2.1.2 The Keldysh theory and light-induced tunneling

In 1964 Leonid V. Keldysh pioneered a very successful theory approach [45] that was able to link multiphoton photoemission with another emission mechanism, namely light-

¹For a detailed and rigorous description of multiphoton processes see, e.g., [44].

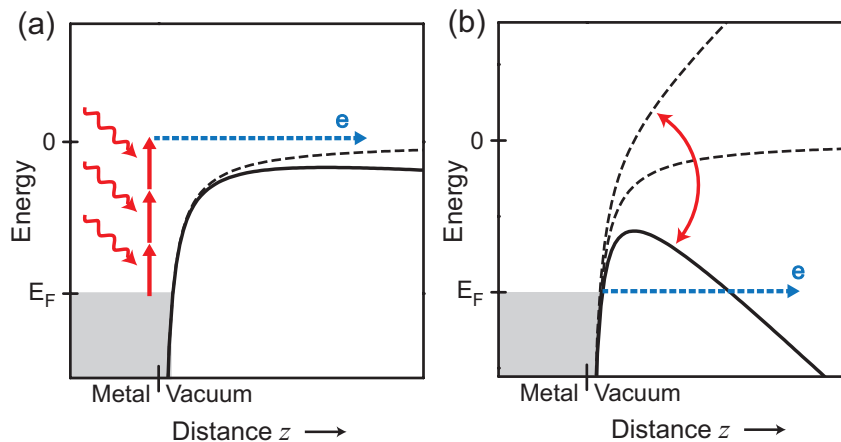


Figure 2.1: Photoemission regimes for a metal surface illustrated in potential energy diagrams. (a) Multiphoton photoemission. Several photons (red) are absorbed by the metal and electrons (blue) are emitted over the potential barrier. The barrier is only weakly perturbed by the light. (b) Light-induced tunneling photoemission. The light field (red) strongly modulates the potential barrier, resulting in a penetrable tunneling barrier for a fraction of the optical cycle duration. Electrons directly tunnel out from the initial state (here the Fermi energy E_F) into the vacuum.

induced tunneling. The theory was originally formulated for the ionization of atoms and band transitions inside solids, but soon extended to photoemission from a metallic surface by Bunkin and Fedorov [46]. Keldysh defined a characteristic parameter γ that separates two limiting regimes, the multiphoton regime ($\gamma \gg 1$) and the tunneling regime ($\gamma \ll 1$) [45]. Light-induced tunneling is also termed optical field emission for metal surfaces. The multiphoton photoemission regime, as introduced in the last subsection, is fully characterized by the photon picture, i.e., the absorption of several photons (see Fig. 2.1(a)). Here the laser field is regarded as a small perturbation. In contrast, the tunneling regime is reached for strong peak electric field strengths and/or small frequencies. The potential is strongly modulated with the light frequency and for a small fraction of the optical cycle duration a penetrable tunneling barrier is formed. According to the tunneling picture, an electron is promoted from its initial state (in the metal or atom) to a free state by a tunneling process (see Fig. 2.1(b) for an illustration).

The Keldysh parameter γ for photoemission from a metal with work function ϕ is defined as

$$\gamma = \sqrt{\frac{\phi}{2U_p}}. \quad (2.4)$$

For the analogous atomic case, ϕ can be replaced with the binding energy I_p of the atomic ground state. The ponderomotive energy U_p is given by

$$U_p = \frac{1}{2}m \langle v(t)^2 \rangle_t = \frac{q^2 E_0^2}{4m\omega^2} \quad (2.5)$$

and corresponds to the mean kinetic energy of a free electron oscillating in a monochromatic cw light field of circular frequency ω and peak electric field E_0 . $q = -|e|$ is the

electron charge, m is the electron mass and $v(t)$ the instantaneous velocity in the laser field; the brackets indicate averaging over one optical cycle. The cycle-averaged light intensity is given by $I = c\epsilon_0 E_0^2/2$, hence the ponderomotive energy scales linearly with intensity. Here c is the vacuum speed of light and ϵ_0 the vacuum permittivity.

A fundamental requirement for the applicability of the theory is low-frequency laser light, i.e., the photon energy E_{phot} has to be much smaller than the work function ϕ (for metal surfaces) or the binding energy I_p (for atoms). The work function of typical metals is typically on the order of 5 eV and therefore laser light in the near-infrared or light of even longer wavelength is required. Decreasing γ in order to enter deeper into the tunneling regime can be achieved by either increasing the intensity or decreasing the carrier frequency. This cannot be done limitlessly because there are validity boundaries to Keldysh-type tunneling theories [47]. For example, the tunneling barrier is suppressed at high laser intensities (barrier suppression regime, [48]) and the initial state cannot be regarded as bound anymore. The Keldysh theory breaks down in this case.

The general photoemission rate given by Keldysh corresponds to a sum of all contributions P_n from different multiphoton orders n : $P \propto \sum_n P_n$. In the original works of Keldysh [45], Bunkin and Fedorov [46], and of Perelomov, Popov and Terent'ev (PPT, [49, 50]), the authors replaced this sum with an integral over the full range of final momenta. Solving this integral yields a momentum-integrated cycle-averaged photoemission rate [45, 46, 49, 51]

$$P(\gamma) \propto \exp \left\{ -\frac{2\phi}{\hbar\omega} \left[\left(1 + \frac{1}{2\gamma^2} \right) \operatorname{arcsinh}\gamma - \frac{\sqrt{1+\gamma^2}}{2\gamma} \right] \right\}, \quad (2.6)$$

here called generalized Keldysh rate, for a monochromatic cw field of amplitude E_0 and frequency ω irradiating a metal surface in grazing incidence. Preexponential factors are omitted here. Replacing the metal work function ϕ with the binding energy I_p yields the atomic case. The defining quantities of Eq. 2.6 are the dimensionless Keldysh parameter γ and the ratio of work function and photon energy $\phi/(\hbar\omega)$. The formula is applicable for all γ . Fig. 2.2 shows the emission rate P as a function of γ for a work function of 4.5 eV and a photon energy of 1.5 eV (wavelength ~ 830 nm).

There are two limiting cases: $\gamma \gg 1$ (for sufficiently small field amplitude and/or large frequency) and $\gamma \ll 1$ (for sufficiently large field amplitude and/or small frequency). It is instructive to determine the rate in these limits from Eq. 2.6. In the original work of Keldysh, this was performed directly from the sum over the multiphoton orders.

For $\gamma \gg 1$ one finds

$$\operatorname{arcsinh}\gamma \approx \ln 2\gamma \Rightarrow P(\gamma) \propto \exp \left(-\frac{2\phi}{\hbar\omega} \ln 2\gamma \right) \propto \left(\frac{1}{2\gamma} \right)^{2\phi/(\hbar\omega)} \propto E_0^{2\phi/(\hbar\omega)}. \quad (2.7)$$

This limit can be identified with the multiphoton photoemission regime. The photocurrent is proportional to $I^{n_{\text{min}}}$, where $n_{\text{min}} = \phi/(\hbar\omega)$ is approximately the number of photons required to overcome the metal work function. Note that n_{min} has a non-integer value here. This is an artefact due to the above-mentioned replacement of the sum with a continuous integral. In the rigorous derivation, n_{min} is given by the minimum required number of photons for photoemission. This is because the lowest-order multiphoton process dominates the count rate, just as the LOPT approach predicts (see Eq. 2.2). The behavior of Eq. 2.7 is displayed in Fig. 2.2.

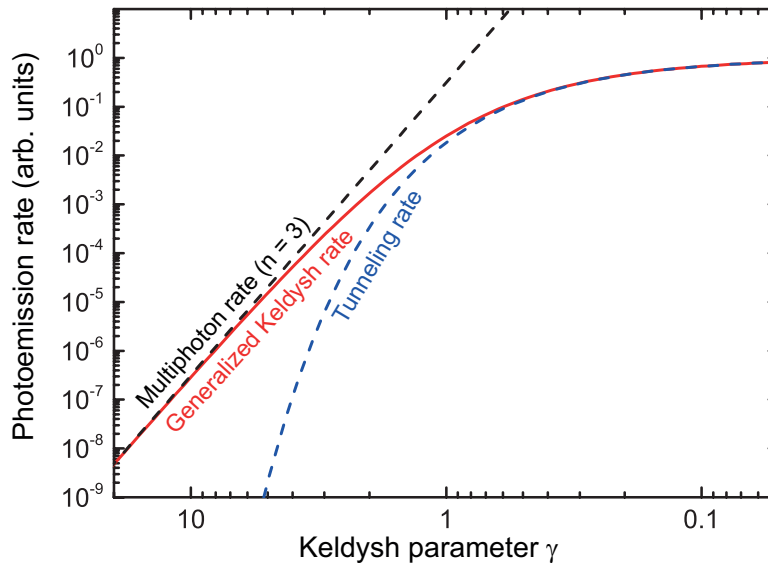


Figure 2.2: Keldysh photoemission rate. The rate given by Keldysh (red curve, Eq. 2.6) is compared to the multiphoton rate (black dashed curve, Eq. 2.2) and the tunneling rate (blue dashed curve, Eq. 2.8). With decreasing γ , i.e., increasing light intensity, the Keldysh rate starts to deviate from the multiphoton rate and follows the tunneling rate in the limit $\gamma \ll 1$. The transition takes place around $\gamma \sim 1$ and manifests itself in a soft kink. In this example plot, the work function ϕ is 4.5 eV and the photon energy 1.5 eV.

The other limiting case $\gamma \ll 1$ yields

$$\operatorname{arcsinh} \gamma \approx \gamma - \frac{\gamma^3}{6} \Rightarrow P(\gamma) \propto \exp\left(-\frac{2\phi}{\hbar\omega} \cdot \frac{2\gamma}{3}\right) \propto \exp\left(-\frac{4\sqrt{2m}\phi^{3/2}}{3|e|\hbar E_0}\right) \quad (2.8)$$

and can be identified with the tunneling regime. The deduced rate is identical to tunneling rates obtained for electron emission in static electric fields (field emission in the solid-state case [52] and static ionization in the atomic case [53, 54]). Therefore the tunneling regime is also called quasi-static regime. In the Keldysh-type treatment described here, photoemission from a metal surface is analogous to atomic ionization. It is important, however, to point out that the symmetry characterizing the atomic case is broken at a metal surface: Electron emission is only possible from the metal half-space to the vacuum half-space. In contrast, electrons in atomic ionization can be emitted into the two opposite half-spaces around the atom.

We will now turn our attention to the intermediate regime where neither the photon picture nor the tunneling picture is strictly valid. Here the generalized Keldysh rate strongly deviates from the rates derived for the two limits (see Fig. 2.2).

2.1.3 Above-Threshold Photoemission and strong-field effects

The lowest multiphoton order dominates the photoemission rate in the multiphoton regime. Moving towards higher intensity and lower γ we also find substantial contributions from higher multiphoton orders $n > n_{\min}$. Hence more photons than required are absorbed (see Fig. 2.3(a) for an illustration). This emission mechanism is called

above-threshold photoemission (ATP) for solids and above-threshold ionization (ATI) for atoms. It has first been observed in the atomic case in 1979 by Agostini *et al.* [55] and in the metallic case by Luan *et al.* [56] in 1989. Considering a cw light field irradiating a metal surface at grazing incidence, we find that the kinetic energy spectrum is given by sharp peaks with energies

$$E_{\text{kin}}^{(n)} = n\hbar\omega - \phi, \quad (2.9)$$

where $n \geq n_{\text{min}}$. This considers only a single initial state at the Fermi level E_F . The peaks are usually smeared out because many initial states below E_F are involved in the emission. Fig. 2.3(b) displays a typical photoelectron spectrum, taken from the first-ever experimental measurement of ATP [56]. The authors irradiated a polycrystalline copper surface with a pulsed laser at 1064 nm wavelength at an intensity of $5 \times 10^8 \text{ W cm}^{-2}$. Peaks spaced with the photon energy ($\sim 1.2 \text{ eV}$) are appearing, just as expected. The overall count rate decreases exponentially with increasing energy. In general, a measurement of the total photoemission rate and its nonlinear dependence on intensity does not unambiguously prove above-threshold effects. The lowest order still dominates the rate up to a certain point and the rate is given by the LOPT power law (Eq. 2.2). Experimental observations of ATP or ATI require spectrally resolved measurements so that high-energy peaks corresponding to the absorption of $n > n_{\text{min}}$ photons can be detected.

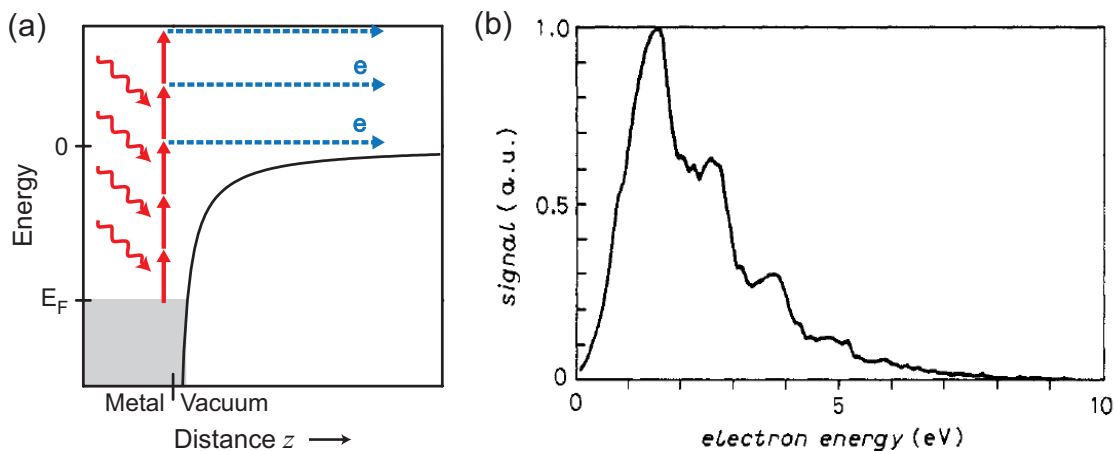


Figure 2.3: Above-threshold photoemission. (a) Illustration of the emission process. More photons (red) than the minimum required number are absorbed and the electron is emitted over the barrier. (b) First observation of above-threshold photoemission from a metal surface [56]. A copper surface was illuminated with pulsed laser light at a wavelength of 1064 nm with an intensity of $5 \times 10^8 \text{ W cm}^{-2}$. Peaks corresponding to the absorption of n photons of energy 1.2 eV are appearing in the spectrum (black curve). Taken and modified from [56].

Moving towards $\gamma \sim 1$, the contributions of individual photon orders and the peak positions start to deviate from the LOPT power law. Two effects were found in ATI experiments with atomic gases using sub-ps laser pulses: First, the position of the peaks shift to lower energies with increasing intensity [57]. The shift in energy was determined to be the ponderomotive energy U_p that scales linearly with intensity. Second, the lowest-order multiphoton peak disappeared when increasing the intensity beyond a certain

threshold (“channel closing”). At even higher intensities, one by one also the next orders disappeared.

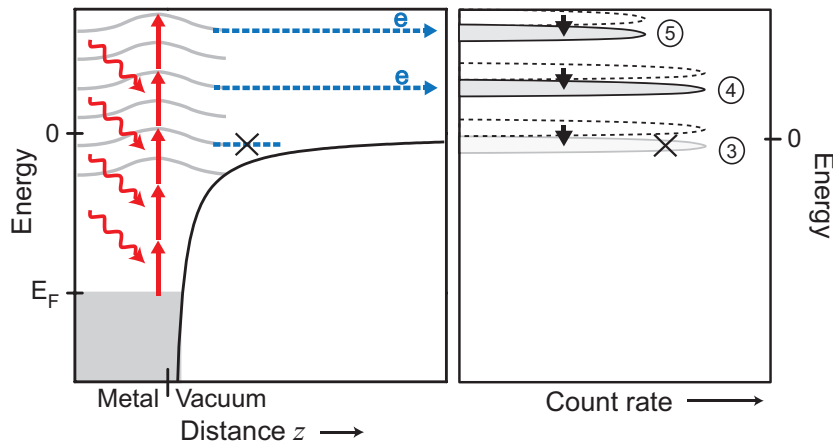


Figure 2.4: Channel closing and peak shifting in surface photoemission. Illustration in a potential energy diagram. The system is irradiated with an intense sub-ps pulse that causes an instantaneous light shift of the continuum states and of the states at the photoemission threshold to higher energy (indicated by the grey curves). The light shift accounts for the fact that electrons in these states strongly quiver in the field and possess extra energy, the ponderomotive energy U_p . Multiphoton transitions (red) take place during the presence of the pulse, with the electrons ending up in the light-shifted states. The electrons (blue) lose the extra energy after the pulse has ended and the quiver motion has stopped. The influence on photoelectron spectra is displayed is sketched on the right: The photoelectron peaks shift to lower energy (peak shifting) and the lowest multiphoton order disappears (channel closing).

The mechanism for peak shifting and channel closing is the following: When the intensity is increased, the ponderomotive energy U_p of the photoelectron is not negligibly small anymore. For example, an intensity of $1 \times 10^{13} \text{ W cm}^{-2}$ corresponds to a ponderomotive energy of 0.60 eV for light with a wavelength of 800 nm. Fig. 2.4 illustrates what happens in the case of a metal surface: In a multiphoton transition, the ponderomotive energy has to be supplied in addition to the energy difference of initial and final states. In pulsed excitation, this extra energy is lost after the pulse has ended since the electron stops to quiver. This leads to an energy shift ΔE for all spectral features², with $\Delta E = -U_p$. The shift scales linearly with intensity. Since we consider a pulsed excitation and U_p changes within the pulse envelope, one has also to account for the time-dependence of U_p . Effectively, the peak shifting effect gives rise to a modified electron spectrum described by

$$E_{\text{kin}}^{(n)} = n\hbar\omega - \phi - U_p \geq 0. \quad (2.10)$$

Moreover, the shift can cause lower-lying multiphoton orders to disappear since the total kinetic energy must possess a positive sign. Electrons from these orders are not able to

²Shifting peak positions were not observed for laser pulses with durations above 1 ps. Then the electrons are enabled to “surf down” the ponderomotive potential and leave the focal spot before the end of the pulse. The loss of energy U_p is exactly compensated by this effect. For a discussion of this long-pulse regime (as opposed to the short-pulse regime considered here) see [58, 59].

overcome the barrier anymore because the states around the photoemission threshold are also upshifted in energy by U_p . The corresponding quantum mechanical picture is the AC Stark shift (or light shift): During the presence of the laser pulse, the continuum states are field-dressed and upshifted in energy. Here the light shift of the initial state must be assumed to be negligible, which is a good approximation for an atomic system and can also hold true for electronic bands in metals (see the discussion in Section 4.2).

These effects are called strong-field effects and are an unambiguous sign that the strong-field regime is reached and the rather naive perturbative approach of Eqs. 2.2 and 2.9 breaks down. The so-called nonadiabatic tunneling regime [60], i.e., the transition regime between multiphoton and tunneling regime, is marked by a characteristic change in nonlinearity: A soft “kink” is appearing around $\gamma \sim 1$ in the Keldysh rate (see Fig. 2.2). The tunneling-like behavior towards high intensities is in essence the consequence of a rapid series of more and more channel closings [61, 62]. Strong-field effects are well established in atomic physics, with many experiments confirming their existence (see, e.g. [57, 63]). In Chapter 4 we will present the first experimental observation of peak shifting and channel closing in photoemission from a metal nanotip.

2.1.4 Other photoemission mechanisms

The last section was concerned with effects that occur both with atoms in the gas-phase and with metal surfaces. Here we will present two emission mechanisms that are specific to metal surfaces and in particular to nanotips: Photofield emission and thermally enhanced field emission. Both effects are enabled by the possibility of applying strong static electric fields to the system. Metal nanotips can be biased with a high voltage with respect to an anode. Due to the boundary conditions imposed by the sharpness of the tip, local field strengths on the order of GV m^{-1} can be attained easily on the surface of the tip’s apex. In general, the static electric field that one can apply to a metal nanotip can strongly influence all emission mechanisms outlined above.

Photofield emission

Photofield emission [64] from metal nanotips is a two-step process: Electrons are excited by one-photon absorption to intermediate states and are then emitted from a metal tip by field emission (see Fig. 2.5(a)). Field emission [52] can occur at static electric field strengths of $\sim \text{GV m}^{-1}$ or more. Electrons are enabled to tunnel from the metal into the vacuum through a penetrable tunneling barrier, very similar to light-induced tunneling. We will take a closer look at field emission in Subsection 3.3.2. Here field emission takes place after electrons are excited by one-photon absorption.

The photoemission rate of photofield emission depends both on laser intensity and the static field strength at the surface. Since we consider a one-photon excitation process the rate scales linearly with intensity. Furthermore, the rate depends strongly on the static field strength according to the Fowler-Nordheim tunneling equation (see Eq. 3.2). The work function ϕ in the equation has to be replaced by an effective barrier height $\phi - \hbar\omega$, the work function reduced by the photon energy [64, 27]. The resulting photoelectron spectrum is basically a convolution of the laser spectrum with the surface density of states along the laser polarization axis and with the tunneling probability from the field

emission step [65]. This emission process is also particularly sensitive to decoherence effects. Electron-electron and electron-phonon scattering inherent to metals strongly modify the spectral structure on time scales larger than 10 fs [65, 66].

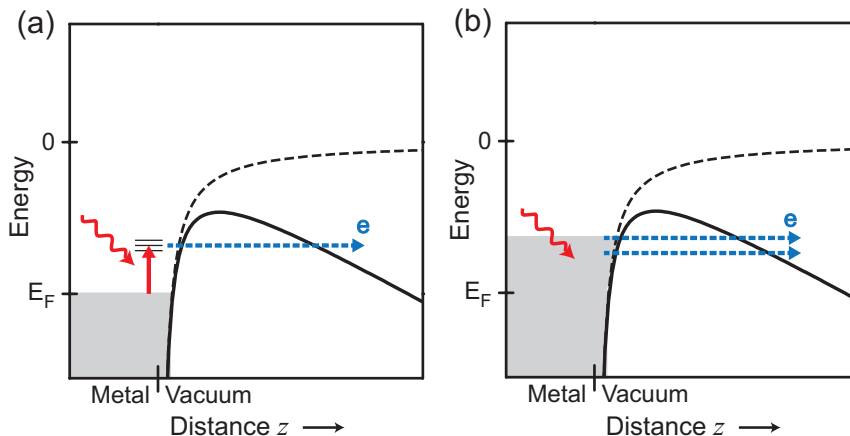


Figure 2.5: Photoemission mechanisms specific to metal surfaces. (a) Photofield emission. The metal absorbs one photon, promoting an electron to an excited state. In a second step, the excited electron is field-emitted into the vacuum. (b) Thermally enhanced field emission. Heating induced by high-intensity light leads to a transient population in higher electronic states. Excited electrons eventually tunnel from the metal by field emission.

Thermally enhanced field emission

Thermally enhanced field emission is similar in nature to photofield emission since it is also a two-step process [64, 67] (see Fig. 2.5b for an illustration). Laser light can strongly excite electrons within the metal tip, creating a non-equilibrium electron distribution and heating the electron gas to temperatures on the order of 1,000 K and more. This temperature is established by electron-electron scattering and associated relaxation processes and does not refer to the temperature of the metal itself that is given by the lattice temperature. Only after thermalization of electron gas and lattice via electron-phonon and phonon-phonon scattering a steady-state lattice temperature is reached. During and after excitation of the electron gas electrons transiently occupy states with much higher energies than the Fermi level. These electrons can be field-emitted from the metal if a strong static electric field is applied to the tip. Very strong excitation with electron gas temperatures on the order of $\sim 50,000$ K (corresponding to ~ 5 eV) can also enable emission over the barrier without the necessity of strong static fields and field emission. The heating effect strongly depends on many parameters like laser intensity, pulse duration and material properties (see Ref. [67] for a detailed discussion) and can compete with all the emission mechanisms outlined above. Thermally enhanced field emission has found to be highly nonlinear in the laser intensity [67]. Since the electron gas excitation persists for up to 1 ps electron emission is not prompt, in contrast to the emission processes described above.

We find, however, that this emission process does not play a role for tungsten and gold tips within the investigated parameter region of our experiment. We estimate the thermalized electron gas temperature for our parameters (6 fs pulses at 800 nm wavelength,

intensity $\sim 10^{12} \text{ W cm}^{-2}$) to around 2,000 K. This is much too small for pure thermal emission over a barrier height of about 5.2 eV (corresponding to $\sim 60,000 \text{ K}$). Moreover, mostly static field strengths below 1 GV m^{-1} were used in the experiment, insufficient for field emission to occur from excited states. Hence we can exclude a significant contribution of thermally enhanced field emission.

2.2 Electron recollision and the Three-Step Model

Attosecond physics is beautifully demonstrated in the recollision mechanism [4, 2, 3]. The local laser electric field steers the motion of a photoemitted electron and can cause the electron to return to the parent matter. The photoelectron then eventually scatters with the parent matter – recollision takes place. The occurrence of recollision is very sensitive to the temporal shape of the laser pulse. The time frame when the recollision takes place is strongly confined. For a light field with a wavelength of 800 nm recollision is limited to a few hundred attoseconds.

Upon recollision, several processes have been observed: High-harmonic generation (HHG, [6, 7]), rescattering³ [16] or nonsequential double ionization (NSDI, [68]). In HHG, the photoelectrons recombine, leading to the emission of high-energy photons. Rescattering refers to fully elastic scattering of the photoelectron with the parent matter and manifests itself in high-energy electrons. In NSDI, a photoelectron scatters with another electron from the parent matter, effectively leading to the emission of the latter electron in addition to the recolliding electron⁴.

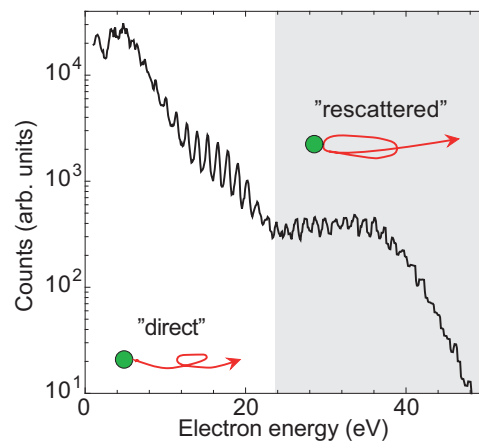


Figure 2.6: Typical photoelectron spectrum of rescattered electrons. The photoelectron spectrum was recorded with xenon gas at a wavelength of 800 nm and a laser intensity of $\sim 7 \times 10^{13} \text{ W cm}^{-2}$. Direct electrons form the low-energy part of the spectrum. Starting at an energy of about 25 eV, rescattered electrons fully dominate the spectrum. A plateau-like structure appears where the count rate does not change much with increasing energy. The plateau is terminated by a high-energy cut-off at about 40 eV. Taken from [69].

³Rescattering is also called high-order above-threshold photoemission (HATP) or ionization (HATI).

⁴Forward scattering, the least dramatic type of interaction with the parent matter, is also possible and very probable for atoms, molecules and solid surfaces.

In this section we focus on rescattering. Rescattering has first been observed by Paulus and co-workers in 1994 [16, 17]. Fig. 2.6 displays a typical experimental spectrum obtained with xenon gas at an intensity of $\sim 7 \times 10^{13} \text{ W cm}^{-2}$ [69]. Direct electrons dominate the low-energy part of the spectrum which shows a strong exponential decay of the count rate. On top of the decay we find peaks from above-threshold ionization. An abrupt change is visible at 25 eV energy: the count rate does not change much anymore with increasing energy. This region is called plateau. At an energy of about 40 eV, the count rate again drops dramatically. The energy position where this strong decay starts is called cut-off. Plateau and cut-off are formed by rescattered electrons. We will show in Chapter 5 that the same phenomenon can also be observed at metal surfaces. Here we focus on the theoretical description of recollision and rescattering that is common to both systems, atomic gas and metal surfaces.

An intuitive semiclassical model that even delivers quantitative predictions about recollision and the subsequent processes is the Three-Step Model (TSM), also called Simple Man’s Model (SMM). It has been formulated by Paul Corkum in his seminal paper in 1993 [4], with precursory work by many others [70, 71, 72, 73]. The recollision mechanism is split into three steps of different nature, illustrated in Fig. 2.7 for a metal surface. Here we concentrate on the rescattering process and its TSM description for a cw laser field in one dimension.

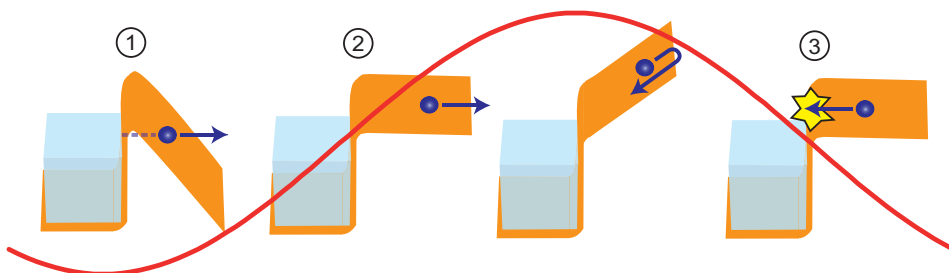


Figure 2.7: The Three-Step Model of the recollision mechanism at a metal surface. Step ①, emission: The electron is liberated from the metal by tunneling photoemission. Step ②, propagation: The electron, treated now as a classical point-like charged particle, is propagating on classical trajectories in the laser electric field (red curve). Electrons emitted within a certain time frame are pulled back to the metal surface when the laser field changes sign. Step ③, recollision: The electron eventually returns to the surface and recollides with it. Upon recollision, most prominently rescattering (fully elastic scattering) or high-harmonic generation (recombination) can take place.

The TSM for rescattering includes the following steps:

In the first step, photoemission takes place and a photoelectron is “born” into the vacuum with a certain probability. This step is described by quantum mechanics, usually invoking light-induced tunneling as the photoemission mechanism. For a practical calculation one determines the probability $W(t)$ for photoemission over time using a tunneling rate such as the Ammosov-Delone-Krainov (ADK) rate [74] or another rate related to Keldysh’s tunneling formula (Eq. 2.8). Tunneling is naturally confined to a short time window around the extrema of the electric field. In contrast to the atomic case, emission from a surface takes place only when the field has a negative sign, i.e.,

when the field vector points into the metal surface. This is due to symmetry breaking at the metal-vacuum interface.

In the second step, the liberated electron is exposed to the laser electric field and begins to perform a field-driven quiver motion. The electron is described in a purely classical way as a point-like charged particle and is propagated on classical trajectories following Newton's equation of motion. We assume that the photoelectron starts on its trajectory at time t_0 at the origin (given by the site of the nucleus for an atomic system or by the surface boundary for a metal surface) with zero initial velocity. Depending on the value of the field's vector potential $A(t_0)$ at its birth time t_0 , a photoelectron acquires a drift momentum $k(t_0) = qA(t_0)$ where $q = -|e|$ is the electron charge. The vector potential is given by $A(t) = -\int_{-\infty}^t E_L(\tau)d\tau$, where $E_L(t)$ denotes the optical electric field. The instantaneous momentum of photoelectron also includes the quiver motion and is given by $k_{\text{inst}}(t) = k(t_0) - qA(t)$. In a cw laser field drift energies of up to $2U_p$ can be reached [75]. The probability that a trajectory associated with a particular emission time t_0 gets populated is given by the instantaneous photoemission rate $W(t_0)$.

In the third step, recollision takes place and results in rescattering. As mentioned above, the occurrence of recollision strongly depends on the birth time t_0 and on the temporal shape of the light field given by the vector potential $A(t)$. Most electrons do not return to the origin and only the drift energy acquired at their very birth gets detected. These electrons are called direct electrons. Here we consider a photoelectron returning to the origin and recolliding with the parent matter at time t_1 . The time instant t_1 as a function of birth time t_0 can be deduced numerically or by a graphical solution [75]. The instantaneous momentum of the recolliding electron is then given by $k_{\text{rec}}(t_0, t_1) = qA(t_0) - qA(t_1)$ and its kinetic energy by $E_{\text{kin,rec}}(t_0, t_1) = q^2[A(t_0) - A(t_1)]^2/(2m)$. When the incoming photoelectron fully elastically scatters with the parent matter, its instantaneous momentum is fully reversed. Here the scattering object can be regarded as an infinitely high potential barrier, essentially a hard wall. After recollision and the sign flip of the momentum the electron can once again take up more kinetic energy from the laser field. It ends up with a final kinetic energy of $E_{\text{kin,final}}(t_0, t_1) = q^2[2A(t_1) - A(t_0)]^2/(2m)$ at a distant detector [75].

It is instructive to take a look at the final kinetic energy of a rescattered photoelectron as a function of its birth time within a laser cycle. Numerically evaluating the classical electron trajectories (second TSM step) and the return condition (third TSM step), $E_{\text{kin,final}}(t_0, t_1)$ can be calculated for each trajectory starting at some time instant t_0 . Fig. 2.8(a) displays the results of such a calculation for a cw light field with a wavelength of 800 nm. The evaluation shows that recolliding electrons can only be born within a narrow time window (~ 400 as) after the laser electric field has reached its peak value. Recollision takes place after approximately $2/3$ of the optical cycle duration and is also strongly confined to a sub-cycle time window. The maximum instantaneous kinetic energy of an incoming electron at recollision is $3.17U_p$ [4]. Through rescattering the electrons can gain a maximum final kinetic energy [17] of

$$E_{\text{cut-off}} = 10.007U_p. \quad (2.11)$$

The maximum energy has been named cut-off energy and Eq. 2.11 is commonly referred to as the $10U_p$ cut-off law. It can be identified with the position of the cut-off in experimental data (see Fig. 2.6). For 800 nm the times corresponding to the cut-off energy

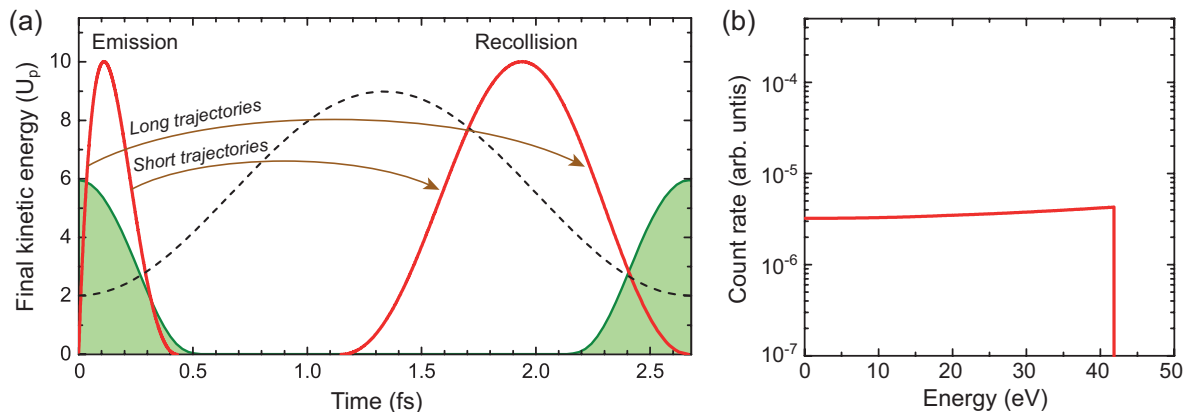


Figure 2.8: Quantitative description of rescattering with the Three-Step Model.

(a) Final kinetic energy of rescattered electrons (red curve) as function of their emission time (left part) and recollision time (right part). The calculation was carried out for a wavelength of 800 nm and a work function of 4.5 eV. The emission times for rescattered electrons is limited to a short time window after the optical field strength (dashed black curve) reaches a peak value, here with negative sign. Further temporal confinement is caused by the emission probability (green curve) that is strongly localized to the peak of the electric field. Note that electrons are only emitted when the field has a negative sign due to the symmetry breaking occurring at the metal surface. (b) Resulting energy spectrum for a continuous-wave light field resembling the experimental parameters of the plot in Fig. 2.6. Only rescattered electrons are included in the calculation. A plateau-like structure is found that is abruptly terminated at a cut-off energy of about 42 eV.

are $t_0 = 0.11$ fs (emission) and $t_1 = 1.94$ fs (recollision). In the TSM framework, every emission time is always associated with the same final kinetic energy if the latter is expressed in multiples of U_p .

There are two classes of trajectories in the TSM, namely long and short trajectories. Electrons on long trajectories are born before the peak in the final kinetic energy at $t_0 = 0.11$ fs and spend a much longer time in the laser field than those on short trajectories born after the peak. Both trajectory classes meet at the maximum kinetic energy at a recollision time of ~ 1.9 fs.

Recollision trajectories are populated by photoelectrons originating from light-induced tunneling. Fig. 2.8 displays the instantaneous Keldysh rate in the tunneling limit (Eq. 2.8). Here tunneling is confined to a short time window of sub-cycle duration (~ 500 as) centered around the maximum field. This strongly influences the shape of the resulting photoelectron spectrum: Preferably long trajectories are populated by electrons from tunneling, mitigating the contribution of electrons on short trajectories. Fig. 2.8(b) shows the TSM results for the experimental data presented in Fig. 2.6. Only rescattered electrons are considered. Indeed a plateau structure emerges, with an abrupt termination by a high-energy cut-off at ~ 42 eV. The coincidence with the experimental data in Fig. 2.6 shows that even quantitative information can be gained from the TSM.

The model offers valuable insight into the recollision mechanism in terms of classical trajectories and well-defined timing. It is able to demonstrate that the recollision mechanism is a field-driven process taking place on attosecond time scale. Moreover, a

plateau structure and an high-energy cut-off naturally emerge from the TSM. But the model also shows severe weaknesses. For example, in the first step tunneling photoemission is assumed to take place and hence a tunneling barrier of finite width has to be penetrated. According to the TSM, electrons start from the origin (atomic core or surface barrier) with zero initial velocity. The traversal of the classically forbidden barrier region is completely ignored. Moreover, the TSM does not account for quantum effects in the second and third steps; coherence effects are not included. We will see later that quantum interference of electron wavepackets play a crucial role in the understanding of both theory and experiment. These and other shortcomings will be addressed with refined models in the next section.

2.3 Quantum Orbit Theory of recollision

The Quantum Orbit Theory [75, 76] is a semiclassical approach to strong-field photoemission and recollision processes. It can be directly derived from the Keldysh theory and the underlying strong-field approximation. It provides an understanding of recollision in terms of classical electron trajectories or “quantum orbits”, without losing fundamental quantum mechanical characteristics. We will now discuss an important prerequisite to the Quantum Orbit Theory, the strong-field approximation.

2.3.1 The strong-field approximation

Photoemission from a single atom and from a metal surface can be described within the theory framework pioneered by Keldysh as already outlined in Sections 2.1. The quantum mechanical potentials for both systems are closely related as we will see in the following. This paves the way for a treatment within the same theory framework.

Fig. 2.9 illustrates the shape of the potential for three important systems: In the first case we take a look at a realistic hydrogen-like atomic system. For a sound description one can assume a coulombic potential containing a ground state with binding energy I_p (see (Fig. 2.9(a))). A cw light field, here described in the length-gauge dipole approximation⁵, perturbs the potential in the whole spatial range with the optical frequency. A major simplification can be made if one ignores the Coulomb force and instead considers the so-called zero-range (or short-range) potential [77]. The zero-range potential is formed by a delta function potential well and contains only a single bound state. The corresponding wave function lives only in the classically forbidden region and has therefore exclusively evanescent character (see Fig. 2.9(b)). Ignoring the Coulomb force and considering only a single bound state are rather strong approximations for an atom, but this approach is justified in a slightly different system: Singly-charged negative ions do not show Coulomb attraction since a neutral atom remains after the ejection of the excess electron. For these ions calculations with the zero-range potential and Keldysh theory show excellent agreement with experimental data [78, 79].

⁵For most cases the size of an atom is much smaller than the wavelength of the incoming light, so any spatial dependence of the optical field amplitude can safely be neglected. At nanotips, however, the enhanced optical near-field and its strong spatial dependence can lead to different scenarios (see Section 2.5 for details).

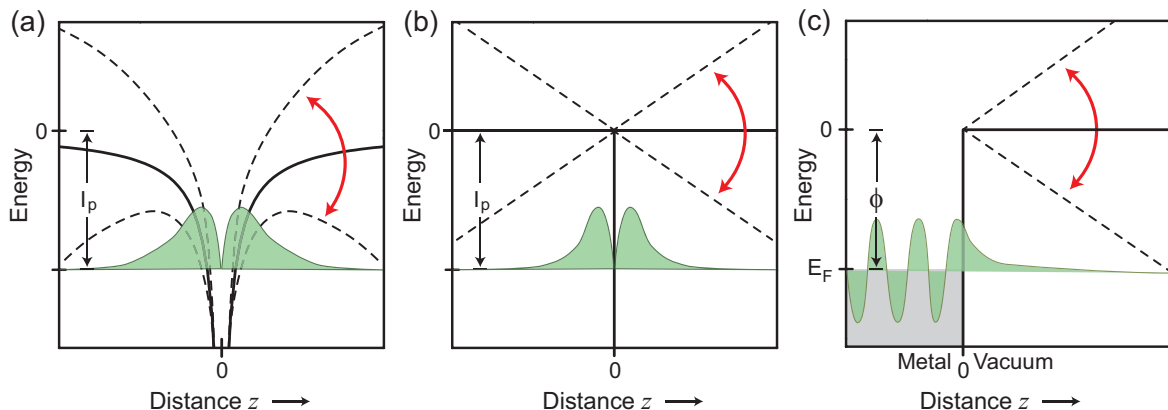


Figure 2.9: Model potentials for atomic and metallic cases. (a) Hydrogen-like atomic potential. The green curve illustrates the shape of the wave function of the ground state with binding energy I_p . The light field modulates the potential in the whole spatial range. (b) Zero-range potential. Like (a), but the coulombic potential has been replaced by a delta potential. The ground state wave function lives completely in the classically forbidden region. This model potential is particularly suitable for a description based on the strong-field approximation. (c) Metal surface. The illustrated wave function corresponds to an electronic state with binding energy (work function) ϕ at the Fermi energy E_F . Very much like the two other systems, the wave function also exhibits an evanescent part. The light field is strongly screened inside the metal, hence here only the vacuum part of the wave function is directly perturbed by the field.

The third system under scrutiny is a flat metal surface. The simplest description of a metal-vacuum interface at spatial coordinate $z = 0$ is given by a semi-infinite potential well, illustrated in Fig. 2.9(c). z denotes the spatial coordinate used throughout this thesis. We limit ourselves everywhere to one dimension which is a good approximation for surfaces. The potential well in the metal half-space has a depth corresponding to the so-called pseudopotential. The pseudopotential is generated by the atomic potentials at the lattice sites and the filled metallic bands. Electron-electron interaction, electron-phonon coupling and the image force exerted on an electron propagating in the vacuum half-space are neglected and we are considering only a single active electron at the Fermi energy E_F . The corresponding state exhibits an evanescent part in the vacuum half-space with a $(1/e)$ decay length of $\zeta = \sqrt{-\hbar^2/(2mE)}$ that is on typically on the order of Ångström. Calculations with time-dependent density functional theory (see Subsection 2.4.2) and a finite-difference time-domain solution of Maxwell's equations (see Section 2.5) show that the field inside the metal is strongly screened. The screening effect takes place on an Ångström length scale close to the metal-vacuum boundary. Therefore the action of the light field is limited to the vacuum half-space in this approximate description. The screening effect is the only multielectron effect that is accounted for in the model. The laser field enters in the length-scale dipole approximation with the time-dependent potential

$$H_1(t) = -qE(t)\Theta(z)z, \quad (2.12)$$

which can be identified with the Hamiltonian in the interaction picture. In this one-dimensional approach, the light field and electron propagation axis are assumed to be

parallel. The heaviside function $\Theta(z)$ accounts for the fact that the field causes a perturbation only in the vacuum half-space. The evanescent part of the metallic state is exposed to the rapidly oscillating laser field, just as in the case of the atom-like zero-range potential and in the case of the hydrogen-like atomic system. This fact makes these systems comparable on a very basic level [80]. In the following, we will first treat the atom-like zero-range potential.

Direct electrons in the strong-field approximation

The theory approach by Keldysh [45], also called Keldysh-Faisal-Reiss (KFR) theory because of later contributions by Faisal [81] and Reiss [82], could explain many phenomena in strong-field ionization of atomic gases. It is also known as the strong-field approximation (SFA)⁶. We discussed the most important results of the theory already in Subsection 2.1.2, here we focus on the basic assumptions for its derivation. We begin our discussion with direct electrons and first treat our problem with first-order time-dependent perturbation theory. The probability $P_p(t)$ to detect a momentum state $|\psi_p(t)\rangle$ with drift momentum p at a distant detector at time t (initial state $|\psi_i(t)\rangle$) is given by $P_p(t) = |a_p(t)|^2$, where

$$a_p(t) = -\frac{i}{\hbar} \int_{-\infty}^t d\tau \langle \psi_p(\tau) | H_I(\tau) | \psi_i(\tau) \rangle \quad (2.13)$$

is a complex probability amplitude. The initial state represents a bound electron with binding energy I_p . The role of intermediate states and resonances is completely neglected so that the first-order approach is fully justified. In first-order time-dependent perturbation theory, the time-dependence of the initial state and the final state in Eq. 2.13 only contains the time evolution according to the unperturbed (field-free) Hamiltonian. Keldysh in his ansatz [45], however, exchanged the final state $|\psi_p(t)\rangle$ with a Volkov state $|\psi_p^V(t)\rangle$ in order to account for the dynamics of the free electron in the laser field. The Volkov wave function [83] in one dimension is given by

$$\psi_p^V(z, t) = \exp \left\{ \frac{i}{\hbar} \left[[p - qA(t)] z - \int_{-\infty}^t \frac{[p - qA(\tau)]^2}{2m} d\tau \right] \right\}. \quad (2.14)$$

It represents a free electron with drift momentum p quivering in a laser field with vector potential $A(t)$. We can now separate space- and time-dependent part of the two wave functions and write the amplitude in a more convenient way. The SFA probability amplitude for direct electrons is then given by

$$a_p(t) = -\frac{i}{\hbar} \int_{-\infty}^t dt_0 \langle \psi_p^V | H_I(t_0) | \psi_i \rangle \times \exp \left\{ -\frac{i}{\hbar} \int_{t_0}^t \frac{[p - qA(\tau)]^2}{2m} d\tau \right\} \exp \left\{ -\frac{i}{\hbar} I_p t_0 \right\}. \quad (2.15)$$

Here we can use the abbreviation

$$S_p^{(\text{cl})}(t_0, t_1) = \int_{t_0}^{t_1} \frac{[p - qA(\tau)]^2}{2m} d\tau. \quad (2.16)$$

⁶The terms strong-field approximation, Keldysh theory and KFR theory all refer effectively to the same theory approach, but there are important differences in formalism and argumentation.

$S_p^{(\text{cl})}(t_0, t_1)$ can be identified with the classical action integral along an electron trajectory. An electron with drift momentum p propagates in a light field with vector potential $A(t)$ from time t_0 to time t_1 . This classical interpretation is very useful as we will see in the next subsection. The so-called quasiclassical action

$$S_p(t_0) = -S_p^{(\text{cl})}(t_0, +\infty) - \int_{-\infty}^{t_0} I_p d\tau = - \int_{t_0}^{+\infty} \frac{[p - qA(\tau)]^2}{2m} d\tau - \int_{-\infty}^{t_0} I_p d\tau \quad (2.17)$$

includes the time evolution of the initial state. For $t \rightarrow +\infty$, Eq. 2.15 can be transformed into the simple expression [84]

$$a_p = -\frac{iB}{\hbar} \int_{-\infty}^{+\infty} dt_0 \exp [iS_p(t_0)/\hbar]. \quad (2.18)$$

The prefactor B contains, among some constants, the dipole matrix element from the spatial integration in Eq. 2.15.

Compared to a full solution of the time-dependent Schrödinger equation, the SFA neglects the influence of the light field on the initial state. Within this approximation, the dynamic AC Stark shift and the displacement of the electron matter wave (polarization) of the initial state are ignored. In addition, the influence of the binding potential on the final states is neglected, whereas the action of the laser field is described in all orders and includes the AC Stark shift of continuum states. Moreover, depletion of initial states by photoemission is assumed to be negligible. The SFA can be applied in the low-frequency limit $\hbar\omega \ll I_p$ in the atomic case or $\hbar\omega \ll \phi$ in the metallic case. The SFA is the ansatz for the results presented earlier when we discussed the Keldysh theory (see Subsection 2.1.2).

Rescattered electrons

Rescattering can be described with a higher-order SFA approach [85, 75]. The SFA includes here a further interaction with the parent matter at time t_1 . t_1 can be interpreted as the recollision time, in addition to the emission time t_0 . Furthermore, an integration over the full range of possible intermediate drift momenta k between emission and recollision has to be carried out. Following [84], the probability amplitude for rescattered electrons is given by

$$a_p^{(\text{resc})}(t) = -\frac{1}{\hbar^2} \int_{-\infty}^t dt_1 \int_{-\infty}^{t_1} dt_0 \int_{-\infty}^{+\infty} dk \langle \psi_p^V(t_1) | H_I(t_1) | \psi_k^V(t_1) \rangle \times \quad (2.19) \\ \times \langle \psi_k^V(t_0) | H_I(t_0) | \psi_i(t_0) \rangle.$$

For $t \rightarrow +\infty$ the equation can be recast into the expression

$$a_p^{(\text{resc})} = -\frac{B_{\text{resc}}}{\hbar^2} \int_{-\infty}^{+\infty} dt_1 \int_{-\infty}^{t_1} dt_0 \int_{-\infty}^{+\infty} dk \exp [iS_p^{(\text{resc})}(t_0, t_1, k)/\hbar], \quad (2.20)$$

with the redefined quasiclassical action $S_p^{(\text{resc})}(t_0, t_1, k)$ for rescattering

$$S_p^{(\text{resc})}(t_0, t_1, k) = - \int_{t_1}^{+\infty} \frac{[p - qA(\tau)]^2}{2m} d\tau - \int_{t_0}^{t_1} \frac{[k - qA(\tau)]^2}{2m} d\tau - \int_{-\infty}^{t_0} I_p d\tau. \quad (2.21)$$

The prefactor B_{resc} is analogous to B in Eq. 2.18 for the direct electrons. A straightforward interpretation follows from the expression for the action: Reading Eq. 2.21 from right to left, we can first identify the time evolution of the initial state up to emission time t_0 . The second term describes the action along a closed electron trajectory in the laser field with intermediate drift momentum k from time t_0 to the recollision time t_1 . Finally, we find the action along the electron trajectory with drift momentum p in the laser field from time t_1 to infinity. This order is already reminiscent of the steps in the TSM described in Section 2.2. The integration in Eq. 2.20 is carried out over all possible times t_0 and $t_1 \geq t_0$ and all intermediate momenta k . With this, Eq. 2.21 has the character of a path integral [86].

The strong-field approximation gives access to analytical solutions of strong-field photoemission for both direct and rescattered electrons. It can be applied not only to the atomic case, but also to the conceptionally simple case of a metal surface. The occurrence of quantities known from classical mechanics, in particular of the action integral, already paves the way to a classical interpretation of the involved physics. In the next subsection we will take a look at solutions of these equations involving the saddle point approximation. We will see that indeed classical trajectories, so-called quantum orbits, emerge from the saddle point solutions. We will also derive the semiclassical Three-Step Model introduced in Section 2.2.

2.3.2 Saddle-point approximation and quantum orbits

The saddle-point approximation (SPA), or its variations known as method of steepest descent or stationary phase approximation⁷, is a standard method to solve integrals of the type

$$A(a, b) = \int_a^b g(x) \exp [i\eta U(x)] dx. \quad (2.22)$$

$U(x)$ is a rapidly oscillating function for large η , whereas $g(x)$ is a function that slowly changes with increasing x . If these requirements are met, only regions around stationary points where $\partial U(x)/\partial x = 0$ give a significant contribution to the integral. Other contributions cancel each other due to the rapid oscillations and sign changes. For an approximate solution one needs to find these stationary points (or saddle points) x_n and replace the integral with a sum over all contributions from N saddle points between a and b :

$$A(a, b) \approx \sum_{n=1}^N g(x_n) \sqrt{\frac{2\pi i}{\eta \partial^2 U(x)/\partial x^2|_{x_n}}} \exp [i\eta U(x_n)]. \quad (2.23)$$

The prefactor to the exponential term comes from the Gaussian integral that needs to be solved in the SPA. The saddle-point approximation can be applied to the SFA probability amplitudes for direct electrons (Eq. 2.18) and for rescattering (Eq. 2.20). The mathematical trick by applying the SPA does not only lead to simpler expressions of the probability amplitudes, but also unveils the intuitive picture of semiclassical electron trajectories, or “quantum orbits”. We will also see that the Three-Step Model follows from the SPA in a straightforward way.

⁷For a detailed discussion of the saddle-point approximation, its derivation and limits in the context of strong-field photoemission, Ref. [84] is strongly recommended.

Direct electrons

We will now apply the SPA to Eq. 2.18 for direct electrons. The SPA is valid in the low-frequency limit $\hbar\omega \ll I_p$. Enforcing the saddle point condition $\partial S(t_0)/\partial t_0 = 0$ for the integration variable t_0 yields

$$\frac{1}{2m} [p - qA(t_0)]^2 + I_p = 0, \quad (2.24)$$

where t_0 denotes a saddle point solution of the equation for a given drift momentum p . In another form the equation reads

$$\frac{1}{2m} [p - qA(t_0)]^2 = -I_p, \quad (2.25)$$

which is reminiscent of an energy conservation relation. Up to time t_0 , the electron is bound in the initial state (energy $-I_p$, with the vacuum level defined as zero kinetic energy). At time t_0 , a transition takes place to a continuum state representing a free electron propagating in the laser field given by the vector potential $A(t)$ with drift energy p . Eq. 2.25 cannot be fulfilled for real t_0 because the right hand side is negative ($I_p > 0$) and on the left hand side we find a squared expression. m , p , q , the amplitude of the vector potential $A(t)$ and the binding energy I_p must be real since they represent constants or observables. In full accordance with the mathematical basis of the SPA [84], the saddle point $t_s = t_0$ must then become complex in order for the left hand side to be negative.

The complex nature of the saddle point t_s can be interpreted within the framework of the imaginary time method introduced by Perelomov, Popov and Terent'ev [50, 87]: In a semiclassical picture, an electron traverses the classically forbidden tunneling barrier region. A solution of the Newtonian equation of motion enforces that the motion of the electron “under the barrier” takes place in imaginary time. Fig. 2.10 illustrates this perspective: The electron starts its motion at the origin ($z_0 = 0$) with zero initial velocity at complex time t_s . It then emerges at real time instant $\text{Re } t_s$ from under the barrier. From this moment on, the propagation takes place fully in real time, just as expected for a free electron. Newton’s equations of motion can then be applied to the “classical electron”.

The semiclassical trajectory perspective is called Quantum Orbit Theory. Electrons are moving on “orbits” that are derived from the fully quantum mechanical framework of the SFA. This notion is supported by an energy-position-space analysis of full quantum mechanical calculations [76]. For a given quantum orbit associated with a saddle point t_s one can also define a tunnel exit [88, 89]. It is the point where the electron leaves the classically forbidden region and emerges as a free electron. It is simply given by the time integration of the instantaneous velocity along the imaginary time $\text{Im } t_s$ “spent” under the barrier and taking the real part of the results:

$$z_{\text{exit}}(t_s) = \frac{1}{m} \text{Re} \left\{ \int_{t_s}^{\text{Re } t_s} [p - qA(\tau)] d\tau \right\}. \quad (2.26)$$

Also a non-zero initial velocity $v_{\text{exit}}(t_s)$ can be defined:

$$v_{\text{exit}}(t_s) = \frac{1}{m} [p - qA(\text{Re } t_s)]. \quad (2.27)$$

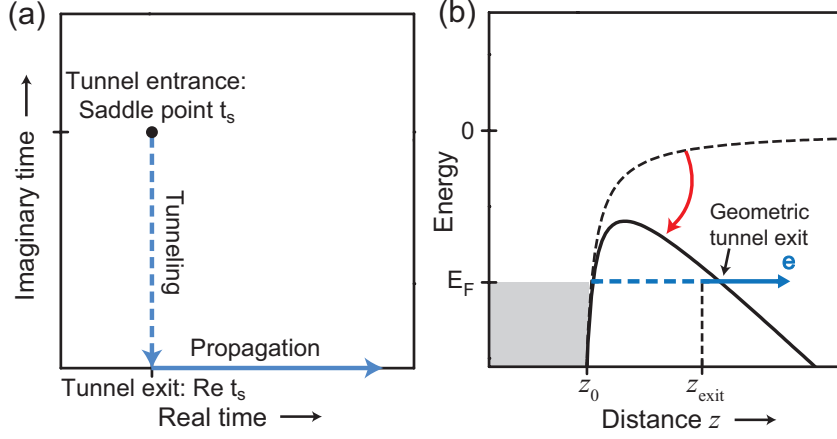


Figure 2.10: Imaginary time and quantum orbits. (a) Sketch of an electron trajectory (“quantum orbit”) in time according to the Quantum Orbit Theory and the related imaginary time method. The complex saddle point t_s can be identified with the time when the electron enters the tunnel and its real part with the time when it appears as a free electron at the tunnel exit. (b) Sketch of the motion of the electron in space. The motion along the imaginary time axis is interpreted as the motion of the electron under the barrier. The electron enters the barrier at the origin z_0 and leaves it at the tunnel exit z_{exit} . In general, the tunnel exit is not identical to the geometric definition of the exit point [88].

The tunnel exit position is not identical to a geometric definition of such a position [88, 89]. The geometric exit is defined as the position z where the instantaneous velocity is zero for a given quantum orbit. This fact will be discussed in detail in Subsection 2.3.4.

It is now straightforward to calculate photoelectron spectra with the SPA. The probability amplitude for direct electrons reads

$$a_p \approx -\frac{iB}{\hbar} \sum_{n=1}^N \sqrt{\frac{2\pi i\hbar}{\partial^2 S_p(t)/\partial t^2|_{t_n}}} \exp [iS_p(t_n)/\hbar], \quad (2.28)$$

where t_n denotes the solutions of the saddle point equation (Eq. 2.25) and N their number. The larger the imaginary part $\text{Im } t_n$ of a saddle point the smaller is its contribution to the probability $P_p = |a_p|^2$. In this way, the imaginary time is strongly connected with the tunneling amplitude. The concept of imaginary time is troublesome if one considers it to represent an actual time. It should be emphasized that it originates from a mathematical trick and that the considerations above simply represent an appealing interpretation. The time integration in the original SFA expression takes place only along the real time axis and does not contain any imaginary time.

Rescattered electrons

The SPA can also be applied to the probability amplitude for rescattered electrons (Eq. 2.20). Now three saddle point equations result because there are three integration

variables, t_0 , t_1 and k :

$$\frac{\partial S_p^{(\text{resc})}(t_0, t_1, k)}{\partial t_0} \rightarrow \frac{1}{2m} [k - qA(t_0)]^2 = -I_p. \quad (2.29)$$

$$\frac{\partial S_p^{(\text{resc})}(t_0, t_1, k)}{\partial k} \rightarrow \frac{1}{m} \int_{t_0}^{t_1} [k - qA(\tau)] d\tau = 0. \quad (2.30)$$

$$\frac{\partial S_p^{(\text{resc})}(t_0, t_1, k)}{\partial t_1} \rightarrow \frac{1}{2m} [p - qA(t_1)]^2 = \frac{1}{2m} [k - qA(t_1)]^2. \quad (2.31)$$

Just like for the direct electrons (Eq. 2.25), the first saddle point equation has the character of an energy conservation relation. At time t_0 , electrons tunnel through the barrier and emerge as free electrons in the laser field with intermediate momentum k . This can be interpreted as the emission step of the TSM. The second saddle point equation (Eq. 2.30) forces the electron to return to the origin. The distance covered by the electron on its quantum orbit between time t_0 and t_1 has to be zero. This corresponds to the propagation step of the TSM. The third equation (Eq. 2.31) also considers energy conservation, here at the recollision time t_1 . The instantaneous kinetic energy of the incoming electron with drift momentum k must be equal to the instantaneous kinetic energy (drift momentum p at a distant detector) after recollision. The three steps of the TSM directly follow from SFA via the SPA.

The emission time t_0 is a complex number just as for the direct electrons. But also the other saddle point components are affected: The recollision time t_1 is also forced to acquire a imaginary part [89, 90] as well as the intermediate momentum k . The physical interpretation of these complex quantities in the SPA is not straightforward [89] and will not be discussed here. Taking the limit $I_p \rightarrow 0$ of the saddle-point equations for rescattered electrons directly yields the TSM. Ignoring I_p , the first saddle-point equation (emission) can be fulfilled with real times t_n . In consequence, also the intermediate momentum k and the recollision time t_1 take on real values. The sub-barrier motion is neglected in this limit. The only survivor of quantum mechanics in the TSM is the tunneling rate used in the first TSM step.

Following [84], the complex probability amplitude for rescattered electrons according to the SPA is given by

$$a_p^{(\text{resc})} \approx -\frac{B_{\text{resc}}}{\hbar^2} \sum_{n=1}^N \frac{(2\pi i \hbar)^{5/2}}{\sqrt{\det \mathfrak{S}|_{\{t_{0,n}, t_{1,n}, k_n\}}}} \exp [iS_p(t_{0,n}, t_{1,n}, k_n)/\hbar], \quad (2.32)$$

where \mathfrak{S} denotes the Hessian matrix of the action $S_p(t_0, t_1, k)$ and $t_{0,n}$, $t_{1,n}$ and k_n denote the components of a saddle point.

In summary, complex times naturally emerge from the SPA. These times can be identified with the time instants of emission and recollision (real parts) and contain information about the corresponding probability amplitudes (imaginary parts). Electrons can be regarded as classical particles traveling on quantum orbits following Newtonian mechanics. Determining the complex times allows for a simple calculation of the probability amplitudes for direct and rescattered electrons. The TSM follows from ignoring the influence of the binding potential.

2.3.3 Spectral formation and quantum interference

In the following part, we will apply the Quantum Orbit Theory to a realistic example and calculate saddle points and the corresponding spectra. We will leave the atomic case and modify the Quantum Orbit Theory so that it can be applied to the case of a metal surface. A reduction of the number of quantum orbits accounts for the broken symmetry at the surface.

Saddle points for direct and rescattered electrons

The saddle point equations for direct electrons (Eq. 2.28) and rescattered electrons (Eq. 2.32) can be solved for a single optical cycle of a cw field with the help of a numerical method [89]. Fig. 2.11 displays the saddle point solutions for a light field with a wavelength λ of 800 nm and a field amplitude E_0 of 18 GV m⁻¹. The field is defined as

$$E_L(t) = -E_0 \cos(\omega t), \quad (2.33)$$

with the frequency $\omega = 2\pi c/\lambda$. The complex emission times $t_0^{(d)}$ for direct electrons are plotted in Fig. 2.11(a). Only the solutions around $t = 0$ are shown when the tunneling barrier is formed in the vacuum half-space at positive z . Solutions with negative imaginary part must be dropped because they lead to unphysical results and, more importantly, are non-existent in a rigorous mathematical application of the SPA [84]. The branch of solutions at negative times can be identified with direct electrons emitted in forward direction with positive drift momenta p . The branch at positive times also represents emission in forward direction, but these electrons change their propagation direction in the light field. They acquire negative drift momenta and end up in the half-space at negative z . From the calculation it is also apparent that electrons with zero drift energy are generated right at the maximum of the field. With increasing drift energy, the imaginary part of the emission time increases strongly. This leads to a strong decrease of the corresponding probability to detect a direct electron at higher energies.

The solutions for t_0 (emission time) and t_1 (recollision time) for rescattered electrons are shown in Fig. 2.11(b) and (c)⁸. There are two different branches that can be identified with long and short trajectories. In the vicinity of the classical cut-off energy at $10 U_p$ the two solutions avoid each other and start to diverge. Also the intermediate drift momentum k (not shown) acquires an imaginary part. In general, the imaginary parts increase for larger Keldysh parameters γ .

Fig. 2.12 displays the real part of the saddle times for rescattered electrons and the left branch of direct electrons vs. final kinetic energy. The results of the Quantum Orbit Theory calculation bear much similarity to the results of the TSM presented in the same figure. There are, however, important differences: The final kinetic energy is not restricted anymore to energies below the classical cut-off. The exponential decay of the count rate beyond the cut-off is accounted for in the Quantum Orbit Theory. Moreover, there are subtle differences in the timing of emission and recollision. The real parts of the emission and recollision times in gas-phase photoemission have been determined

⁸There also exist solutions that correspond to electrons spending two or more cycles in the field before recollision. Their contribution to the total yield for energies larger than $7 U_p$ is about one order of magnitude lower [84] and is neglected here.

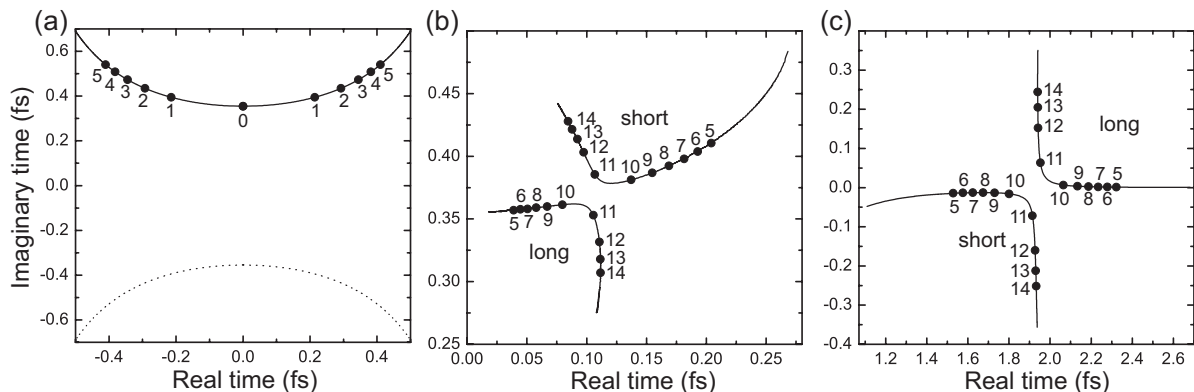


Figure 2.11: Saddle point solutions in complex time. (a) Saddle point solutions for direct electrons in complex time, around the maximum the electric field strength at time zero. The left branch at negative real time corresponds to emission of electrons in forward direction. Electrons from the right branch are emitted in forward direction, but turn in the field because they have a negative drift momentum. The numbers to each dot indicate the final kinetic energies in multiples of U_p . Solutions at negative imaginary times have to be dropped because they lead to unphysical results (dotted curve). The larger the imaginary part the smaller the contribution of the corresponding quantum orbit to the total emission probability. (b) Emission times t_0 of rescattered electrons. There are two branches corresponding to long and short trajectories. The branches avoid each other close to the classical cut-off at $10U_p$. (c) Recollision times t_1 of rescattered electrons. A behavior similar to (b) results. The calculation was carried out for single cycle of 800 nm light at an intensity of $4.3 \times 10^{13} \text{ W cm}^{-2}$ and a binding energy of 4.5 eV ($\gamma = 0.94$).

experimentally [18, 91]. Good agreement was found with the Quantum Orbit Theory, whereas the TSM strongly deviated from the measured values.

Quantum orbits for photoemission from a metal surface

At a metal surface, the symmetry that characterizes the atomic case is broken. Photoemission only takes place from the metal half-space into the vacuum half-space where a detector measures the drift energy of the photoelectrons. We can now modify the Quantum Orbits Theory in order to account for symmetry breaking at the metal-vacuum interface⁹.

Electrons are only emitted when the field has a negative sign and points into the metal, creating a tunneling barrier (see Fig. 2.8). Therefore all solutions to the saddle point equation for direct electrons (Eq. 2.25) where the field is positive and the barrier is absent are dropped. In addition, another class of quantum orbits and their corresponding saddle points do not contribute to the final energy spectrum, namely photoelectrons that possess negative drift momenta. They are emitted in forward direction, but due

⁹Bunkin and Fedorov [46] in their application of the Keldysh theory to surfaces totally ignore symmetry breaking at the surface, in full accordance with the SFA. The only SFA approach that includes symmetry breaking is the model presented by Yalunin and co-workers [62]. It shows excellent agreement with a fully quantum mechanical *ab-initio* calculation when it comes to the total emission probability. However, the calculation of a realistic rescattering spectrum is elusive because the re-distribution of energy at recollision with the metal surface is ignored in this model.

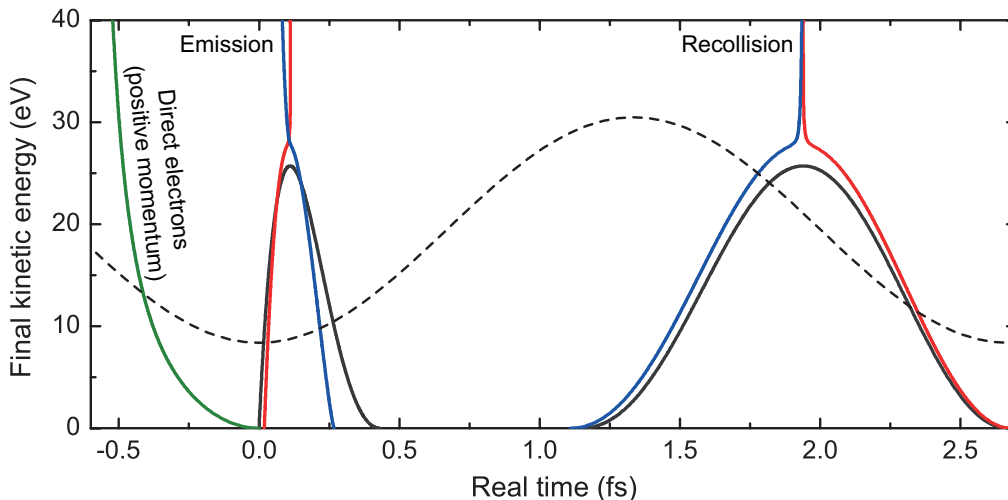


Figure 2.12: Timing of direct emission and rescattering in the Quantum Orbit Theory. Final kinetic energy as a function of the real parts of the saddle times from Fig. 2.11. We show the final energy of direct electrons emitted in forward direction is shown (green curve) as well as that of rescattered electrons on long trajectories (red curve) and short trajectories (blue curve). The black curve displays the result of the TSM for the same parameter set and the dashed curve sketches the driving field. Kinetic energies beyond the classical cut-off at 25.7 eV are reached in the Quantum Orbit Theory. Furthermore, there are subtle differences in timing between this calculation and the TSM results, particularly in the timing of the emission between 0 and 0.5 fs.

to the action of the field they change direction and return to the parent matter. In the atomic case most of these electrons do not undergo rescattering, but miss the ionic core. These quantum orbits can be dropped for a metal surface because these electrons reenter the field-free metal half-space again and are “lost”. In conclusion, the remaining orbits contributing to photoemission from a metal are direct electrons with positive drift momenta and rescattered electrons on long and short trajectories. The reduction in the number of orbits makes the solid-state case even simpler to describe than the atomic case.

We can now calculate a spectrum for photoemission from a metal surface. Fig. 2.13 displays the spectrum resulting from the relevant quantum orbits. A flat-top pulse containing two laser cycles is used in the calculation. The basis of the calculation are the saddle points shown in Figs. 2.11 and 2.12. The binding energy of 4.5 eV corresponds to the work function at a tungsten surface [92]. The spectral shape is determined from the SPA probability amplitudes (Eqs. 2.28 and 2.32).

The resulting spectrum indeed resembles all features found in above-threshold photoemission and rescattering. The pronounced decay of the direct part, the rescattering plateau and the decay beyond the cut-off energy are all reproduced. At the cut-off, an artefact of the SPA is visible: Due to the close proximity of the saddle points of long and short trajectories, the SPA breaks down. An unphysical increase of the count rate around the cut-off results. Beyond the cut-off, the contribution of short trajectories has to be disregarded because it increases strongly with increasing energy. Higher order saddle-point methods can be applied in order to regularize this spectral part [93]. The

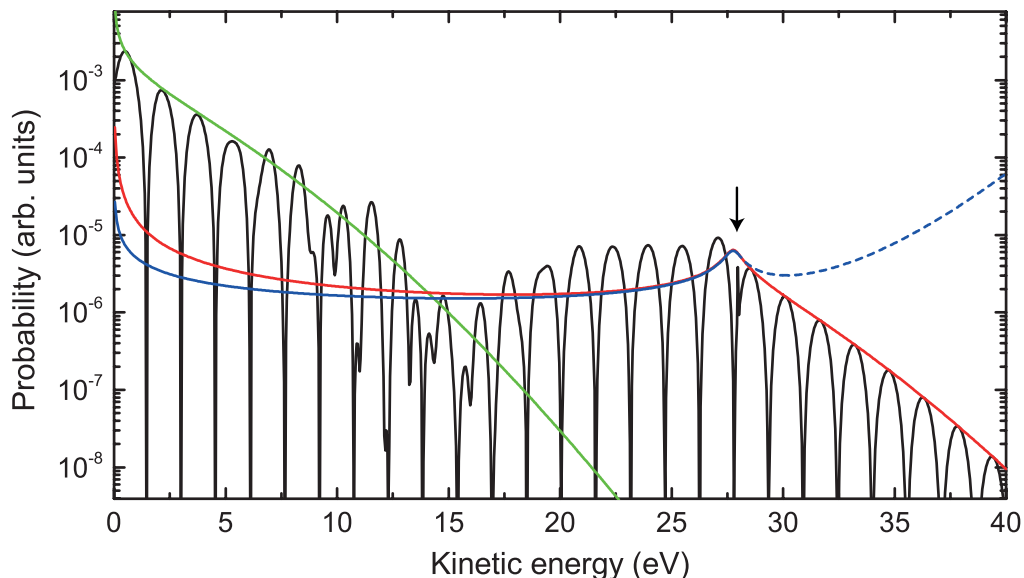


Figure 2.13: Spectrum of photoemission from a metal surface calculated with the Quantum Orbit Theory. The black curve displays the final spectrum for a two-cycle flat-top pulse with the saddle points from Figs. 2.11 and 2.12. Direct electrons (green curve), rescattered electrons on long trajectories (red curve) and short trajectories (blue curve) form the spectrum. The contributions from quantum orbits in two subsequent cycles give rise to interference in the spectral domain. Most prominently, peaks with a spacing of 1.55 eV appear throughout the spectrum, in accordance with the multiphoton interpretation of the process. The contribution of short trajectories after the cut-off (dashed blue curve) has to be ignored because it leads to the unphysical result of steadily increasing count rate. Direct and rescattered electrons interfere, which leads to the irregular features between 6 eV to 19 eV. The arrow indicates the cut-off according to the Quantum Orbit Theory, here located at ~ 28 eV.

agreement with an exact calculation, however, is still fair [84].

Another important result of the Quantum Orbit Theory can be seen: Interference structures are visible in the spectrum because the contributions of the different quantum orbits have to be added coherently. Most prominently, ATP peaks with a spacing of 1.55 eV are visible in the spectrum and their positions agree with the law for peak positions given in Eq. 2.10. We will now analyze the interference structures and their origin for the case of photoemission from a metal surface.

Interference of quantum orbits

The quantum interference of electron orbits is a typical example of the interference of different pathways to a given final state. The timing of the different orbits plays a crucial role in the emergence of spectral interference. Time and energy domain are strongly connected as we will see in the following. Following [76], we will consider two equally weighted quantum orbits, denoted as a and b , leading to the same drift momentum p . The detection probability P_p can be related to the corresponding action integrals S_a and

S_b :

$$P_p \propto \left| \exp\left(\frac{iS_a}{\hbar}\right) + \exp\left(\frac{iS_b}{\hbar}\right) \right|^2. \quad (2.34)$$

Evaluating the squared term and separating the real and imaginary parts of the action reveal an oscillatory cross term given by

$$P_p \propto A \cos\left(\frac{\text{Re } S_b - \text{Re } S_a}{\hbar}\right) + D, \quad (2.35)$$

where A is an amplitude and D is an offset leading to a positive probability P_p . The difference in the real part of the actions of the two orbits governs these oscillations. A good approximation for the real part of the action difference is given by

$$\text{Re}(S_b - S_a) \approx \frac{p^2}{2m}(\text{Re } t_b - \text{Re } t_a) \equiv E_{\text{kin}}\Delta t, \quad (2.36)$$

where t_a and t_b denote the saddle times of the corresponding trajectory and $E_{\text{kin}} = p^2/(2m)$ the kinetic energy. With this, the separation of the quantum paths in real time $\Delta t \equiv \text{Re } t_b - \text{Re } t_a$ directly enters into Eq. 2.35.

Intercycle interference

If more than a single optical cycle contributes to the photoemission, contributions originating from different cycles will interfere, leading to so-called intercycle interference. An important example is the interference of quantum orbits from two subsequent cycles of a cw light field. The dynamics of the first cycle are repeated in the second cycle. The separation in real time Δt is simply given by the optical cycle duration T_{opt} for all final energies. The action difference ΔS_p for interference of two subsequent cycles is known exactly [36] for both direct and rescattered electron and reads

$$\Delta S_p = \left(\frac{p^2}{2m} + \phi + U_p\right) T_{\text{opt}}. \quad (2.37)$$

Eq. 2.35 yields spectral fringes of the type

$$P(E_{\text{kin}}) \propto A \cos\left[\frac{(E_{\text{kin}} + \phi + U_p) T_{\text{opt}}}{\hbar}\right] + D, \quad (2.38)$$

where A is an amplitude and D is an offset. The spacing ΔE of the resulting peaks is given by

$$\Delta E = \frac{h}{T_{\text{opt}}} \equiv E_{\text{phot}}, \quad (2.39)$$

where E_{phot} is the energy of a photon in the light field and h denotes the Planck constant. We obtain the ATP peaks appearing in the model spectrum in Fig. 2.13 both for direct and rescattered electrons. The width of the peaks decreases with increasing number of cycles. For a cw light field a comb of delta functions results [49, 75]. Eq. 2.38 reveals that the positions of the peaks fully correspond to those appearing in ATP and also ATI. Effectively, we directly derived the law for the peak positions already formulated in Eq. 2.10 in Section 2.1. This illustrates the complementarity of the multiphoton picture and the interference of quantum orbits, and consequently the complementarity of the perturbative approach to photoemission and the semiclassical ansatz presented here.

Intracycle interference

Within a single optical cycle, there are three different classes of orbits that are also subject to quantum interference. This type of interference is called intracycle interference [94]. For example, the long and short trajectories of rescattered electrons interfere. Their separation in recollision time depends strongly on the final kinetic energy and amounts to $\Delta t \approx 0...750$ as for 800 nm light and final energies larger than $5 U_p$ (see Fig. 2.12). The minimum distance ΔE_{\min} between the resulting peaks is then given by

$$\Delta E_{\min} = \frac{h}{\max \Delta t} \approx 5.5 \text{ eV}. \quad (2.40)$$

For Keldysh parameters $\gamma > 1$ with only a weakly developed plateau this type of interference does not play much of a role because the peak distance is large. Intracycle interference is also visible in the example spectrum in Fig. 2.13. The overall count rate slightly drops due to interference of long and short trajectories at a kinetic energy of about 16 eV. Direct and rescattered electrons also interfere [75]. In the example spectrum, this can be seen in the irregular features in the spectral region from 6 eV to 19 eV where the amplitudes of direct and rescattered electrons are of comparable strength. A discussion of this type of intracycle interference, however, is beyond the scope of this thesis.

The interference of quantum orbits with different start times can also be interpreted as a slits-in-time experiment [95, 94, 96]. This intriguing interpretation will be taken up in Section 6.2. We will now focus on an extended model based on the TSM. It incorporates most of the features of the Quantum Orbit Theory.

2.3.4 Extended Three-Step Model

Applying the Quantum Orbit Theory to few-cycle light pulses used in many experiments is not straightforward (see, e.g., Ref. [76] for a review). For the purpose of interpreting the experimental data in the forthcoming chapters of this thesis, we developed a modified version of the Three-Step Model, the so-called extended Three-Step Model (also called extended Simple Man's Model in the publications [33, 35]). The one-dimensional model describes rescattering at a metal surface driven by few-cycle light pulses. It adds two important features to the TSM, namely effects from the binding potential and the quantum interference of different rescattering trajectories. This subsection is based on the original publications [33, 35].

Few-cycle light pulses

A light pulse of the duration of only a few optical cycles strongly confines the interaction of light and matter in time. The electric field of such a pulse is defined as

$$E_L(t) = E_0 f(t) \cos(\omega t + \phi_{\text{CE}}). \quad (2.41)$$

E_0 is the electric field amplitude and $f(t)$ is a function that describes the pulse envelope. $\omega = 2\pi c/\lambda$ denotes the (circular) frequency of the light field corresponding to the central wavelength λ and ϕ_{CE} is the so-called carrier-envelope phase. The pulse duration τ of

a light pulse is commonly defined as the full-width-at-half-maximum duration of the intensity envelope. A pulse is called few-cycle pulse if only a few optical cycles are contained within the pulse duration τ . For a few-cycle pulse, the carrier-envelope (CE) phase ϕ_{CE} plays a very important role. The CE phase is the phase difference between the maxima of the carrier wave and pulse envelope. Naturally, changing the CE phase does not affect the shape of the pulse envelope, but the shape of the optical field contained in the envelope. The CE phase provides the simplest way to control the waveform of the optical field without changing the average intensity¹⁰. It can uncover effects that are dependent on the shape of the field and insensitive to the shape of the pulse envelope. If field-driven dynamics are involved in a photoemission process, then a scan of the CE phase of a pulse should modulate the outcome of the process. Particularly recollision is sensitive to the CE phase since the dynamics of the recolliding electron is fully governed by the shape of the *field* (see, e.g., [9, 98]). The model described here is capable of modeling CE phase effects on rescattering.

Emission rate

The light field drives the first step of the extended TSM (see Fig. 2.14): An electron is liberated from the metal by an optically induced tunneling process. We chose here a Keldysh-type tunneling rate similar to the widely used Ammosov-Delone-Krainov (ADK, [74]) rate of tunneling photoionization of a single atom in a strong laser field. It agrees with the Keldysh tunneling formula (Eq. 2.8) with exponential accuracy. The tunneling rate W as a function of time t is given by

$$W(t) = \frac{C}{|E_L(t)|} \Theta[-E_L(t)] \exp\left(-\frac{4\sqrt{2m}\phi^{3/2}}{3\hbar|qE_L(t)|}\right), \quad (2.42)$$

with the normalization constant C . The metal work function ϕ replaces the binding energy I_p used in the ADK rate.

Keldysh and also ADK use in their atomic tunneling rate expressions an electric field strength corresponding to the *cycle-averaged* field intensity of a monochromatic light field. Instead we simply use the *instantaneous* field strength $E_L(t)$ in our tunneling rate in order to account for sub-optical-cycle effects. For atomic gases a closed-form tunneling rate formula for few-cycle laser pulses has been proposed [60], but for a metal surface no analogue exists. Our tunneling rate (Eq. 2.42) is highly nonlinear in the field. The emission in one optical cycle is confined to a duration significantly shorter than the duration of a half cycle (~ 500 as). The Heaviside function term in Eq. 2.42 accounts for the broken symmetry at the metal-vacuum interface.

Tunnel exit

The second step of the TSM is the propagation step where the electron motion in the laser field is treated classically. Crucial for the second step are the initial conditions of the trajectory of the electron. The conventional TSM assumes that the liberated electron

¹⁰An important alternative is a bichromatic field, for example containing fundamental light and its second harmonic [97]. Such a field enables control on a very similar level.

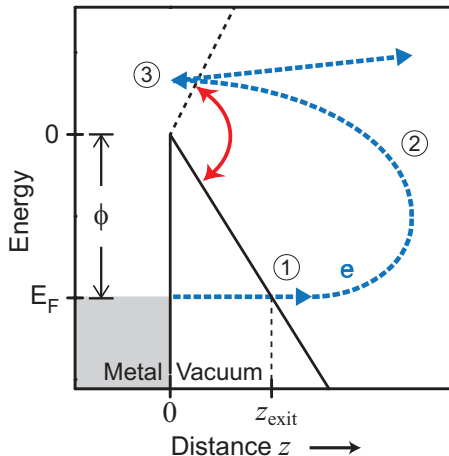


Figure 2.14: The three steps of the Extended TSM. Step ①, emission: The electron is liberated from the metal by tunneling photoemission. Here we use a tunneling probability rate that accounts for the broken symmetry at the surface: Emission takes place only when the electric field points into the metal and a tunneling barrier is formed. Step ②, propagation: The electron emerges at the (time-dependent) geometric tunnel exit z_{exit} . It is subsequently treated as a classical particle and propagates on classical trajectories in the field. We calculate the accumulated quantum mechanical phase of the electron wavepacket along the trajectory. Step ③, recollision: The electron eventually returns to the surface and recollides with it, leading to rescattering. All trajectories leading to a given final energy are summed coherently. This allows for interference of different quantum pathways. Taken from [35].

starts at the origin (metal-vacuum interface) with zero initial velocity. The emission step of the TSM neglects any displacement of the electron during the tunneling process. The more realistic Quantum Orbit Model, however, accounts for the finite potential barrier that forms between the origin and the vacuum. The emission time t_0 acquires an imaginary part because the work function is not neglected in the saddle point equation (Eq. 2.29). Due to the imaginary part of the emission time t_0 , one gets a finite tunneling distance and a tunnel exit position according to Eq. 2.26. In addition, a non-zero initial velocity results from the Quantum Orbit Model. The changed initial conditions modify the electron trajectories and lead to a higher cut-off energy than $10 U_p$ expected from the TSM. Busuladžić and coworkers [99] determined the cut-off energy with the Quantum Orbit Theory for the zero-range potential case and found a new cut-off law valid in the tunneling limit $\gamma \ll 1$:

$$E_{\text{cut-off}} \approx 10.007 U_p + 0.538 I_p. \quad (2.43)$$

The cut-off is upshifted in energy by approximately half of the binding energy I_p due to the non-zero tunneling distance.

In the extended TSM for the metal surface, we use the geometric tunnel exit as an approximation [35, 100]. It is defined as the position where a tunneled electron on the vacuum side of the “tunnel” has zero kinetic energy (see Fig. 2.14). The exit position z_{exit} as a function of emission time t_0 is given by

$$z_{\text{exit}}(t_0) \approx -\frac{\phi}{|e|E_L(t_0)}. \quad (2.44)$$

A far more rigorous approach could be realized by directly using the tunnel exit from Quantum Orbit Theory (Eq. 2.26), as proposed in [88, 89]. The present approximation, however, can be implemented without the need to solve complicated saddle-point equations for a few-cycle pulse. Fig. 2.15 displays the cut-off energy according to the extended TSM as a function of cycle-averaged intensity. The calculation was carried out for light with a wavelength of 800 nm and a work function of 5.2 eV. The result agrees well with the Quantum Orbit Theory cut-off position and its tunneling limit Eq. 2.43 at high intensities ($\gamma < 1$). At lower intensities, the extended TSM cut-off departs from the Quantum Orbit Theory results and shows irregular behavior, in particular a hump-like structure at an intensity of $1.5 \times 10^{13} \text{ W cm}^{-2}$. The geometric tunnel exit from Eq. 2.44 assumes large values for low fields, which causes the irregular behavior. However, down to an intensity of $1 \times 10^{13} \text{ W cm}^{-2}$, the approximation still predicts an upshifted cut-off energy. Measurements with atomic gases with different binding energies have clearly shown an influence of the energy of the initial state [101]. The geometric tunnel exit could explain the experimental observations even in a quantitative way. Another embodiment of the TSM including the geometric tunnel exit has been applied to successfully describe photoemission from dielectric nanoparticles [102].

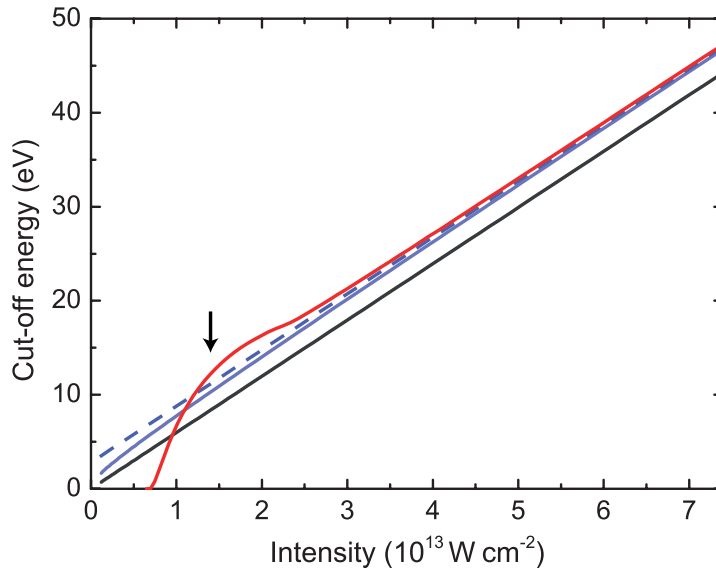


Figure 2.15: Influence of a non-zero tunnel exit on the rescattering cut-off. The cut-off position as a function of intensity according to the plain TSM (black curve) follows the $10 U_p$ law (Eq. 2.11). Corrections have to be made because the finite tunneling distance is neglected in the TSM. The Quantum Orbit Theory with the tunnel exit given by Eq. 2.26 yields an upshifted cut-off energy (solid blue curve). The dashed blue curve shows the limit of the theory in the tunneling regime (Eq. 2.43). At high intensity, the extended TSM (red curve) incorporating the geometric tunnel exit (Eq. 2.44) agrees well with the Quantum Orbit calculations. Deviations increase at lower intensities. In all calculations, the wavelength is 800 nm and the work function 5.2 eV. The arrow indicates the parameter region of the measurement presented in Chapter 6.

In an actual calculation of the propagation step, one determines the geometric tunnel exit position z_{exit} for each time instant t_0 within the pulse. We then have to keep track

of the electron's path starting at the tunnel exit with zero initial velocity. An electron released at time t_0 acquires a drift momentum $k(t_0) = qA(t_0)$ in the laser field. We now have to determine if and at which time instant t_1 recollision takes place. The condition for an electron to return to the surface is given by the equation

$$\frac{q}{m} \int_{t_0}^{t_1} [A(t_0) - A(\tau)] d\tau + z_{\text{exit}}(t_0) = 0. \quad (2.45)$$

Eq. 2.45 is the analogue to the second saddle point equation for rescattering in the Quantum Orbit Theory (Eq. 2.30). Once t_1 is determined, the final kinetic energy is found from

$$E_{\text{kin}}(t_0, t_1) = \frac{p(t_0, t_1)^2}{2m}, \quad (2.46)$$

with the final momentum

$$p(t_0, t_1) = q[2A(t_1) - A(t_0)]. \quad (2.47)$$

The calculation is straightforward and avoids imaginary time and momentum. Rescattering is modeled by scattering off an infinitely high wall at the metal-vacuum interface. The scattering amplitude is assumed to be unity for all possible incoming momenta.

Quantum interference

A serious lack of the original TSM is the absence of quantum interference. We can, however, resort to ideas from Quantum Orbit Theory: For each trajectory, we calculate the quantum mechanical phase θ of the corresponding matter wavepacket at the end of the few-cycle pulse at time instant t_p . The phase of a wavepacket is governed by the action $S(t_0, t_1)$ along its trajectory. For a given rescattering trajectory (emission time t_0 , recollision time t_1 , intermediate momentum $k(t_0)$ and final momentum $p(t_0, t_1)$) the phase is given by

$$\theta(t_0, t_1) = \frac{S(t_0, t_1)}{\hbar} = - \int_{t_1}^{t_p} \frac{[p(t_0, t_1) - qA(\tau)]^2}{2m\hbar} d\tau - \int_{t_0}^{t_1} \frac{[k(t_0) - qA(\tau)]^2}{2m\hbar} d\tau + \frac{I_p t_0}{\hbar}, \quad (2.48)$$

using the SFA definition of the quasiclassical action for rescattering (Eq. 2.21). A phase shift of the wavepacket upon scattering is neglected since all rescattered electrons undergo the same interaction with the surface. Here we assume an energy-independent phase shift. In order to retrieve a spectrum all contributions to a given final energy are summed in a coherent way, i.e., we take the phases of the corresponding wavepackets into account. The probability $P(E_{\text{kin}})$ to detect an electron at energy E_{kin} is given by

$$P(E_{\text{kin}}) = \left| \sum_j \left\{ \sqrt{W(t_0^{(j)})} \exp \left[i\theta \left(t_0^{(j)}, t_1^{(j)} \right) \right] \right\} \right|^2, \quad (2.49)$$

where j numbers the contributing trajectories. The different contributions are weighted by a probability amplitude corresponding to the emission rate $W(t_0^{(j)})$. The equation is the analogue to Eq. 2.32 in the Quantum Orbit Theory.

Results of the extended Three-Step Model

We now apply the extended TSM to a realistic example. We assume a work function of $\phi = 5.2$ eV and an ultrashort laser pulse with a full-width half-maximum (FWHM) duration of the intensity envelope of $\tau = 10.5$ fs and a center wavelength of $\lambda = 800$ nm. The peak field strength is $E_0 = 11.5$ GV m⁻¹. We chose a cosine-square envelope function that is given by

$$f(t) = \sin^2\left(\frac{\omega t}{2n}\right), \quad (2.50)$$

where

$$n = \frac{\omega\tau}{4 \arccos(2^{-1/4})} \quad (2.51)$$

denotes the number of optical cycles covered by the envelope. The pulse duration ranges already in the many-cycle domain and CE phase effects are strongly suppressed.

Fig. 2.16(a) shows the final kinetic energy E_{kin} as a function of emission time t_0 for rescattered electrons. Electrons that undergo rescattering are born right after the laser field assumes its maximum value with negative sign and the tunneling barrier is formed. Like in the original TSM, long (labeled with a) and short trajectories (labeled with b) are found. No energies beyond the cut-off are allowed in the model. An important observation can be made from the results: For each laser cycle, both the tunneling probability and the cut-off energy strongly vary. The tunneling emission rate $W(t)$ (Eq. 2.42) is highly nonlinear in the field and quasistatically follows the optical electric field $E_L(t)$. Contributions from different cycles are weighted in a different way. The cut-off energy has a more complicated dependence on the shape of the laser electric field. Both the instantaneous electric field via the tunnel exit (Eq. 2.44) and the vector potential $A(t)$ via the propagation (Eq. 2.45) influence the maximum energy. Strong acceleration during the subsequent half-cycle is required for a high cut-off energy. Therefore high cutoffs usually result from electrons that are born before the maximum of the pulse envelope. In the example calculation, this is true for the trajectories labeled 2a and 2b.

Fig. 2.16(b) displays the resulting energy spectrum from the calculation. All contributions to a given energy are added coherently. A plateau structure results that rapidly decays at high energies. The cut-off is located at an energy of 17.6 eV, in contrast to 10.5 eV derived from the $10U_p$ law. The spectrum is dominated by peaks with a spacing of the photon energy. These peaks arise due to intercycle interference (Subsection 2.3.3). The contributions from a-type trajectories from the different cycles interfere with each other. Their corresponding recollision times t_1 differ by approximately the duration of an optical cycle T_{opt} , causing an interference pattern with fringe spacing $\Delta E \approx h/T_{\text{opt}} = E_{\text{phot}}$. There is, however, a region at high energies from 14.5 eV to the cut-off where this interference pattern is absent. Fig. 2.16 reveals that only trajectories from one cycle contribute. A full Quantum Orbit Theory calculation would show that the fringe pattern is not absent, but rather loses contrast (see, e.g., [76]). The drastic caustic-like transition from presence to absence of fringes is due to the semiclassical nature of our model. There is also intracycle interference of long (a-type) and short (b-type) trajectories. This causes a fringe pattern with a spacing much larger than the photon energy. In the example calculation of Fig. 2.16, however, the second trajectory

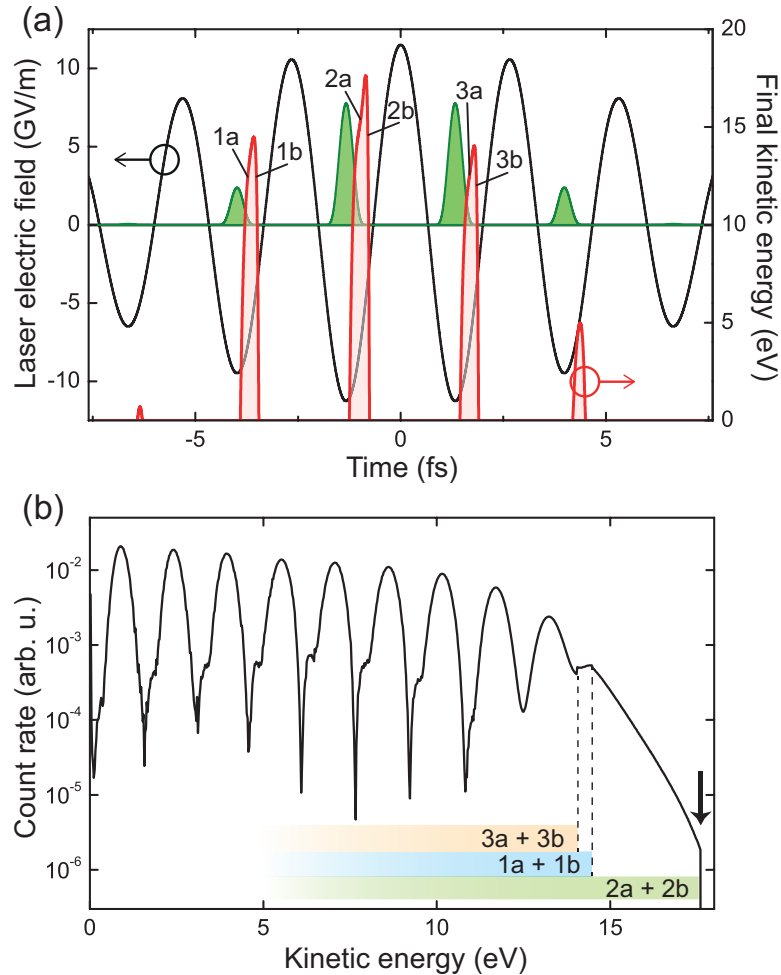


Figure 2.16: Example calculation in the framework of the extended Three-Step Model. (a) Final kinetic energy of a rescattered photoelectron as a function of its birth time t_0 . Also displayed are the laser electric field and the tunneling rate (filled curve in the center) that populates the rescattering trajectories. Rescattering is only possible within a short time window in each optical cycle. For each optical cycle numbered as 1–3, the intracycle trajectories are denoted as a (long trajectories) and b (short trajectories). The b-type trajectories do not play a role because the emission rate at the corresponding times is very low compared to a-type trajectories. (b) Photoelectron spectrum derived from the data in the upper panel by coherent summation of the trajectories. The spectrum is dominated by interference peaks with a spacing of approximately the photon energy. This is caused by intercycle interference of the a-type trajectories. For energies larger than 14.5 eV only the trajectory 2a significantly contributes, hence no spectral interference is observed. The arrow marks the classical cut-off. Parameters of the example calculation: central wavelength $\lambda = 800$ nm, pulse duration $\tau = 10.5$ fs (cosine-like cosine-square pulse), peak electric field $E_0 = 11.5$ GV m $^{-1}$, work function $\phi = 5.2$ eV.

of each cycle is only marginally populated in comparison to the first one. Therefore this type of interference plays only a minor role here and there is no trace of it in the spectra.

The presented extended Three-Step Model accounts for all main features of the recollision mechanism. First, it correctly reproduces the plateau-like shape and the high-energy cut-off found in experimental rescattering spectra. Second, it is based on the notion that the field of a laser pulse directly drives the motion of an electron liberated from the metal. Third, it includes quantum interference effects that reveal much about timing and dynamics of the recollision process. For a few-cycle laser pulse, the interference fringes and the cut-off position are strongly dependent on the CE phase, or in general, on the shape of the optical electric field of the laser pulse. We will see in the forthcoming experimental investigation that the CE phase indeed determines the electron trajectories and steers the electron motion.

2.4 Numerical approaches

In the previous sections we focused on approaches to strong-field photoemission based on the strong-field approximation. Numerical approaches are more realistic since they provide exact quantum mechanical models. However, they do not offer the same level of transparency as SFA-type models. In this section, we will briefly discuss two numerical models, namely the numerical integration of the Schrödinger equation and Time-dependent Density Functional Theory. The results of the models will be discussed when we compare theory and experiment in the forthcoming chapters.

2.4.1 Integration of the time-dependent Schrödinger equation

The time-dependent Schrödinger equation (TDSE) can be solved exactly with numerical means. Most of them rely on an approximation of the time evolution operator. The operator is given by

$$U(t, t_0) = \exp \left[-\frac{i}{\hbar} \int_{t_0}^t H(z, \tau) d\tau \right]. \quad (2.52)$$

It describes the time evolution of a single-particle wave function between times t_0 and t of a system with a time-dependent Hamiltonian $H(t)$. We use a numerical approximation scheme for $U(t_0, t)$ based on the Crank-Nicolson method [103, 104]. Taking only a very small time difference Δt into account, we can approximate the time evolution operator with

$$U(t + \Delta t, t) \approx \frac{1 - \frac{i\Delta t}{2\hbar} H(z, t)}{1 + \frac{i\Delta t}{2\hbar} H(z, t)}. \quad (2.53)$$

We also have to discretize the wave function $\psi(z, t)$ in time t and spatial dimension z . The resulting numerical grids are spaced by Δt and Δz , respectively. The spacing of both grids must be chosen so as to support the full representation and propagation of a wave function corresponding to the highest kinetic energy in the system. The Hamiltonian is discretized and written as a matrix. The second derivative in space contained in the kinetic energy term $p^2/(2m)$ in the Hamiltonian is discretized as well. The evolution of the wave function is calculated with an iterative scheme.

The implementation of the model and its description here is based on [28, 29, 35]. The TDSE is solved for a single active electron in a one-dimensional model potential. Of big importance is the shape of the potential used to describe the system (see Fig. 2.17). A narrow ($\sim 2\text{\AA}$) potential well of depth $\phi + E_F$ contains a ground state wave function. The size of the well is chosen so that the ground state exhibits a binding energy corresponding to the work function ϕ . The ground state represents the initial state in the “metal”. It is confined by an infinitely high potential wall on one side and on the other side by a potential step representing the metal-vacuum surface barrier. We also take the image-force potential into account. It represents the static image force exerted on a liberated electron by the remaining hole in the metal and is given by

$$V_{\text{im}}(z) = -\frac{q^2}{16\pi\epsilon_0 z}. \quad (2.54)$$

It is assumed here that the hole forms instantly so that any time dependence in Eq. 2.54 can be neglected. The additional potential gives a smoother shape to the surface barrier potential. The ground state wave function is determined using the imaginary time propagation method (see, e.g., [105]). The wave function has an evanescent part that penetrates into the classically forbidden (vacuum) region. This part plays the key role in the emission of wavepackets that lead to rescattering [80].

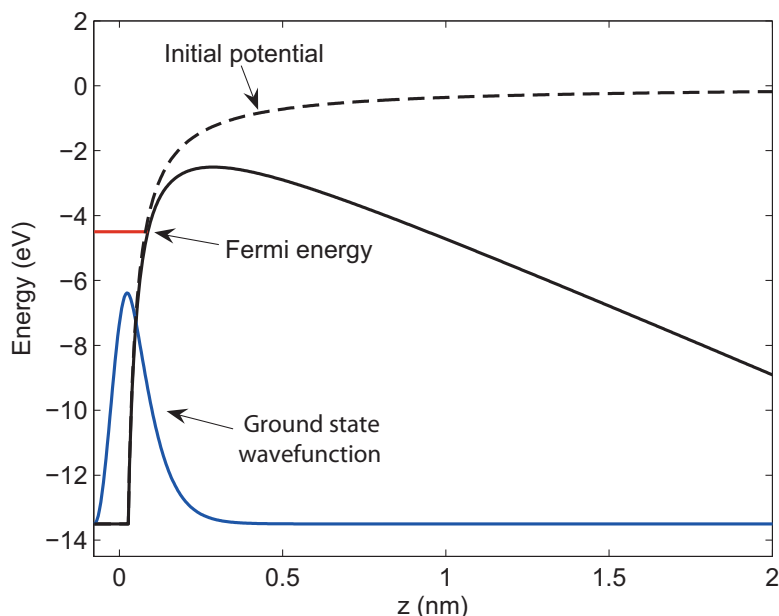


Figure 2.17: Model potential for the integration of the time-dependent Schrödinger equation. The metal potential is approximated by a narrow potential well (dashed black curve) that contains a ground state wave function (blue curve) at the Fermi level. The image force potential (Eq. 2.54) is taken into account. Additionally, there is the possibility to apply a static electric field (solid black curve).

The aforementioned infinitely high potential wall is essential for our model. It serves as a scattering potential for wave function components travelling towards the surface. The surface potential itself also causes scattering, but to a much lesser extent as numerical

tests confirm. Surface barrier and wall potential are only separated by a distance of $\sim 2\text{\AA}$. With this, the implementation of rescattering in the TDSE model is comparable to that in the extended Three-Step Model.

The laser field is defined in the same way as in Subsection 2.3.4, Eq. 2.41, but with a Gaussian envelope function

$$f(t) = \exp\left(-\frac{2 \ln 2 t^2}{\tau^2}\right). \quad (2.55)$$

In addition to the laser field, we include a static field E_{static} in this model. By applying a bias voltage to a nanotip high static fields of up to 2GV m^{-1} can be reached without significant field emission. Usually, the static field has negative sign and assists the laser field (see Fig. 2.17). The wave function is propagated in time with the Crank-Nicolson method under the influence of the external fields. The fields are switched on adiabatically. After interaction with the laser pulse, we retrieve an energy spectrum by projecting the resulting wave function onto continuum states.

Despite its *ab-initio* nature, the TDSE model incorporates many approximations. The choice of a narrow well containing only a ground state at the Fermi energy is a strong approximation. In contrast to realistic metals where electrons are delocalized, we consider a strongly localized state here. The ground state in our model has characteristics of a surface state [106]. Yalunin and co-workers compared TDSE simulations of surface photoemission from delocalized states with localized initial states [62]. If the depletion of the ground state was not too large, they found good agreement between both cases. Still the most drastic approximation in the TDSE model is the single-active electron approximation. In contrast, a metal is characterized by many electronic states that interact with each other. This shortcoming can be addressed by time-dependent density functional theory, which is by far the most realistic of all models presented here.

2.4.2 Time-dependent density functional theory

A common approach to describe multi-electron systems is the time-dependent density functional theory (TDDFT) [107, 108]. It can be applied to photoemission from a metal surface. TDDFT can describe a quasi-free electron gas including electron-electron interaction and its effects such as polarization of the charge density by the laser field and the screening of the laser field inside the metal. The multi-electron system is mapped onto an effective system of one-body pseudo wave functions $\psi_k(z, t)$. Each wave function obeys a differential equation similar to the time-dependent Schrödinger equation, the so-called time-dependent Kohn-Sham equation. The equation includes electron-electron interaction by virtue of the electrostatic and exchange-correlation terms in the Hamiltonian.

The TDDFT model was applied to nanotip photoemission by Wachter and co-workers [34, 36] using an one-dimensional ansatz. The reaction coordinate is the surface normal direction. This approximation is justified because the system's natural length scale, the de-Broglie wavelength of the electrons at the Fermi level, is on the order of 4\AA . This quantity is much smaller than typical nanotip radii of curvature ($5 \dots 50 \text{ nm}$). Moreover, a fully self-consistent treatment of the system in three dimensions is currently

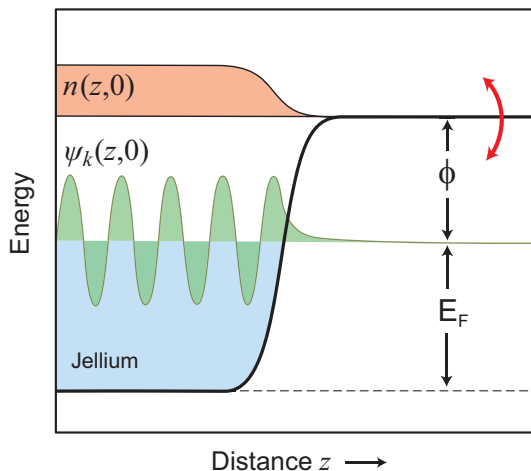


Figure 2.18: Schematic picture for the time-dependent density functional theory. A potential slab (“jellium”) contains many electronic states that generate a surface pseudopotential (black curve) in a self-consistent way. A pseudo wave function $\psi_k(z, 0)$ corresponding to a state at Fermi energy E_F is displayed (green curve). The weighted sum of all occupied electronic states forms the local electron density $n(z, 0)$. The influence of external fields is introduced via a time-dependent potential term. Rescattering is enabled by an atom-like potential term (not shown). Inspired by [109].

not feasible due to computer power requirements that can not be met even today. Exchange and correlation are included within the adiabatic local density approximation (LDA) [108]. Within the LDA, the exact exchange-correlation potential is approximated by the exchange-correlation potential for a free electron gas with the local electron density. The long-range image-force potential is not included explicitly, but can be included in the surface pseudopotential in the same way as in TDSE model. The time-dependent local electron density $n(z, t)$ is the defining quantity in the TDDFT. It can be expressed in terms of the pseudo wave functions $\psi_k(z, t)$ as

$$n(z, t) = \sum_{k=1}^{n_{\text{occ}}} c_k |\psi_k(z, t)|^2. \quad (2.56)$$

c_k are weighting coefficients and n_{occ} denotes the number of occupied electronic states up to the Fermi level. The Kohn-Sham equations with the LDA in the implementation of Wachter and co-workers reads

$$i\hbar \frac{\partial \psi_k(z, t)}{\partial t} = \left\{ -\frac{\hbar^2}{2m} \frac{\partial^2}{\partial x^2} + V[n(z, t)] + V_{\text{ext}}(z, t) \right\} \psi_k(z, t). \quad (2.57)$$

The potential term $V[n(z, t)]$ depends on the local density and is chosen in a way to generate the appropriate potential with the correct Fermi energy E_F and work function ϕ . The model implements a so-called jellium slab, a potential well of finite size (see Fig. 2.18 for an illustration). In essence, the model then describes an interacting quasi-free electron gas with fully delocalized states (for details refer to the original publications [34, 36]). V_{ext} denotes the potential created by the external fields. It includes the laser field in the dipole approximation and in addition a static electric field.

In order to account for rescattering, the potential in Eq. 2.57 is extended by an additional term V_{atom} . It is given by

$$V_{\text{atom}} = -\frac{1}{1 + |z|} \exp\left(-\frac{|z|}{\lambda_{\text{TF}}}\right) \quad (2.58)$$

and describes a screened Coulomb potential at the position of the first atomic layer. It is screened with the Thomas-Fermi screening length for an electron gas, given by

$$\lambda_{\text{TF}} = \sqrt{\frac{2\epsilon_0 E_{\text{F}}}{3q^2 n}} \approx 0.5 \text{ \AA}. \quad (2.59)$$

n denotes the electron density and E_{F} is the Fermi energy measured with respect to the bottom of the pseudopotential. A single atomic site at the surface is sufficient to induce rescattering. The strength of the potential essentially determines the scattering amplitude.

The TDDFT model is the only manageable model that goes beyond the single active electron approximation. This approximation is characteristic for models from atomic physics. The TDDFT model can be used to model rescattering at a metal surface and gain insight into the effects of electron-electron interaction on photoemission dynamics. It can be applied for arbitrary field shapes and offers the possibility to add a static electric field. The only drawback is the absence of the image force and in general the absence of long-range interaction in the model. We will compare experimental data with TDDFT model calculations in Chapter 5.

2.5 Enhanced optical near-fields at nanotips

In the previous parts we focused on the description of photoemission from metal surfaces in external fields. In this thesis, the experimental investigation of surface photoemission is carried out with metal nanotips. The geometry of the electron emitter has to be accounted for in the models described above. The presence of the nanostructure strongly affects the local optical field: If a metal nanostructure is irradiated with light of a wavelength much larger than the structure size, optical near-fields are excited [110, 111]. In essence, the local optical field is strongly enhanced in the vicinity of the nanostructure. Moreover, the light field is strongly localized near small structures and sharp edges. Near-field optics or nano-optics, as it is oftentimes called, is a rapidly growing field that explores near-field enhancement (see [112] for a review). Applications of nano-optics include scanning near-field microscopy (SNOM, [113]) and tip-enhanced Raman spectroscopy (TERS, [114]), both of which involve nanotips. The nanotip facilitates localization of light far below the diffraction limit. This fact enables measurements with a resolution of down to 10 nm. The following discussion of near-field enhancement at nanotips is based on [115, 37].

Commonly, near-field enhancement at nanostructures is thought to be based on three mechanisms of different nature: First, so-called geometric field enhancement takes place. The discontinuity of the dielectric constant at the metal-vacuum interface leads to the accumulation of surface charge under light irradiation. The surface charge then leads to

a strong local electric field due to the tiny size of the nanostructure. The oscillation of the charge induced by the field translates into the oscillatory behavior of the near-field. This effect can be regarded as the time-dependent analogue of the electrostatic lightning rod effect. Second, an antenna resonance can cause field enhancement. If the structure has a size of an odd multiple of half of the wavelength, the resulting resonance can exceed the effect of the other mechanisms significantly. Last, a plasmonic effect leads to strong enhancement. Plasmonic field enhancement requires a plasmonic material like gold or silver and a geometry supporting the excitation of a plasmon resonance. The plasmonic effect is important when the optical frequency is close to the resonance frequency. The geometric mechanism is universal for all materials and a broad range of wavelengths, whereas the other effects depend critically on the choice of material, geometry and wavelength.

The excited near-field is also responsible for the photoemission and electron dynamics in our nanotip-based system. In a theoretical investigation [115, 37], we explored the parameter dependence of the near-field excitation in our nanotip system. We performed a numerical simulation of Maxwell's equations for the geometry of typical nanotips. Here we only briefly describe the simulation and its outcome.

A numerical solution of the time-dependent Maxwell equations in a complicated geometry can be carried out using a finite-difference time-domain (FDTD) method [116]. In the FDTD method, the optical electric and magnetic fields are discretized in space. Maxwell's equations in a discretized representation are used to calculate the time-dependent fields in an iterative procedure. We used a commercially available Maxwell solver¹¹ and a three-dimensional representation of a nanotip geometry. The geometry of a typical tip is given by an apex of approximately hemispherical shape supported by a shank with a small opening angle. Fig. 2.19 displays a cut through the structure of a typical tungsten tip. Here the tip radius of curvature at the apex is 30 nm and the total opening angle is 10° , in agreement with microscope images from tips (see Fig. 3.5 in Subsection 3.3.1). A linearly polarized optical field with a wavelength of 800 nm irradiates the tip. The field is polarized parallel to the tip's symmetry axis ($z = 0$). Its wave vector is oriented perpendicular to this axis. This scenario corresponds to grazing incidence at a flat surface. In order to avoid antenna resonances, the light is confined to a focal spot of $2\ \mu\text{m}$. This assures that the simulation boundaries are not significantly irradiated with light (for details see [115, 37]).

Fig. 2.19 shows the results of a FDTD calculation with the aforementioned parameters. Tungsten has been chosen as tip material. It has a dielectric constant of $\epsilon \approx 4 + 19i$ at 800 nm wavelength. It is instructive to take a look at the time average of the electric field in space. The electric field is strongly enhanced at the tip surface and rapidly decays into free space. On the tip's symmetry axis ($z = 0$), a $1/e$ decay length L can be defined that is on the order of the tip radius of curvature. The enhancement effect is concentrated on the apex of tip. This and the pronounced decay are consistent with the geometric mechanism where oscillating surface charges lead to high fields in the vicinity of sharp structural features. Usually, one defines a field enhancement factor which is given by the ratio of the maximum amplitude of the enhanced field and the amplitude of the incident field. Here it is about 3.4.

¹¹Lumerical 7.0.1.

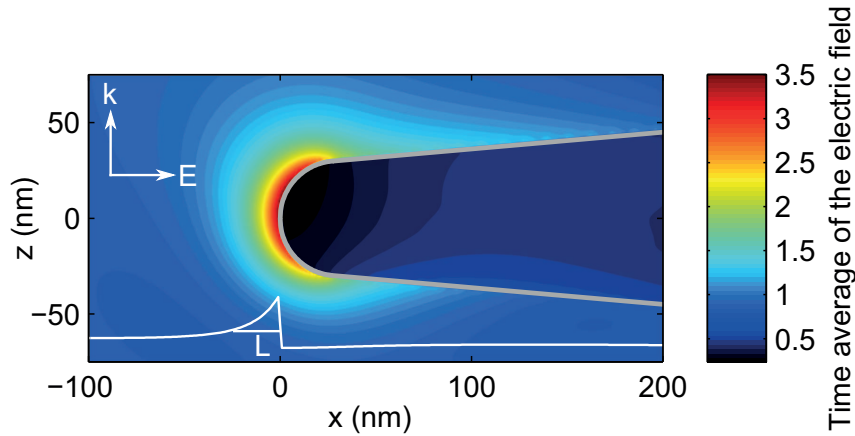


Figure 2.19: Optical field enhancement at a metal nanotip. Time-average of the optical electric field in vicinity of a sharp nanotip calculated with a numerical method. The color encodes the ratio of the local field average and the amplitude of the incident light. The field is enhanced at the surface of the apex by a factor of up to 3.4, whereas the inside of the metal is nearly field free. Also shown is the field along $z = 0$ (white curve). The near-field rapidly decays into free space with the $1/e$ decay length L . The tip has a radius of curvature of 30 nm and is made from tungsten. The incident electric field E (wavelength $\lambda = 800$ nm) with wave vector k has is polarized parallel to the tip axis ($z = 0$). Taken from [37].

When using few-cycle laser pulses the broadband response of the system becomes important. It is not clear *a priori* that the temporal shape of the near-field resembles that of the incident field without any distortion [34]. In order to investigate this it is helpful to take a look on the time-dependence of the effect. Fig. 2.20 shows the time evolution of the incident and enhanced fields at the tip surface at $z = 0$, here for a tungsten tip with 5 nm radius. The pulse duration is 5 fs and its center wavelength is 800 nm. It can clearly be seen that the shape of the pulse is still a few-cycle pulse and does not undergo heavy distortion. However, two effects are observed. First, the carrier-envelope phase of the enhanced pulse is shifted, here by 0.4π . The enhanced field is delayed with respect to the incident field due to a finite response time of the system. Also the peak of the envelope is shifted by a small amount of time (~ 70 as). These shifts are sensitive to the material and the geometry of the tip. Second, a weak excitation of the field remains after the end of the driving pulse. In a good approximation, the enhanced field can be described as a few-cycle pulse with an enhanced amplitude and a shifted carrier-envelope phase. The pulse tail due to excitation can be neglected because it does not play a role in a highly nonlinear process. The duration of the enhanced pulse is approximately the same as the driving pulse. Hence a regular few-cycle pulse is sufficient for calculations with the photoemission theory models described above.

Fig. 2.21 shows calculated field enhancement factors as a function of tip radius for tungsten, gold and silver nanotips. In contrast, gold and silver are plasmonic materials. They have dielectric constants with negative real part and small (< 5) imaginary part at near-infrared wavelengths. In general, the results agree with the geometric mechanism of field enhancement: The field enhancement increases when decreasing the tip radius. The ratio of structure size and driving wavelength decreases, leading to higher fields. With nanotips made from tungsten, gold and silver, field enhancement factors of up

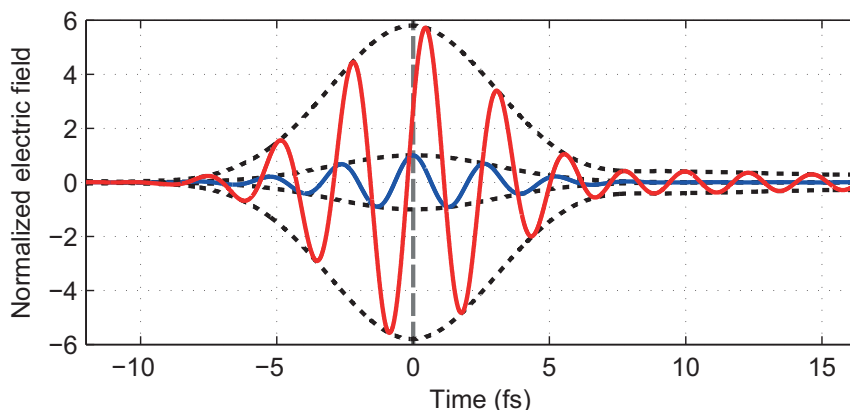


Figure 2.20: Time evolution of a near-field driven by a few-cycle pulse. A laser pulse with a center wavelength of 800 nm and a duration of 5 fs (blue curve) irradiates a tungsten tip with a radius of 5 nm. The enhanced field over time at the tip surface along $z = 0$ is shown by the red curve. Evident from the figure is the enhanced amplitude (field enhancement factor 5.8) and a shift of the carrier-envelope phase. The enhanced field is delayed with respect to the driving field. After the incident pulse has ended, an excitation of the enhanced field remains. Courtesy of S. Thomas.

to 6 are possible at an experimentally feasible tip radius of 5 nm. It is, on first glance, puzzling, however, why nanotips from plasmonic materials show similar field enhancement values as tungsten. One might assume that plasmonic materials enable larger field enhancement factors due to the plasmonic mechanism of field enhancement. In contrast, the behavior found here suggests that the geometric mechanism is dominant for nanotips. Calculations with arbitrary dielectric constants indeed show that in most cases the geometric mechanism prevails [37].

The theory models describing photoemission from the tip surface are driven with the *enhanced* field amplitude. However, there is an intricate interplay of field enhancement and photoemission because the same pool of electrons is responsible for both. The only model that is able to selfconsistently incorporate field enhancement is the TDDFT (Subsection 2.4.2). A TDDFT calculation in three dimensions, however, is elusive even with today's computer power. An alternative is an integration of TDDFT on small spatial scales with Maxwell's equations on large scales [117]. This method, however, is still in its very beginnings. We have to resort to a disentangled treatment of field enhancement and photoemission by feeding the photoemission models with results from FDTD simulations.

The field enhancement effect is very helpful since it strongly relaxes the requirements on the laser system. For example, a peak intensity of $4 \times 10^{11} \text{ W cm}^{-2}$ translates into an enhanced intensity of about $1 \times 10^{13} \text{ W cm}^{-2}$ at the tip apex assuming a field enhancement factor of 6. It is possible to enter the strong-field photoemission regime at these intensities without the need for an amplified laser system.

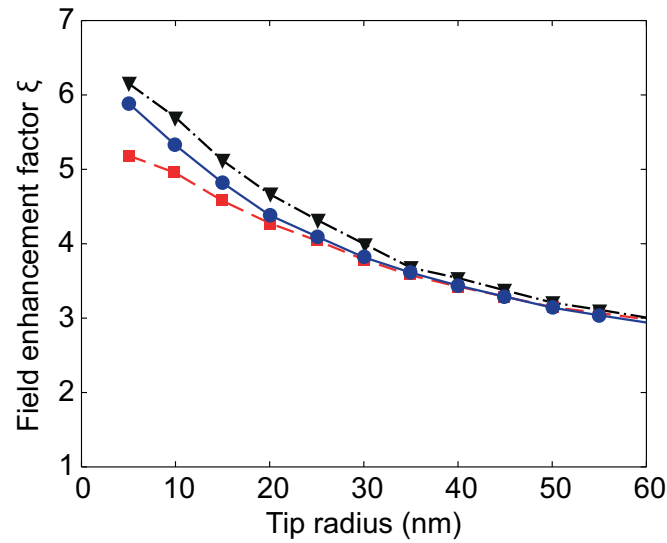


Figure 2.21: Dependence of field enhancement on tip material and radius. Field enhancement factor as a function of tip radius for tungsten (blue circles), gold (red squares) and silver (black triangles). The colored lines serve as a guide to the eyes. For decreasing tip radius the field enhancement significantly increases up to a factor of 6 for 5 nm tips. This behavior is consistent with the geometric mechanism of field enhancement. Nanotips from plasmonic materials (here gold and silver) behave similarly to tungsten. Taken and modified from [37].

3 Experimental methods and setup

At the core of this thesis lies an experimental investigation of laser-induced electron emission from sharp metal tips using few-cycle near-infrared laser pulses. In general, the experiment requires a versatile setup involving many different techniques. In this chapter, we will describe the basic setup and fundamental methods used in the experiments in the upcoming chapters. More details can be found in [118, 119]. The experiment consists of an optical system for the generation of phase-stable few-cycle laser pulses (Section 3.1) and of a vacuum chamber that contains the tip and detectors (Section 3.2). Methods for nanotip production and characterization are described in Section 3.3.

The main feature of the experimental setup is the capability to measure photoelectron spectra and to use carrier-envelope (CE) phase stable few-cycle laser pulses. An electron spectrometer allows for an investigation of different emission processes that cannot be distinguished otherwise (see Section 2.1) and for CE phase effects in spectra. CE phase stabilized pulses enable the observations of effects that are not only sensitive to the average intensity that follows the pulse envelope, but that are also sensitive to the temporal shape of the underlying electric field.

3.1 Optical setup

In the following we describe the optical system of the setup, which has been designed to minimize the laser pulse duration at the emission site. It also includes a CE phase stabilization scheme.

Laser system

The laser system used in the experiment is a commercial Kerr-lens mode-locked titanium:sapphire (Ti:sa) laser oscillator¹. It is pumped by a frequency-doubled neodymium-doped yttrium aluminum garnet laser² with 6 W average power at 532 nm wavelength. The laser oscillator produces pulses with a duration of about 6 fs at a center wavelength of ~ 800 nm and a repetition rate of 80 MHz. The maximum average output power is ~ 760 mW in mode-locked operation. The optical spectrum of the oscillator output is depicted in Fig. 3.1(a). It spans from 630 nm to 1020 nm and supports a FWHM intensity duration of about 5.1 fs assuming the ideal case of a flat spectral phase. Interferometric autocorrelation enables an experimental estimate of the duration of the pulse. Fig. 3.1(b) displays such a trace. The experimental trace is in good agreement with a trace of an ideal pulse calculated from the spectrum by Fourier transformation. This suggests that laser pulses with a pulse duration only slightly larger than 5.1 fs are

¹VENTEON PULSE : ONE Power edition.

²Coherent Verdi V6.

generated by the oscillator. We estimate an upper limit of 6.5 fs. With an optical cycle duration of about 2.7 fs, the pulse duration corresponds to about 2 to 2.5 optical cycles. All operational parameters (center wavelength, pulse duration, optical spectrum and output power) vary slightly from day to day and the oscillator requires regular readjustment. The experimental spectrum in Fig. 3.1 shows that the center wavelength is about 820 nm, corresponding to a photon energy of 1.51 eV.

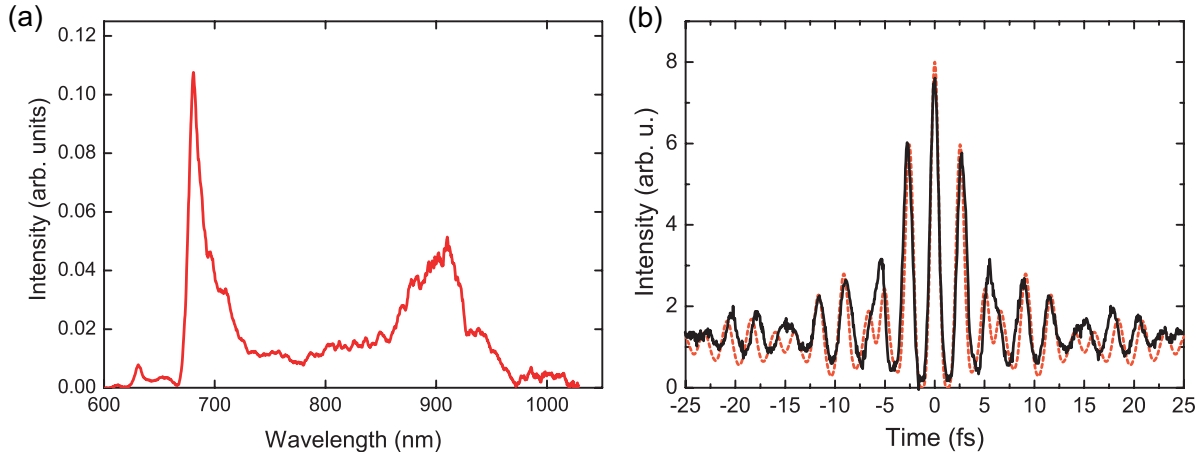


Figure 3.1: Properties of laser light from the Ti:sapphire oscillator. (a) Exemplary optical spectrum. The spectrum is centered around a photon energy of 1.51 eV, corresponding to a center wavelength of 820 nm. (b) Interferometric autocorrelation trace of the laser pulses. An experimental trace (black curve) is compared with a calculated trace (dotted red curve) that corresponds to the spectrum in (a). For the calculation, a flat spectral phase was assumed. The good agreement suggests that the experimental pulse duration is only slightly larger than the optimum pulse duration of 5.1 fs.

Dispersion management and focusing

A main task of the optical setup is to conserve the ultrashort pulse duration along the optical path to the experimental chamber. The chromatic components in the broad spectrum undergo different group velocity dispersion (GVD) when propagating through media. At 800 nm wavelength, media show positive group velocity dispersion. This means that blue components are delayed with respect to red components, resulting in an effective increase of the pulse duration. In our setup, we introduce as little material as possible into the beam path and hence minimize positive GVD. Furthermore, silver-coated mirrors are used that allow for almost unity reflection for a broad wavelength range without introducing dispersion.

The optical setup is depicted in Fig. 3.2. Double chirped mirrors (DCMs) introduce negative GVD and allow for recompression of broadened pulses and partial compensation of third-order dispersion effects. DCMs are used to compensate for positive GVD along the optical path. Several optical elements made from fused silica and barium fluoride (BaF_2) as well as air are responsible for pulse broadening. Two stages of DCM recompression are used: Four bounces off a pair of DCMs optimized for fused silica³ are

³These DCMs have been designed and manufactured by V. Pervak, LMU Munich.

introduced close to the output port of the laser oscillator, denoted as DCMs 1. Furthermore, two bounces off another pair of DCMs⁴ are used (DCMs 2), specially designed for compensation of BaF₂ and air. Since the magnitude of recompression can only be adjusted by the number of bounces at the DCMs in a step-wise fashion, a movable fused silica wedge pair and a BaF₂ wedge pair are used for finetuning positive GVD.

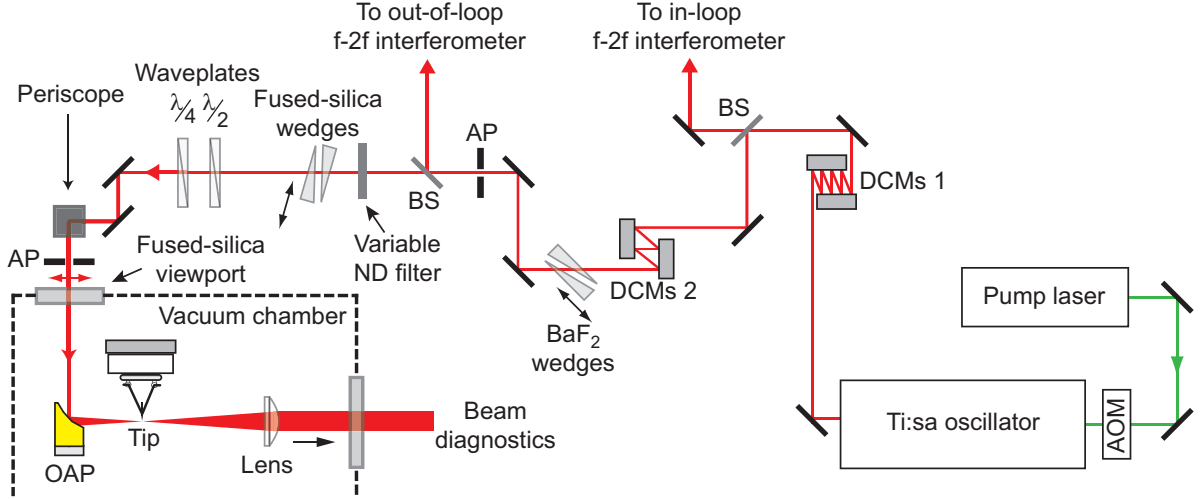


Figure 3.2: Optical setup. A Ti:sa laser oscillator generates 6 fs pulses at a center wavelength of ~ 800 nm. The pump power is regulated by an acousto-optical modulator (AOM). Dispersion compensation is performed with two pairs of double chirped mirrors (DCMs). Movable wedges made from fused silica and barium fluoride (BaF₂) are used for finetuning. Two beam splitters (BS) feed two interferometers for carrier-envelope phase stabilization. A variable neutral density (ND) filter serves for adjusting the output power. The polarization can be tuned with two waveplates. Apertures (AP) are used for beam alignment. Inside the vacuum chamber, the beam is tightly focused on the tip with an off-axis parabolic (OAP) mirror. The beam is then recollimated by a lens and used for diagnostics.

Two beam splitters (BS) pick up a part of the light to two f -to- $2f$ interferometers for CE phase stabilization. A Michelson interferometer (not shown) can be used for interferometric autocorrelation measurements using a second-harmonic generation (SHG) crystal or the tip as nonlinear element [28]. About 40 mW of laser power is directed to the experimental chamber and the nanotip. The incident laser power can be tuned with a variable neutral density (ND) filter. Moreover, the polarization of the beam can be tuned using broadband half-wave and quarter-wave waveplates. Usually, the polarization is chosen to be linear and parallel to the tip's pointing direction. This configuration assures that a high field enhancement factor can be attained at the tip apex (see Section 2.5).

The beam enters the vacuum chamber through a fused-silica viewport. A gold-coated off-axis parabolic (OAP) mirror with an effective focal length of $f = 15$ mm focuses the beam down to a waist of $w_0 = (2.4 \pm 0.4) \mu\text{m}$. The focal waist size w_0 is defined as the $1/e^2$ radius of the intensity profile. The attained waist size is highly sensitive to alignment. With different beam profiles and alignment of the optical elements, smaller

⁴Nanolayers NANE0 DCM7 blue/green.

focal waist sizes down to $1.8\ \mu\text{m}$ could also be attained. For Gaussian laser pulses, the peak laser electric field E_0 is related to the average laser power P_{avg} via [120]:

$$E_0 = \left(\frac{8\sqrt{\ln 2}}{\pi^{3/2}} \frac{Z_0 P_{\text{avg}}}{\tau f_{\text{rep}} w_0^2} \right)^{1/2}. \quad (3.1)$$

Here $Z_0 = 377\ \Omega$ is the impedance of free space and f_{rep} the laser repetition rate. Assuming a laser power of 40 mW and the aforementioned spot size and a pulse duration of 6 fs, a peak field of $2.6\ \text{GV m}^{-1}$ can be reached. The corresponding peak intensity is $8.7 \times 10^{13}\ \text{W cm}^{-2}$. Including the field enhancement effect with a factor of 6, a near-field strength of up to $15\ \text{GV m}^{-1}$ can be attained at the tip surface. This field translates into an intensity of $3 \times 10^{13}\ \text{W cm}^{-2}$, placing the experiment in the strong-field regime at a Keldysh parameter of $\gamma \sim 1$. Due to the field enhancement effect, the strong-field regime can be reached with a simple laser oscillator only, without the need for an expensive and complicated amplified system.

After alignment of the focal spot, the tip is placed in the focus with the help of a three-dimensional piezo-based nanopositioning system⁵. The tip's shadow can be observed in the recollimated beam and maximum electron emission indicates optimum positioning.

Carrier-envelope phase stabilization

Due to intensity fluctuations in the pump laser beam and instabilities of the optical elements in the laser oscillator cavity, the CE phase at the oscillator output is highly unstable. In our experiment, we would like to investigate the effect of the CE phase on the electron emission and hence need to stabilize the phase of the laser pulses. The carrier-envelope offset frequency f_{CEO} corresponds to the average pulse-to-pulse CE phase slip $\Delta\phi_{\text{CE}}$ over the temporal separation of subsequent pulses $1/f_{\text{rep}}$. If f_{CEO} can be stabilized to zero, the phase ϕ_{CE} is the same for all pulses, hence every pulse has the same shape of the optical electric field. f_{CEO} can be measured and stabilized with the help of an f -to- $2f$ interferometer [8, 121]. For this purpose, light pulses with a spectrum covering more than a frequency octave have to be generated. In the interferometer, this light is superimposed with its second harmonic. Fundamental and frequency doubled light have frequency components in the same spectral region, namely in the high-frequency part of the fundamental. The CE offset frequency can be deduced simply from the beatnote signal of the interferometer in the spectral overlap region. This frequency comb technique has been originally devised for high-precision frequency metrology, but has found a wide range of other applications. Here we only describe the very basics of the implementation of the CE phase stabilization in the experiment. Further details can be found in [38, 119].

The Ti:sapphire oscillator does not generate an octave-spanning spectrum. Therefore the spectrum has to be broadened to more than a full octave in a coherent way. For this purpose we focus the beam into a photonic crystal fiber (PCF) where self-phase modulation and spectral broadening take place. Another challenge is the requirement to stabilize f_{CEO} to zero. If f_{CEO} is locked to zero, the signal on the beatnote detector is ideally constant over time. Fluctuations between laser oscillator and beatnote detector,

⁵Slip-stick motion positioners ANxyz101 from attocube Systems.

background light and other effects, however, can then strongly distort the signal and add unwanted noise. An AC signal is less prone to these effects. Therefore an acousto-optical modulator (AOM) was inserted into the fundamental arm of the interferometer. We use light from the first diffraction order that is frequency-shifted by the AOM driving frequency f_{AOM} . If f_{CEO} is zero, the beatnote signal will then be equal to f_{AOM} . The beatnote is found at a wavelength of about 500 nm and detected by an avalanche photodiode. 80 mW of input laser power is sufficient for a successful operation of the interferometer. The beatnote signal is compared to a reference signal with frequency f_{AOM} and an error signal is generated. A simple way to feed the error signal back into system is modulating the pump power. For this purpose, an AOM is placed into the pump laser beam. The error signal determines the amplitude of the driving signal for this AOM and hence the amount of light scattered away from the zeroth diffraction order. With this, a full feedback loop is constructed and an electronic lock of the CE phase is possible. The CE phase can be adjusted by changing the relative phase between AOM driving frequency and the reference signal. The f -to- $2f$ interferometer used in the feedback loop is called in-loop interferometer.

A second (“out-of-loop”) f -to- $2f$ interferometer is used to monitor the performance of the stabilization loop. Nominally, about 140 mW of laser power drives this interferometer. The interferometer does not use a PCF but employs a monolithic design with a periodically poled lithium niobate (PPLN) crystal [122]. It supports both self-phase modulation and second-harmonic generation. The beatnote is detected in the green part of the spectrum. The out-of-loop detection shows that the stabilization loop performs well, with a root-mean-square phase variation below 100 mrad/min.

3.2 Vacuum chamber and detection system

For the experiment, an ultrahigh vacuum (UHV) with a base pressure of 10^{-8} mbar or better is required in order to avoid fast surface contamination of the nanotip. Here a vacuum with a pressure of about 3×10^{-10} mbar is used for laser-induced electron emission. We only give a brief overview of the vacuum setup and the detection systems. More details can be found in [118, 119].

The base pressure of about 3×10^{-10} mbar is attained with the help of a rotary-vane roughing pump (intermediate pressure $\sim 10^{-3}$ mbar) and a turbomolecular pump. The stainless-steel vacuum chamber is routinely baked out at a temperature of about 120 °C. In order to reach the final base pressure, an ion getter pump and a titanium sublimation pump assist the other pumps. The chamber can be backfilled with high-purity gases using a dosing valve for field ion microscopy.

Fig. 3.3 shows a sketch of the chamber and the detectors. The nanotip is held on a v-shaped wire and points towards one of the detectors. High-voltage biasing as well as resistive heating of the tip can be performed. The detection system should be able to provide high spatial resolution imaging and spectrally resolved measurements of electron emission from the tip. For this purpose, two different detectors can be used: A microchannel plate (MCP) detector and an electron spectrometer. Linear motion feedthroughs enable *in-situ* exchange of the detectors. With the help of the MCP detector, tip characterization is possible with field emission and field ion microscopy (see subsection 3.3.3).

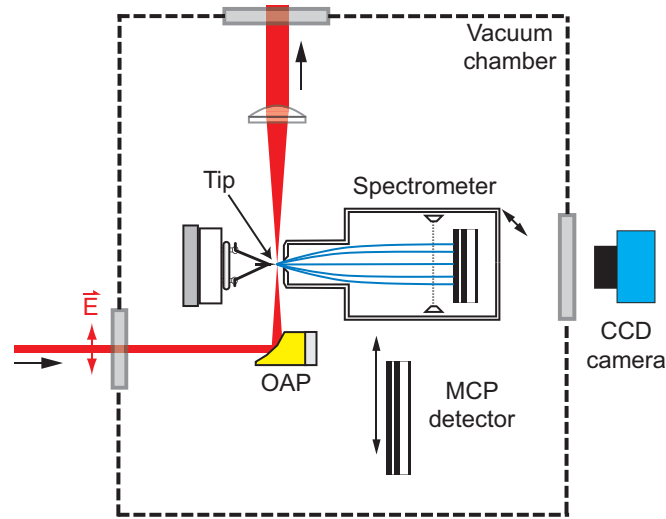


Figure 3.3: Sketch of the vacuum chamber setup. The vacuum chamber, here in top view, is operated at a base pressure of 3×10^{-10} mbar. The laser-illuminated tip is mounted on a v-shaped wire. Electrons emitted from the tip (trajectories indicated by blue curves) can be detected either with a microchannel plate (MCP) detector or a retarding field electron spectrometer. The former serves for high spatial resolution imaging of the electron emission pattern, whereas the latter is used to record electron energy spectra. More details can be found in [118, 119].

The MCP detector is located at a distance of about 4 cm from the nanotip. Its active area has a diameter of about 4 cm. In a measurement with the MCP detector, the tip is biased with a negative voltage U_{tip} and serves as a cathode. The front side of the MCP is kept on ground potential and serves as an anode. The back side is biased with a high positive gain voltage U_{gain} of up to 2 kV. The phosphor screen of the detector is biased with +4 kV. In this configuration, the MCP serves as an electron multiplier with high spatial resolution. The gain factor can be as large as 10^7 , enabling single electron detection with a dark count rate of less than 5 electrons per second. The amplified current can be measured at the phosphor screen. The electron emission pattern is imaged with a CCD camera outside of the vacuum chamber.

Electron spectrometer

With the help of linear motion feedthroughs, the MCP detector can be exchanged with an electron spectrometer. The spectrometer that is used in the experiment⁶ is a retarding field spectrometer, first implemented by E. W. Müller in 1936 [19]. The retarding field spectrometer features a fine mesh grid that is biased with voltage U_{grid} , measured with respect to the tip voltage. The grid serves as a high-pass energy filter for incoming electrons. Only electrons with a minimum kinetic energy of $-|e|U_{\text{grid}}$ pass. Electron energies measured with this type of spectrometer are usually referenced to the Fermi energy E_{F} . This thesis follows this convention common in surface science.

Recording the count rate transmitted through the filter grid as a function of the grid

⁶Staib Instruments RFA2000 retarding field analyzer.

voltage U_{grid} yields an integrated electron spectrum. The actual spectrum is retrieved by subsequent differentiation and smoothing of the recorded curve. In strong-field science, usually time-of-flight (TOF) spectrometers are used to measure photoelectron spectra. With a repetition rate of 80 MHz, however, arrival times of electrons from two subsequent laser pulses easily overlap. Furthermore, the operation of such a spectrometer is only possible with pulsed (laser-triggered) electron emission. Continuous electron emission, for example from field emission (see below), can not be resolved spectrally with a TOF spectrometer. A viable alternative to a retarding field spectrometer would be a hemispherical electron analyzer. This detector can also provide angular resolution in addition to spectral resolution. Both spectrometer types are based on electrostatic energy filtering and are capable of measuring continuous electron currents.

In the experiment, the tip is kept on ground potential and electrons emitted from the tip are accelerated to the spectrometer's entrance aperture that is biased with a positive extraction voltage U_{extr} . Using a current preamplifier connected to the tip, it is then possible to measure the total current drawn from the tip while recording electron spectra. This is particularly useful for monitoring the stability of the tip emission current over time. Only electrons emitted in forward direction are detected by the spectrometer. The acceptance angle of the spectrometer is not known, but estimated to be significantly smaller than 20° . In the best case, a total detection efficiency of 10^{-2} was found from a comparison of the total current with the count rate detected at the spectrometer's MCP detector. The resulting integrated electron spectrum is then numerically differentiated and smoothed with a Savitzky-Golay algorithm [123].

The electron spectrometer has a resolution of about 80 meV. This value has been estimated from a comparison of an experimental electron spectrum of field emission with its well-known theory counterpart [124]. Besides emitter instability, shot noise constitutes the main source of noise on spectral measurements (see [119] for a discussion).

3.3 Metal nanotip preparation and characterization

Nanometer-scale emitters with many different geometries can be fabricated by a wide variety of techniques. Here a class of emitters has been chosen that is particularly simple to fabricate: metal nanotips. Electrochemical etching can be used to produce sharp metal tips. In the following, we discuss the fabrication of tungsten and gold nanotips, the major "workhorses" of our experiment (subsection 3.3.1). A fundamental effect at metal nanotips is field emission of electrons in strong static electric fields, introduced in subsection 3.3.2. The understanding of (DC) field emission is crucial for the experiment. Metal tips also have the advantage that they can be easily characterized with many different methods (subsection 3.3.3). The possibility of surface structure imaging and manipulation on an atomic level make these emitters intriguing electron sources.

3.3.1 Nanotip fabrication

The fabrication of nanotips with electrochemical etching is fairly straightforward and robust. Because tips are used in scanning electron microscopy there is a vast amount of literature on fabrication techniques.

We use tungsten and gold nanotips in our experiment. The fabrication method for both materials is based on the so-called two-lamellae drop-off technique (see, e.g., [125]). A thin wire of the desired tip material is mounted vertically, parallel to the gravity force (see Fig. 3.4). The wire points through two metal rings that are separated at least by 4 mm and have a diameter of about 7 mm. Both rings are briefly immersed in an etchant solution, resulting in the formation of a thin film in the rings. A lamella forms around the wire. The application of a small DC voltage between wire and upper ring induces electrochemical etching at the point where the film touches the wire. Because the transport of molecular ions from the etchant solution is more effective to the central part of the lamella (see inset of Fig. 3.4), etching is also stronger there than on the fringes of the lamella. The etching procedure considerably thins the wire until it finally breaks under the influence of gravity. A detection mechanism using the lower ring detects this event and a fast electronic cut-off is triggered so that etching is discontinued at the remaining upper part of the wire. In this way, further blunting of the wire is avoided. The resulting wire ends in a sharp tip. The size of the tip apex can be as small as several nanometers.

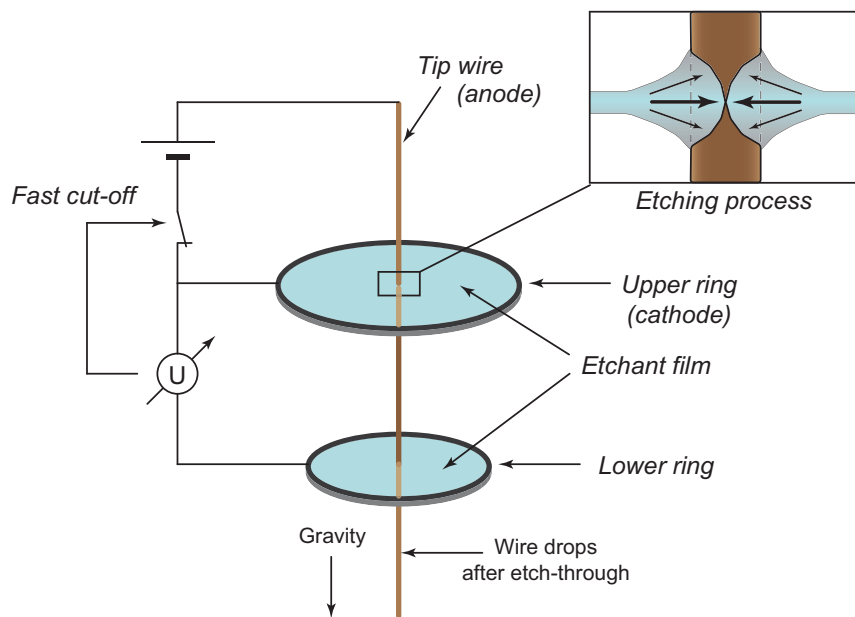


Figure 3.4: Illustration of the double-lamellae drop-off technique. A thin wire is mounted vertically along gravity. Two rings hold a film with etchant solution. Applying a voltage between wire and upper ring causes electrochemical etching at the place where the wire touches the etchant solution. Due to the formation of a lamella around the wire (inset), slowly two tip-like structures are etched into the wire. When the wire finally breaks under the influence of gravity and etching, a fast electronic cut-off switches off the etching voltage. The remaining upper tip can be used for the experiment.

Tungsten tips

Tungsten (chemical symbol W) has the highest melting point (3,683 K) among all pure metals and can therefore withstand high temperatures. It also has a comparatively large

thermal conductivity. A drawback of tungsten is that it oxidates quickly. The oxide layers on the apex, however, can be removed easily with the methods described below.

The fabrication procedure for a tip made from tungsten wire follows the outline given in the previous paragraph. Usually a polycrystalline tungsten wire with a diameter of 0.1 mm is used for etching. Due to the wire production process, the grains in the wire are oriented along the crystallographic (110) direction. W(110) orientation means that the spatial (110) direction in the lattice, here expressed with Miller indices, is parallel to the axis of the wire. Other crystallographic orientations require single-crystal tungsten wire for etching. Throughout this thesis single-crystal tungsten wire in (310) orientation with a diameter of 0.127 mm is used. W(310) has the lowest work function of all possible orientations of tungsten [92].

For tungsten, an aqueous sodium hydroxide (NaOH) solution with a concentration of 3M is used for etching⁷. The two rings are made from gold wire, which is not affected by the etchant solution. The etching voltage is 6 V. Ideally, currents ranging from 1...5 mA are detected during etching. Etch-through usually occurs within 2 min after switching on the etching voltage. After etch-through, distilled water is used to rinse the tip.

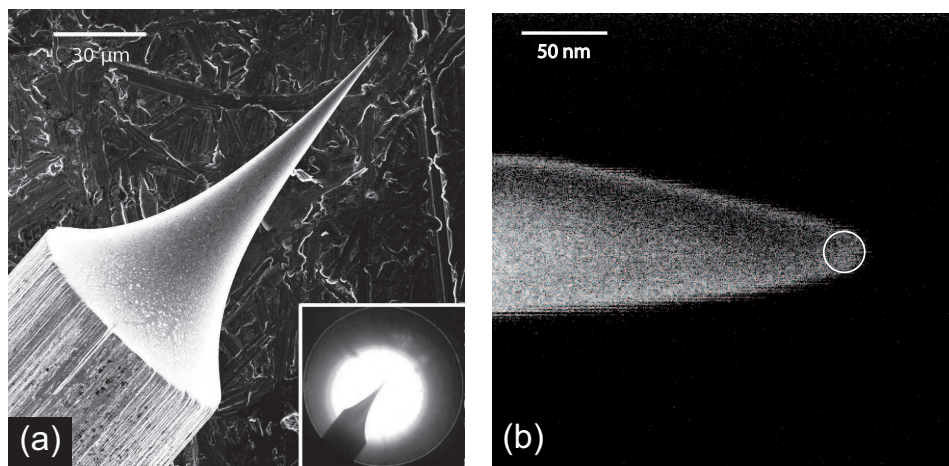


Figure 3.5: Images of tungsten tips produced with NaOH solution. (a) Low-resolution scanning electron microscope image. Inset: Optical microscope image. (b) High-resolution scanning electron microscope image. The circle has a radius of about 12 nm.

The resulting tungsten tips can be inspected with an optical microscope (see Fig. 3.5(a)). Usually, a shiny surface and a smooth shape of the tip shank are a good sign that the tip is sharp and usable for the experiment. Better insight can be gained from scanning electron microscope (SEM) images. Fig. 3.5(b) shows a close-up image of the apex region of a tungsten tip. The shape of the tip apex can be approximated with a hemisphere, here with a radius of curvature of about 12 nm. Tungsten tips produced with NaOH have radii ranging from 5 nm to 50 nm. The full opening angle of the tips is typically about 10°. Unfortunately, SEM imaging of tips cause deposition of carbon material on the tip surface, rendering the tip unusable without further cleaning procedures. An optical inspection of a tip is sufficient because the success rate of the etching procedure is high (~90%). We clean the tip in the vacuum chamber and use field emission to test it.

⁷4.8 g of solid NaOH in 40 ml of deionized H₂O.

Gold tips

Gold is a favorable tip material due to its high thermal conductivity [67] and its plasmonic nature. The latter is the reason why scanning near-field optical microscopy is often performed with gold tips. There are several methods for the fabrication of gold tips (see, e.g., the references in [126]). We developed a novel fabrication procedure [127] that reliably produces tips with high surface quality using a nonhazardous etchant solution.

The method is based on a 90% saturated aqueous potassium chloride (KCl) etchant solution⁸. A polycrystalline gold wire with a diameter of 0.1 mm is used for tip fabrication. The rings for gold etching are made of platinum wire. A DC voltage of 10 V drives the etching process. Currents as high as 40 mA are detected during etching. Etching is characterized by strong bubble formation, causing frequent ruptures of the upper lamella. Therefore the rings have to be refilled with the etchant solution several times. After etch-through the remaining tip is carefully rinsed with acetone.

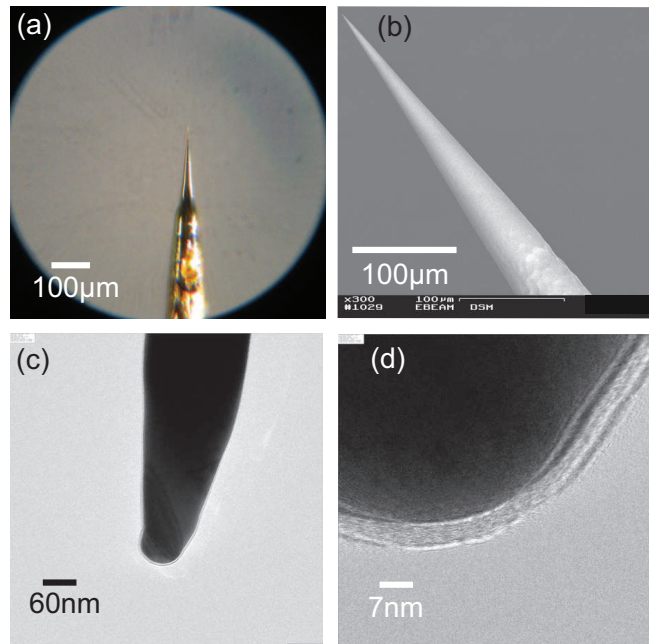


Figure 3.6: Images of gold tips produced with KCl solution. (a) Optical microscope image. (b) Low-resolution scanning electron microscopy image. (c) Transmission electron microscope image. The transparent film seen on the surface arises from passivation layers. (d) High-resolution transmission electron microscope image of the tip apex. Taken from [127].

Fig. 3.6 shows results of the KCl-based etching process. A shiny gold surface under the optical microscope (Fig. 3.6(a)) hints already towards the high surface quality that can also be seen in an SEM image (Fig. 3.6(b)). The full opening angle of the tip shank is about 10° . Transmission electron microscope images reveal that a thin passivation layer remains from the etching process (Fig. 3.6(d)). The surface roughness inferred from the TEM images is below 0.8 nm. Tip radii between 20 nm and 50 nm have been achieved with the KCl method.

⁸29.7 g of solid potassium chloride in 100 ml of deionized H₂O.

Tip cleaning by resistive heating and field evaporation

After installing a tip into the vacuum chamber, it can be cleaned *in situ* with the help of two methods, namely resistive heating and field evaporation. Careful heating of a tungsten tip at a temperature of about 1,000 K results in the evaporation of surface oxide layers [128]. Higher temperatures can lead to blunting of the tip and faceting of the apex. Resistive heating to about 1,000 K is achieved by sending a high current of 3–3.5 A through the support wire that holds the tip. Observation of slight glowing of the tip with an infrared viewer indicates that the right temperature is reached. However, this method cannot be applied to gold tips that experience considerable blunting already at much lower temperatures.

Field evaporation [129, 130] is based on the evaporation of protruding surface atoms in high static electric fields. For tungsten, a field of about $+57 \text{ GV m}^{-1}$ is required to induce field evaporation [131]. Gold tips experience this effect already at a lower field strength of $\sim 35 \text{ GV m}^{-1}$ [130]. Field evaporation of tungsten tips can be directly observed and controlled with field ion microscopy (see below). This enables surface structure manipulation on an atomic level. The disadvantage of the method is that only the tip apex is cleaned. Adsorbates remaining at the tip shank can diffuse to the apex after cleaning by field evaporation.

3.3.2 Field emission

Field emission is the static analogue to light-induced tunneling photoemission (see subsection 2.1.2). A strong static electric field creates a penetrable tunneling barrier. Electrons tunnel from occupied states around the Fermi level into the vacuum (see Fig. 3.7). Field emission is a phenomenon well known for more than a century and was successfully described with quantum mechanics by Fowler and Nordheim already in 1928 [52] as one of the first applications of the Wentzel-Kramers-Brillouin approximation. The so-called Fowler-Nordheim (FN) equation (see, e.g., [132, 133]) relates the emission current density j to the electric field strength E_{DC} . It is of the form

$$j(E_{\text{DC}}) \propto \frac{1}{t^2(y)} E_{\text{DC}}^2 \exp \left\{ -\frac{4\sqrt{2m}}{3|e|\hbar} v(y) \frac{\phi^{3/2}}{|E_{\text{DC}}|} \right\}. \quad (3.2)$$

Here y denotes the Nordheim parameter that is given by

$$y = \sqrt{\frac{|e|^3 |E_{\text{DC}}|}{4\pi\epsilon_0 \phi^2}}. \quad (3.3)$$

The scaling of the current density with the field is highly nonlinear. The FN equation bears much similarity to the Keldysh tunneling photoemission rate (Eq. 2.8). Its derivation also involves semiclassical approximations, just as in the Keldysh theory. The dimensionless Nordheim functions $v(y)$ and $t(y)$ account for effects arising from the image-force potential (Eq. 2.54) acting on the electrons. Approximate closed-form expressions exist for these function [134]. For usual parameters in the experiment ($E_{\text{DC}} \sim -2 \text{ GV m}^{-1}$, $\phi = 4.5 \text{ eV}$), $v(y) \approx 0.8$ and $t(y) \approx 1$ hold true. Observable field emission currents on

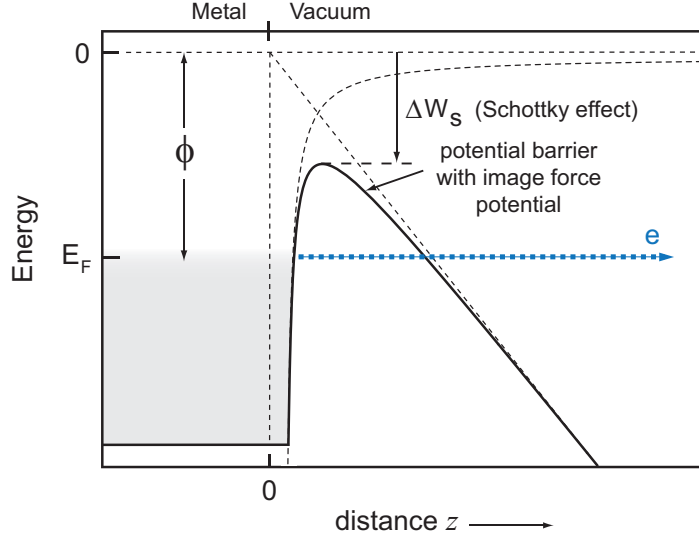


Figure 3.7: Illustration of field emission. Field emission takes place at a metal-vacuum interface if a high static electric field is applied to the metal surface. Electrons tunnel from the Fermi level at E_F and lower lying states into the vacuum. Due to the image-force potential acting on emitted electrons, the potential barrier is lowered by ΔW_s with respect to the vacuum level (Schottky effect).

the order of fA are produced at nanotips at field strengths of about -2 GV m^{-1} or larger absolute field strengths [135, 136].

The image-force potential (Eq. 2.54) in conjunction with the static electric field causes a lowering of the height of the tunneling barrier by

$$\Delta W_s = \sqrt{\frac{|e|^3 |E_{DC}|}{4\pi\epsilon_0}}, \quad (3.4)$$

also known as Schottky effect [137].

We use the field emission process in our experiment to extract the tip size and record images of the emission pattern with field emission microscopy (see below).

3.3.3 In-situ tip characterization methods

A particularly intriguing property of sharp metal tips is the possibility to apply *in-situ* tip characterization methods. The tip mounted in the vacuum chamber can be characterized with a wide variety of methods without the need to open the chamber. Of utmost importance is the knowledge of the radius of curvature r of the tip apex. This quantity defines the sharpness of the tip. The sharper the tip, the larger is the static field strength at the surface of the tip apex for a given bias voltage. The relation between tip bias voltage U_{tip} and static field strength E_{DC} is given by [129, 130]

$$E_{DC} = \frac{U_{\text{tip}}}{kr}. \quad (3.5)$$

k is called field reduction factor: due to the presence of the tip shank, the field strength attained at a tip is smaller than for the ideal case of a metallic sphere. For the tips in

the experiment, k is about 5–15 and depends on the shape of the tip's apex and shank, and on the anode-tip distance. With a radius of 5 nm and a field reduction factor of 15, a voltage of 300 V translates into an enormous field strength of 4 GV m^{-1} at the tip apex. The parameter kr is the defining quantity for voltage-to-field conversion. kr and r can be determined with a wide variety of methods. We will discuss their advantages and disadvantages below.

In addition to the radius of curvature, it is profitable to gain knowledge about the surface structure and the emission pattern. Two microscopy methods that enable this are described below, namely field emission microscopy and field ion microscopy.

Fowler-Nordheim plot

This simple method based on field emission enables the determination of the voltage-to-field conversion parameter kr . Field emission is described by the Fowler-Nordheim equation (Eq. 3.2) that is a function of the field strength E_{DC} . Displaying the total field emission current J as a function of tip voltage U_{tip} in an $\ln(J^2/U_{\text{tip}})$ vs. $1/U_{\text{tip}}$ plot yields the so-called Fowler-Nordheim (FN) plot. The FN plot can be fitted with a straight line of slope s . From the slope, the parameter kr can be inferred from the formula

$$kr = -\frac{3|e|\hbar}{4\sqrt{2m}\phi^{3/2}} \cdot \frac{s}{v(y)}. \quad (3.6)$$

A drawback of this method is that the Nordheim function $v(y)$ influences the determination of kr . The value of $v(y)$ can be deduced with the help of an iterative scheme [36, 129]: We start with the assumption $v(y) = 1$ and calculate a preliminary factor kr with Eq. 3.6. We then determine E_{DC} from the voltage U_{tip} used to record the FN plot, and finally calculate the Nordheim parameter y and $v(y) \approx 1 - y^2 + (1/3)y^2 \ln y$ [134]. This procedure is repeated until convergence. Another drawback here is the dependence of the field reduction factor k on the tip-anode distance and geometry.

Fig. 3.8 depicts a typical FN plot. The plot was recorded with the spectrometer's MCP detector and gives a valid voltage-to-field conversion parameter kr for measurements with the spectrometer placed in front of the tip. Here the kr parameter is $(165 \pm 5) \text{ nm}$, with $v(y) = 0.79 \pm 0.04$, inferred from the slope of the linear fit curve $s = (-8569 \pm 106) \text{ V}$. The ring counting method (see below) yields a tip radius $r = (13.4 \pm 1.7) \text{ nm}$, from which we infer $k \sim 12$.

Field emission microscopy

Field emission microscopy (FEM, [19, 129]) is a powerful and simple method to investigate the emission pattern of a tip. In FEM, a nanotip faces a spatially resolving detector, in our case an MCP detector. A high negative voltage drives field emission from the tip. The static electric field determines the trajectories of electrons emitted from the tip apex. Because the field is strongest near the surface, electrons gain the highest fraction of their final velocity within a few tip radii distance from their emission site. Therefore they leave the tip nearly radially and are subsequently drawn towards the screen, where a projection image of their respective emission sites at the hemispherical tip surface is formed. Effectively, the system represents a projection microscope. Its magnification

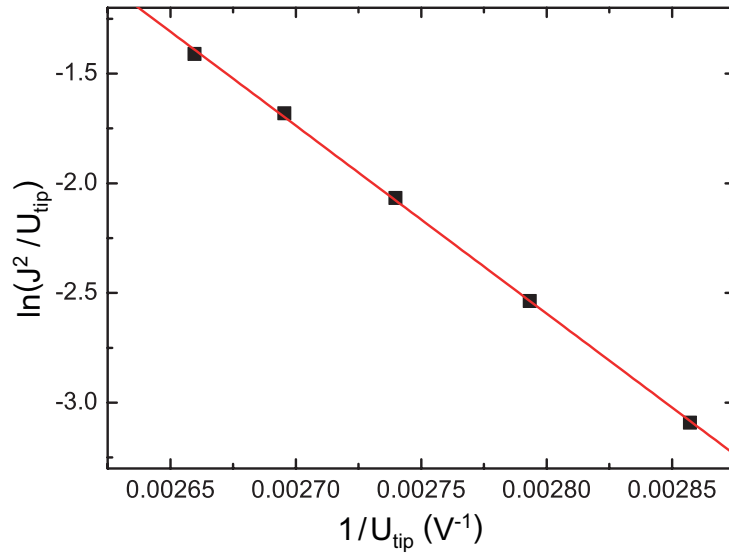


Figure 3.8: Fowler-Nordheim plot. Plotting the field emission current J as a function of tip voltage U_{tip} approximately yields a straight line. From its slope, the voltage-to-field conversion parameter kr can be inferred. Here it is (165 ± 5) nm.

factor is given by the ratio of tip-anode distance and tip radius and is on the order of 10^6 . The emission sites on the tip apex can be imaged with a resolution of several nanometers in FEM.

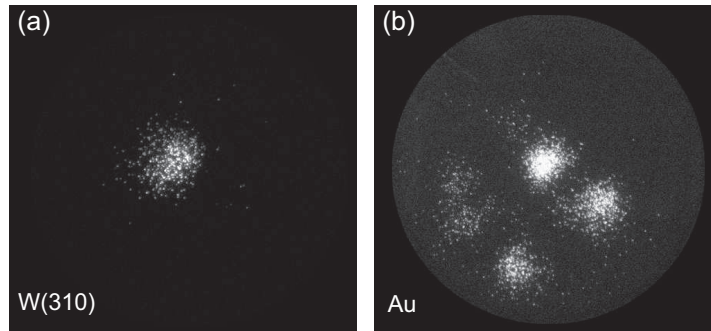


Figure 3.9: Field emission microscope images of nanotips. (a) Image of a tungsten tip in (310) orientation. A single emission spot is visible that originates from (310) poles. (b) Image of a polycrystalline gold tip. Four larger spots are observed.

Fig. 3.9 shows typical field emission patterns recorded with FEM from a tungsten tip in W(310) orientation and a polycrystalline gold tip. The tungsten image shows a single emission spot that corresponds to emission from four W(310) facets on the tip surface. W(310) facets exhibit the lowest local work function. The remaining tip surface does not contribute to field emission. The image of the gold tip features four larger emission spots that are characterized by a four-fold symmetry. The interpretation of these images is not straightforward and a more powerful method exists, namely field ion microscopy (see below).

Field ion microscopy

Field ion microscopy (FIM) was the first method to make single atoms on a surface visible to the human eye in 1955 [21, 130]. FIM is also a projection microscopy technique very similar to FEM, but uses ions for imaging instead of electrons. To this end, the vacuum chamber is backfilled with an imaging gas. The tip is biased with a high positive voltage with respect to the detector. Atoms from the imaging gas are polarized and attracted in the high field at the tip apex. When a gas atom gets so close to atoms on the surface it is ionized in the local field close to an atomic site. The remaining ion is positively charged and repelled by the positively biased tip. The ions are accelerated towards the MCP and form a projection microscope image. The magnification factor is similar to that of FEM. In contrast to FEM, the resolution provided by FIM is usually much higher and suffices to image single protruding atoms on the tip surface.

Tungsten and gold tips require different imaging gases. For tungsten, helium at a partial pressure of 5×10^{-6} mbar leads to good results and atomic resolution at room temperature. Fig. 3.10(a) displays a typical FIM image of a W(310) tip. The tip radius is estimated to be $r \approx 12$ nm from the ring-counting method (see below). The FIM image has been recorded with a bias voltage of +7.1 kV and a low MCP gain voltage of about +1.2 kV. In FIM images of tungsten, single atomic sites can be resolved. The layer structure of the atomic lattice is clearly visible in the picture, in particular in ring structures.

A ball model (see Fig. 3.10(c)) helps to identify crystallographic poles. In the model, a hemisphere is cut into the bcc lattice structure of tungsten in order to model the surface of the tip apex. The distance of each lattice site to the hemisphere surface is calculated and displayed in a color code. Protrusions (red) experience higher local electric fields than depressions (green) and appear as bright spots in the experimental image. As expected, the W(310) pole is pointing in forward direction. This helps with the interpretation of FEM images. Often only a single emission spot is visible (see Fig. 3.9(a)). For sharp tips with radii smaller than about 40 nm, the emission spot originates from four (310) facets centered around the (100) pole. Electron emission from these spots merges for sufficiently small tip radii. W(310) has the lowest work function of all tungsten orientations.

For gold tips, neon was used for imaging. The use of helium is not possible because rapid field evaporation sets in already before a FIM image can be formed. Neon has a lower ionization potential than helium and images can be obtained at fields below the field evaporation threshold. Fig. 3.10(b) displays an FIM image of a polycrystalline gold tip with a radius of about 65 nm estimated from an FN plot. At room temperature, FIM of gold does not provide high-contrast atomic resolution. Some atomic sites are visible in the image, but a full characterization of the surface is elusive. A four-fold symmetry can be seen in the FIM image and also in the FEM image (3.9(b)). The ball model using an fcc lattice shows that the gold tip is oriented in the (100) direction (Fig. 3.10(d)).

The voltage-to-field conversion parameter kr can be estimated by determining the voltage U_{BI} where the FIM image has the highest contrast and quality. The field strength E_{BI} where the highest imaging quality is reached is called best-image field and is well known [131]. The best image field of helium is about 47 GV m^{-1} for tips with a radius of about 10 nm. kr can be calculated from U_{BI} and E_{BI} via Eq. 3.5. Performing this analysis with the tungsten tip in Fig. 3.10(a) yields $kr \approx 66$ nm. The drawback of this

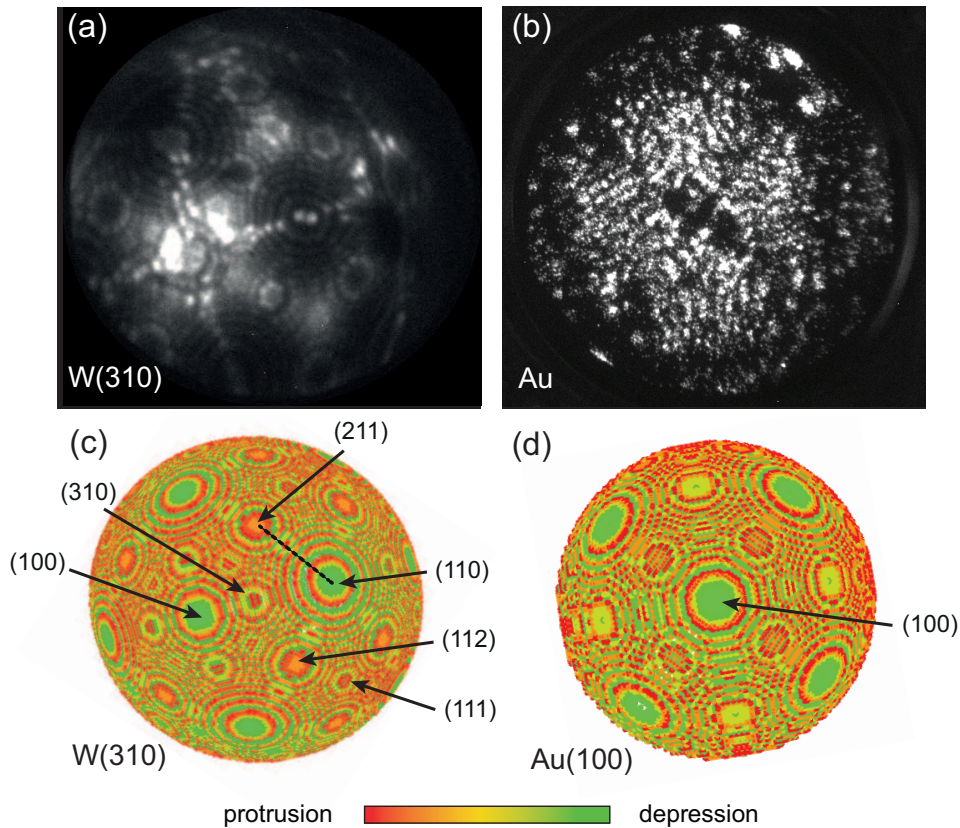


Figure 3.10: Room-temperature field ion microscope images of nanotips. (a) Image of a tungsten tip in (310) orientation using helium gas. The tip radius inferred from the ring-counting method is about 12 nm. (b) Image of a polycrystalline gold tip using krypton gas. The four-fold symmetry of the FEM image is clearly visible. High-contrast atomic resolution, however, is elusive at room temperature. (c) Ball model of a W(310) tip. The model enables identification of crystalline poles on the apex surface. Red color indicates protruding atomic structures that experience high local fields. These structures appear very bright in the experimental image. The ring counting method is applied between the (110) and (211) poles (dotted line). (d) Ball model of Au tip in (100) orientation.

method is that the best image voltage is a very subjective criterion and prone to human error. Furthermore, this method can only be used with the MCP detector. kr in the spectrometer geometry can only be determined using an FN plot recorded with the spectrometer itself.

Ring counting method

The most powerful and reliable method to determine the tip radius r is the ring counting method [130]. It relies on the interpretation of field ion microscope images in the light of the well-known crystal lattice structure of metals. It can be applied only to tungsten since gold does not provide the necessary image quality in our setup. The description of the method here is based on [37]. Atoms terminating atomic layers of the tungsten bcc lattice structure protrude from the rest of the surface (see ball model in Fig. 3.10(c)) and are visible as bright spots in FIM images. Most strikingly, around the (110) poles,

pronounced ring structures are found that originate from the cut of a hemisphere into the lattice.

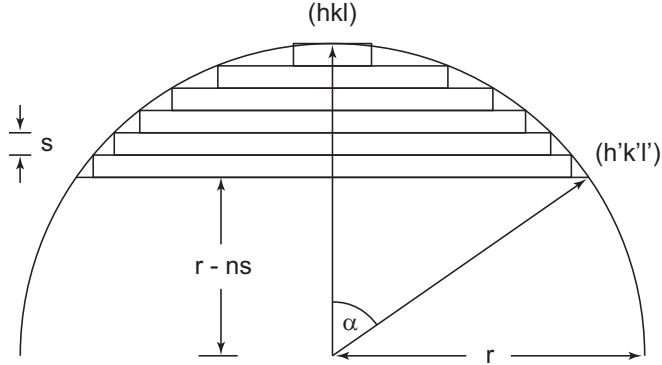


Figure 3.11: Illustration of the ring counting method. The radius r of the hemisphere can be determined with the help of the crystal lattice structure (see text).

Fig. 3.11 illustrates the method: Counting the number of rings n between two crystallographic poles gives the radius of curvature via the relation

$$r = \frac{ns}{1 - \cos \alpha}. \quad (3.7)$$

$s = a/(\delta\sqrt{h^2 + k^2 + l^2})$ is the lattice step size for the reference orientation (h, k, l) (here (110)). a denotes the lattice constant (tungsten: $a = 3.16 \text{ \AA}$) and δ is 1 if $h + k + l$ is an even number and 2 otherwise. α is the angle between reference orientation (h, k, l) and secondary orientation (h', k', l') (here (211)). It is given by

$$\cos \alpha = (hh' + kk' + ll')/\sqrt{(h^2 + k^2 + l^2)(h'^2 + k'^2 + l'^2)}. \quad (3.8)$$

For $(h, k, l) = (110)$ and $(h', k', l') = (211)$, we find $\alpha = 30^\circ$. For the FIM image in Fig. 3.10, one finds $r = (8.5 \pm 1.7) \text{ nm}$. The disadvantage of the method is that only the local curvature between the two poles is measured. The results from the ring counting method are not accurate if the apex seriously deviates from the ideal case of a hemisphere.

4 Strong-field above-threshold photoemission from nanotips

In this chapter, we will present experimental measurements of above-threshold photoemission from tips triggered by few-cycle laser pulses. Photoelectron spectra play an important role in this investigation of light-matter interaction since they reveal much of the photoemission physics at nanotips.

4.1 Above-threshold photoemission

In the following, we apply FEM (subsection 3.3.3) to investigate the emission pattern of photoemission and spectral measurements to get insight about the underlying photoemission mechanism.

Emission pattern

Fig. 4.1 depicts emission patterns of DC field emission and photoemission recorded with the MCP detector using a W(310) tip. A tip radius of curvature of about (10 ± 2) nm was inferred from a FIM micrograph (see Fig. 4.1(c)) with the ring counting method.

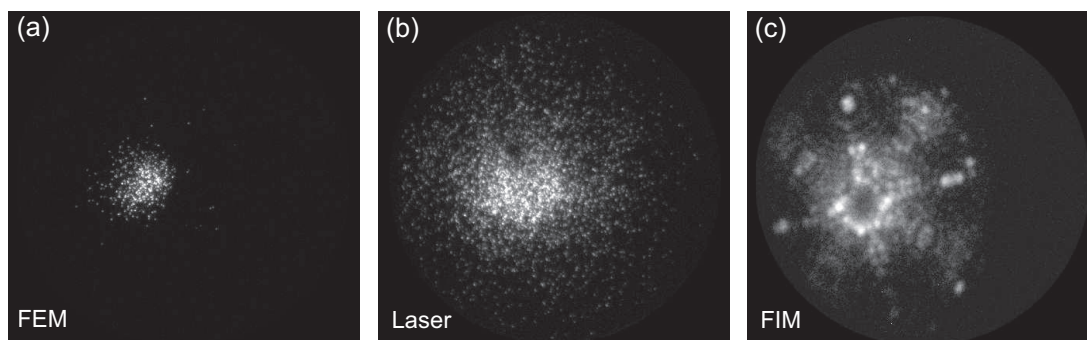


Figure 4.1: Emission pattern of laser-induced electron emission from a W(310) tip. (a) FEM image of DC field emission (static field strength $E_{\text{DC}} \approx -2.7 \text{ GV m}^{-1}$). (b) FEM image of laser-induced electron emission (laser intensity $I_0 = 4 \times 10^{10} \text{ W cm}^{-2}$, $E_{\text{DC}} \approx -1.3 \text{ GV m}^{-1}$). (c). FIM micrograph of the tip ($U_{\text{tip}} = +7.5 \text{ kV}$). The emission spots of field emission and photoemission can be identified with four low work function (310) facets centered around the crystallographic (100) pole.

The tip's voltage-to-field conversion parameter in the MCP detector geometry is estimated to be $kr = (160 \pm 30) \text{ nm}$ from the best image field in FIM. Field emission (Fig. 4.1(a)) was driven with a static field of $E_{\text{DC}} \approx -2.7 \text{ GV m}^{-1}$ (bias voltage

$U_{\text{tip}} = -409 \text{ V}$). Photoemission (Fig. 4.1(b)) was triggered by 6-fs pulses at 800 nm wavelength from the Ti:sapphire laser oscillator with an intensity of $I_0 = 4 \times 10^{10} \text{ W cm}^{-2}$ at a static field of $E_{\text{DC}} \approx -1.3 \text{ GV m}^{-1}$ (bias voltage $U_{\text{tip}} = -190 \text{ V}$).

A comparison of FEM and FIM images reveals that the single spot visible in both field emission and photoemission originates from four (310) facets centered around the (100) pole. At these facets the local work function is lowest so that electrons are preferably emitted from there in field emission and photoemission. The photoemission spot is considerably larger than the spot from field emission. Furthermore, faint signatures of photoelectrons are found from all over the apex area. This suggests that photoemission is not as sensitive to the local work function as field emission. The majority of photoelectrons is emitted in forward direction in a single emission cone with an opening angle of $\sim 20^\circ$ (FWHM). The fact that the photoemission pattern is well defined shows that the choice of a W(310) is advantageous for this experiment. In the following, we focus on spectrally resolved photoemission measurements. Their discussion is based on [35, 32].

Photoelectron spectra

Fig. 4.2(a) shows electron spectra obtained at light intensities¹ of $1.9 \dots 4.6 \times 10^{11} \text{ W cm}^{-2}$ using the same W(310) tip as above. A positive extraction voltage of 150 V is applied to the entrance aperture of the spectrometer. The bias voltage translates into a static electric field of -1.2 GV m^{-1} at the tip apex². The parameters were adjusted so that less than one electron per pulse was emitted from the tip in order to avoid Coulomb repulsion effects.

In the photoelectron spectra, peaks are clearly visible on top of an overall exponential decay. Absorption of three photons of energy $\hbar\omega \approx 1.55 \text{ eV}$ is necessary for multiphoton photoemission to overcome the surface potential barrier with effective height $\phi_{\text{eff}} \approx 4 \text{ eV}$. In the five curves with lowest intensity in Fig. 4.2, we observe the lowest-order peak at around 4.3 eV. There are further peaks visible with energies that correspond to the absorption of more than three photons, representing above-threshold peaks. In the curve with highest intensity ($4.6 \times 10^{11} \text{ W cm}^{-2}$), we observe photon peaks up to the order $n = 9$. The ATP peak structure is clearly visible in our experiment. This is because the tip apex is much smaller than the laser spot size so that focal averaging effects are avoided. The visibility of spectral features will play a decisive role in the forthcoming parts of this experimental investigation.

We find that the peaks are approximately spaced by $\sim 1.47 \text{ eV}$ as determined by a linear fit of their positions at $2.3 \times 10^{11} \text{ W cm}^{-2}$ (Fig. 4.2(b)). The positions were inferred from multiple Gaussian peak fits (see Fig. 4.3). The three-photon peak position is located slightly above the fit curve, which includes the higher photon orders only. If we extrapolate the linear fit to zero photon order we see that it intersects the energy axis at about -0.5 eV below the Fermi level. At W(310) surfaces, a pronounced peak is found in the local density of states at an energy of -0.4 eV below the Fermi level [138]. We conclude that the majority of electrons originate from there and in general from the vicinity of the Fermi level.

¹In the original publication [32], the intensity values are a factor of 2 too small, here they are correct.

²This value differs considerably from -0.8 GV m^{-1} given in [32] and was derived from a re-analysis of the data.

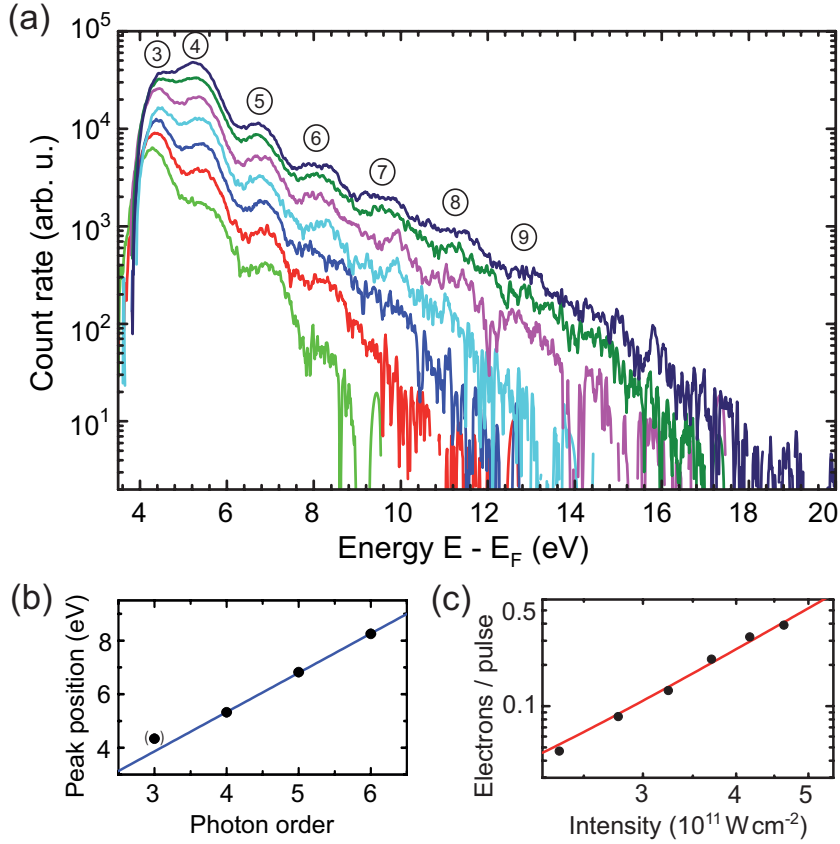


Figure 4.2: Above-threshold photoemission electron spectra as a function of laser intensity. (a) Count rate on logarithmic scale as a function of energy for different laser intensities. From bottom to top, the peak intensity is $I_0 = \{1.9, 2.3, 2.8, 3.2, 3.7, 4.2, 4.6\} \times 10^{11} \text{ W cm}^{-2}$. The applied extraction voltage is 150 V, corresponding to a static electric field of -1.2 GV m^{-1} . The energy is referenced to the Fermi energy E_F . The encircled numbers indicate the multiphoton order. (b) Positions of the spectral peaks for $2.3 \times 10^{11} \text{ W cm}^{-2}$ as a function of photon order. The data is consistent with ATP with 1.47 eV photons (solid line: linear fit excluding the lowest order). (c) Total tip current as a function of intensity in a double-logarithmic plot. The line represents a multiphoton power-law fit to the data with $n \approx 3.1$ (see text). Taken from [35, 32].

The spectral cut-on at an energy of about 4 eV above the Fermi energy E_F marks the effective barrier height ϕ_{eff} . With a work function of $\phi = 4.35 \text{ eV}$ and a static electric field of $E_{\text{DC}} = -1.2 \text{ GV m}^{-1}$, an effective barrier height of $\phi_{\text{eff}} = 3.0 \text{ eV}$ is expected due to the Schottky effect (cf. Eq. 3.4). In the experiment, however, we find a significantly higher value of $\phi_{\text{eff}} \sim 4 \text{ eV}$. We regularly observe in the experiment that ϕ_{eff} grows larger within about one hour after cleaning by field evaporation and then stabilizes to a constant value. Other than the shift of the cut-on and a decrease of the total count rate no further changes in the photoelectron spectra have been detected. The change in ϕ_{eff} is likely due to adsorption of residual gas atoms [139].

The scaling of the total photocurrent with intensity follows the multiphoton power law (Eq. 2.2) with $n = 3.1 \pm 0.1$ (see Fig. 4.2(c)) and confirms that three-photon absorption dominates the photoemission process. Without spectral information, the detection

of above-threshold processes would be practically impossible. No deviation from the multiphoton power-law is observed even at high intensity.

4.2 Strong-field effects: Peak suppression and peak shifting

A closer look at the spectra shown in Fig. 4.2 reveals more subtle effects. Fig. 4.3(a) depicts a close-up version of the same data in linear scale. Beginning with an intensity of $4.2 \times 10^{11} \text{ W cm}^{-2}$ the yield of the $n = 4$ peak exceeds that of the $n = 3$ peak with increasing laser intensity. This is a clear sign that peak suppression and channel closing sets in (subsection 2.1.3). In our case only the lowest photon order is affected by channel closing. At a critical intensity of $\sim 4 \times 10^{11} \text{ W cm}^{-2}$, the three-photon peak is suppressed. The corresponding ponderomotive energy can be estimated as $U_p \approx 0.3 \text{ eV}$.

We also observe the peak shifting effect: The low-order spectral features shift to lower energy with increasing intensity. Fig. 4.3(b) shows the positions of the $n = 4$ and $n = 5$ peaks and of the next lower minima, inferred from multiple Gaussian curve fits to the data. The positions of these spectral features shift approximately linearly with intensity. From Fig. 4.3(b) we deduce a mean slope³ of the spectral shift with intensity of $s_{\text{exp}} = (-5 \pm 3) \text{ eV}/(10^{13} \text{ W cm}^{-2})$. The theoretically expected ponderomotive shift for the intensity I_0 in the bare laser focus has a slope of $s_{\text{th}} = -(dU_p/dI) = -0.55 \text{ eV}/(10^{13} \text{ W cm}^{-2})$. The discrepancy between s_{exp} and s_{th} is due to the near-field enhancement at the tip apex. The field enhancement factor ξ can be extracted from the experimental and the theoretical slope with

$$\xi = \sqrt{\frac{s_{\text{exp}}}{s_{\text{th}}}} = 3.0 \pm 0.8. \quad (4.1)$$

The ponderomotive energy in the enhanced field is $U_p \approx 0.3 \text{ eV}$ for the highest intensity in the measurement. Note that the inferred field enhancement factor is slightly smaller compared to the expected theoretical value of 5 for a 10 nm tip.

A deviation from the simple picture of the ponderomotive shift is evident from Fig. 4.3: The slopes of the shift of the individual spectral features are not uniform, but range from $-1.2 \dots -0.2 \text{ eV}/(10^{12} \text{ W cm}^{-2})$. Moreover, neither minima nor maxima shift perfectly linearly with intensity. For an observation of the spectral shift, the initial states have to experience a much smaller or no light shift than the continuum states during the laser pulse. Close to the Fermi energy, electrons in tungsten are found in s and d bands [140]. s band electrons are considered to be delocalized whereas d band electrons are much more localized to the atomic sites. Following [141], we argue that d band states do not experience a strong light shift because of their localized nature. This creates a similar situation to ATI where the shift of the strongly localized atomic ground state is much smaller than that of the continuum states. The fact that the shift is lower than expected for a tip with a field enhancement factor of 5 can be attributed to a contribution of s band electrons. Another mechanism that could affect the observed shift in our experiment is electron-electron scattering. This effect leads to both to a distortion and to a shift of the spectral features to lower energy [66].

³The value given in [32] is a factor 2 too large due to a miscalculation of the intensity, here it is correct.

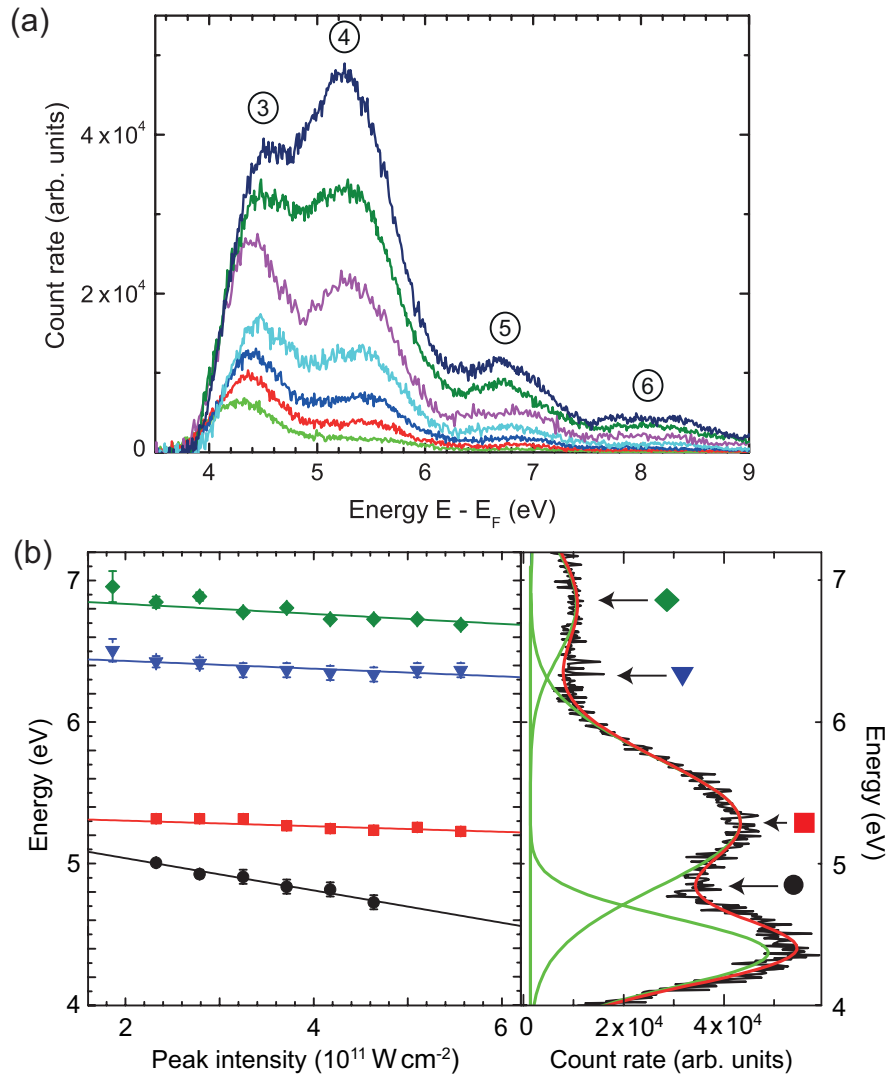


Figure 4.3: Strong-field effects in Above-Threshold Photoemission spectra. (a) Peak suppression. Electron spectra from Fig. 4.2 in linear scale. From bottom to top, the peak intensity is $I_0 = \{1.9, 2.3, 2.8, 3.2, 3.7, 4.2, 4.6\} \times 10^{11} \text{ W cm}^{-2}$. The encircled numbers indicate the multiphoton order. For intensities $I_0 > 4 \times 10^{13} \text{ W cm}^{-2}$, the three-photon peak is suppressed. (b) Peak shifting. The positions of the $n = 4$ and $n = 5$ maxima (squares and diamonds) and that of the next lower minima (balls and triangles) are displayed as function of intensity I_0 . The slopes are in the range of $-1.2 \dots -0.2 \text{ eV}/(10^{12} \text{ W cm}^{-2})$. The positions of the maxima and minima are extracted from fits to the data of Fig. 4.2 with multiple Gaussian curves. Right part: Single spectrum shown in linear scale (black curve). The green curves indicate Gaussian peaks from a multiple peak fit, the red curve displays the sum of all peak contributions.

The results presented in this section underline the fact that the strong-field photoemission regime has been reached. This is an important prerequisite for the main results of this thesis presented in the next chapters. The ponderomotive energy is not negligibly small anymore as inferred from the channel closing and peak shifting effects. The observation of strong-field effects in our spectrally resolved experiment is consistent with

a tip-based photoemission experiment carried out by Bormann *et al.* [61]. The authors deduced the occurrence of channel closings in an indirect way from the intensity scaling of the total photoemission current.

5 Electron rescattering at nanotips

This chapter continues the investigation of Chapter 4 and is devoted to electron recollision and rescattering at metal nanotips. It represents one of the main results of this thesis. The discussion given here follows the original publications [34, 36, 35].

5.1 Electron rescattering in strong light fields and static fields

5.1.1 Rescattering plateau and high-energy cut-off

A series of photoelectron spectra was recorded for gradually increasing laser intensities $I_0 = \{0.55, 0.72, 0.89, 1.1, 1.3\} \times 10^{11} \text{ W cm}^{-2}$ (Fig. 5.1). A fixed extraction voltage of +50 V is applied to the entrance aperture of the spectrometer. With $kr = (125 \pm 40) \text{ nm}$, the field strength is about -0.4 GV m^{-1} . The W(310) tip used here has a radius of about $r \approx 8 \text{ nm}$ inferred from the ring counting method. At maximum intensity, on average only ~ 0.4 electrons per laser pulse are emitted from the tip. Therefore space-charge effects do not play a role in this measurement.

At the lowest laser intensity, ATP peaks are observed on top of an overall exponential decay. The first photon peak at energy $E \approx 5.6 \text{ eV}$ corresponds to multiphoton photoemission with 4 photons. The spectral cut-on is located at an energy of $E \approx 5.2 \text{ eV}$. Taking the Schottky effect into consideration, a work function of 6 eV results, much higher than expected, likely due to adsorbates on the tip surface. For higher intensities a radical change takes place: At energies $E > 9 \text{ eV}$, a pronounced plateau structure builds up with increasing intensity. The count rate stays almost constant between 10 and 15 eV for the highest laser intensity. Beyond the plateau structure we observe a rapid decay of the count rate. The spectrum can be divided into two parts, the low-energy direct part and the high-energy plateau part: The direct part marked by the strong exponential decay contains only direct electrons that do not interact with the surface after photoemission. The plateau part is dominated by electrons that undergo rescattering. In both parts ATP peaks are found. Beyond the plateau part, we find a kink in the spectrum that can be identified with the rescattering cut-off. Rescattering at a metal surface was predicted by Faisal and co-workers in 2005 [80]. This experimental observation represents the first evidence for electron rescattering and recollision at a metal surface.

Intensity scaling of the high-energy cut-off

According to the Three-Step Model introduced in Section 2.2, a rescattered electron can gain a maximum kinetic energy of $E_{\text{cut-off}} \approx 10 U_p$ (cf. Eq. 2.11), hence the cut-off energy

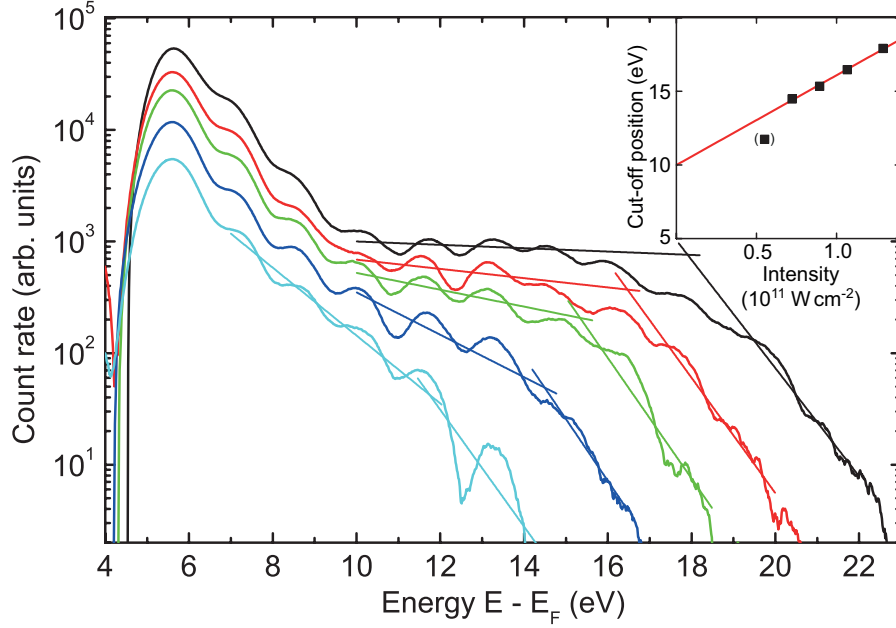


Figure 5.1: Plateau in Above-Threshold Photoemission spectra. Count rate as a function of electron energy for different laser intensities at a fixed static field of -0.4 GV m^{-1} . From bottom to top the curves are recorded at intensities $\{0.55, 0.72, 0.89, 1.1, 1.3\} \times 10^{11} \text{ W cm}^{-2}$. With increasing intensity, a plateau builds up at an energy $E > 9 \text{ eV}$. The lines represent exponential decay fits to the plateau part and to the subsequent decay. The intersection of each pair gives the cut-off energy. Inset: Cut-off energy as a function of intensity. The solid line indicates a linear fit of the four data points with highest intensity.

$E_{\text{cut-off}}$ should scale linearly with intensity. The experimental cut-off position for each intensity was extracted with the help of two separate exponential decay curve fits to the plateau and the subsequent decay part (see Fig. 5.1). The cut-off position as a function of intensity of the incident laser pulses is depicted in the inset of Fig. 5.1. The plot confirms an approximately linear scaling and yields a slope of $s_{\text{exp}} = (6.1 \pm 0.3) \text{ eV}/(10^{11} \text{ W cm}^{-2})$. From the $10 U_p$ law we obtain a slope of $s_{\text{th}} = 10 (dU_p/dI) = 5.5 \text{ eV}/(10^{13} \text{ W cm}^{-2})$ without field enhancement. From the slopes we obtain a field enhancement factor of

$$\xi = \sqrt{\frac{s_{\text{exp}}}{s_{\text{th}}}} = 10.5 \pm 0.3. \quad (5.1)$$

This enhancement factor is unusually high for a tip radius of 8 nm where a field enhancement factor of about 6 is expected (see Section 2.5). We speculate that this discrepancy is caused by an erroneous determination of the intensity in the focal spot or an irregular tip shape causing a higher near-field enhancement. Nevertheless, this investigation shows that the cut-off energy can serve as an indicator for the strength of the optical near-field at the tip apex.

Circular polarization

In ATI with atomic gases, a way to suppress rescattering is to use circularly polarized light [4]. In such a light field, the photoelectrons are propagating on spiral trajectories

and miss the ionic core with a very high probability. This test can also be performed with rescattering at tips. Fig. 5.2 displays electron spectra recorded with linear and circular polarization at a static field strength of about -0.4 GV m^{-1} . The photoelectron spectrum recorded with linear polarization at an intensity of $I_0 = 1.0 \times 10^{12} \text{ W cm}^{-2}$ shows a faint plateau structure and a clear high-energy cut-off. Using the same laser power, but switching to circular polarization results in a drop of the count rate by more than an order of magnitude and in the absence of any clear signature of rescattering. Using twice the laser power, however, changes the picture. The high-energy cut-off is restored, albeit at a lower energy ($\sim 15 \text{ eV}$) than before using linear polarization ($\sim 17 \text{ eV}$). At the same time, also the total count rate is found again at a smaller, but comparable level.

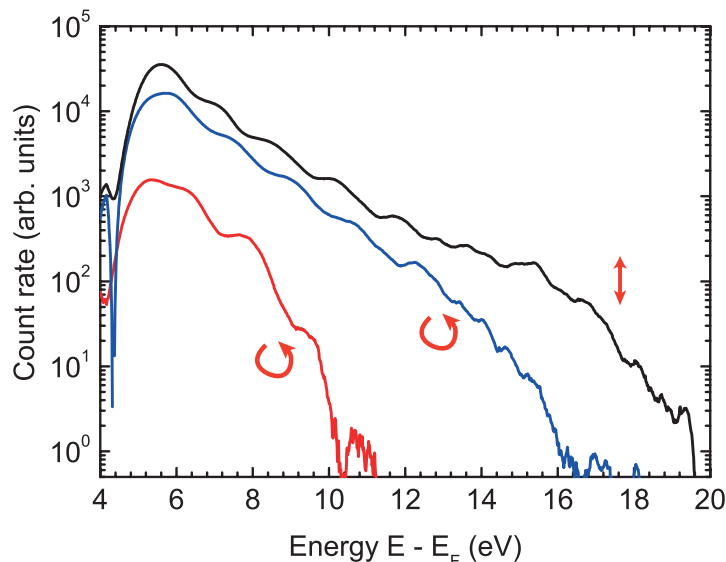


Figure 5.2: Photoemission and rescattering with circularly polarized light. Electron spectra recorded with different polarizations of the laser electric field. The upper spectrum is generated by linearly polarized light with an intensity of $1.0 \times 10^{12} \text{ W cm}^{-2}$. The two spectra below are recorded with circularly polarized light, using the same laser power (lower curve) and twice this power (upper curve).

The observation of rescattering with circularly polarized light most likely arises for two reasons: First, the scattering object is an extended metal surface and not a tiny ionic core like in ATI. Electrons on spiral trajectories are very unlikely to miss the surface. Second, the optical near-field plays a big role: On the axis defined by the tip’s pointing direction, only the electric field component parallel to this axis is strongly enhanced. In our case, the tip acts as a “rectifier” of the light polarization and the electrons are still driven by an approximately linearly polarized near-field. The cycle-averaged intensity corresponding to the field component parallel to the tip’s pointing direction effectively drops by a factor of 2 when switching from linear to circular polarization. As a result, the count rate should drop by a factor of 16 assuming a four-photon multiphoton process, which is consistent with the experimental observation. This drop in count rate can be compensated by using twice the laser power.

5.1.2 Comparison with theory models

The experimental data already provides evidence for electron rescattering. The question addressed in this subsection is now if full-fledged theory models can explain rescattering at a metal surface as observed experimentally. In the following, we will compare the experimental data presented in Fig. 5.1 with three theory models, namely the Quantum Orbit Theory (Section 2.3), the numerical integration of the time-dependent Schrödinger equation (TDSE; subsection 2.4.1) and the time-dependent density functional theory (TDDFT; subsection 2.4.2).

Quantum Orbit Theory

Fig. 5.3 depicts the result of a Quantum Orbit Theory calculation including the modifications for metal surfaces (see subsection 2.3.3). The experimental spectrum recorded at a nominal laser intensity of $I_0 = 1.3 \times 10^{11} \text{ W cm}^{-2}$ (Fig. 5.1) serves as a reference. Both direct and rescattered electrons on long and short trajectories are considered in the calculation. The ultrashort laser pulse is modeled in a very simple way: A sequence of two optical cycles of a cw laser field with 800 nm wavelength drives the system. The electric field $E_L(t)$ is given by

$$E_L(t) = -E_0 \cos(\omega t), 0 \leq t \leq 2T_{\text{opt}}, \quad (5.2)$$

where $T_{\text{opt}} = \lambda/c$ is the optical cycle duration. The electric field strength of $E_0 = 11 \text{ GV m}^{-1}$ (intensity $I = 1.6 \times 10^{13} \text{ W cm}^{-2}$) was chosen so that calculation and reference spectrum agree well. An effective work function of $\phi = 5.2 \text{ eV}$ matches the low-energy cut-on of the reference spectrum. The Keldysh parameter is 1.6, well in the transition regime between multiphoton and tunneling photoemission. The only other fit parameters are the overall photoemission rate and the relative amplitude of direct and rescattered electrons. The interference of direct electrons with rescattered electrons is neglected in the calculation.

Theory and experimental spectrum match fairly well considering the simplicity of the theory model. Shape and peak positions are reproduced by the calculation. Some deviations can be found, however: The peak contrast is much higher in the model than in the experiment because the model considers only a single initial state at the Fermi energy. Another artefact of the theory is the anomalous height of the peak at energy 16.3 eV and a spike at 17.2 eV. Close to the cut-off energy at 17.2 eV, the saddle times for long and short trajectories are very close to each other, causing a breakdown of the saddle-point approximation and hence of the Quantum Orbit Theory.

The individual contributions can be directly separated in the model: Direct electron trajectories form the direct part with its characteristic exponential decay. The calculation also confirms that the plateau indeed arises from electron rescattering. The timing of the emission of direct and rescattered electrons follows the behavior already found in Fig. 2.12. There is a dip at $\sim 8 \text{ eV}$ in the overall count rate contributed by rescattered electrons, caused by the interference of long and short trajectories. The model shows that rescattering found in the experimental data can be reasonably explained with the Quantum Orbit Theory.

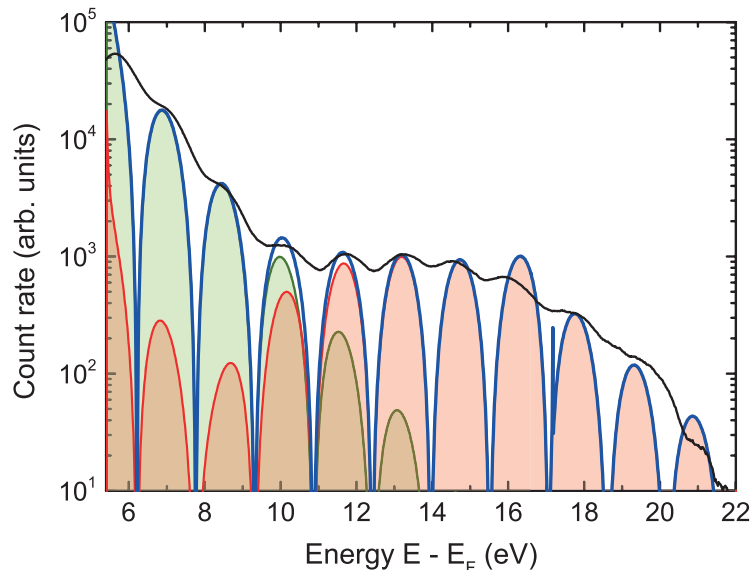


Figure 5.3: Quantum Orbit Theory calculation of rescattering at a metal surface.

An experimental spectrum ($I_0 = 1.3 \times 10^{11} \text{ W cm}^{-2}$ from Fig. 5.1, black curve) is compared to a Quantum Orbit Theory calculation (blue curve). The individual contributions from direct electrons (green curve) and rescattered electrons (red curve) are also shown. The calculation parameters are the following: Field amplitude $E_0 = 11 \text{ GV m}^{-1}$, wavelength $\lambda = 800 \text{ nm}$ and effective work function $\phi = 5.2 \text{ eV}$. A sequence of two optical cycles of a cw field is used to mimick the ultrashort laser pulse.

Integration of the time-dependent Schrödinger equation

In the following, we will compare the experimental spectrum to the numerical integration of the TDSE, introduced in subsection 2.4.1. In contrast to the Quantum Orbit Theory model above, it incorporates the static electric field and the image-force potential.

Fig. 5.4 shows the result of a calculation with the TDSE model. A Gaussian laser pulse with a duration of $\tau = 5.5 \text{ fs}$ (intensity FWHM) is used in the calculation. Spectra were averaged over 8 different carrier-envelope phases in order to retrieve a phase-averaged spectrum. The calculation includes a static electric field of $E_{\text{DC}} = -0.4 \text{ GV m}^{-1}$. The work function is chosen as $\phi = 6 \text{ eV}$ so that the effective barrier height including the Schottky effect is 5.2 eV . The Fermi energy with respect to the bottom of the metal-like potential well is 9 eV . The laser electric peak field is $E_0 = 11 \text{ GV m}^{-1}$, the same value as in the previous calculation with the Quantum Orbit Theory. In the numerical integration procedure, the step size of the spatial grid is 0.04 \AA and the time step is 4.3 as .

The agreement of theory and experiment is reasonably good in the plateau part. Also a comparison to the Quantum Orbit Theory gives good results there. The direct part, however, matches only poorly with the experimental reference spectrum. This is due to the fact that the potential used in the calculation strongly enhances rescattering: Scattering takes place predominantly at the infinitely high potential barrier at the lower end of the spatial grid and not at the potential step at the metal-vacuum interface (cf. Fig. 2.17). The direct part quickly disappears in the rescattered part. Strong interference between both parts manifests itself in the irregular peak structure at low energies. The shape of the rescattered part, however, does not suffer from the shortcomings of our

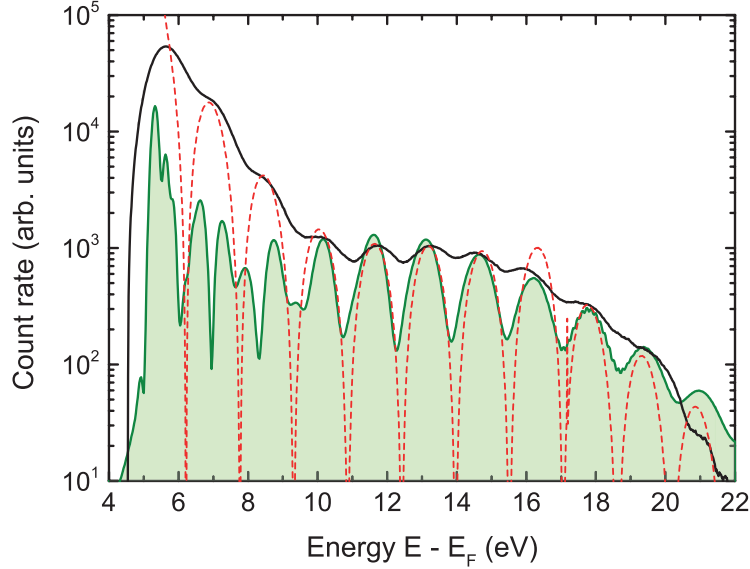


Figure 5.4: Integration of the time-dependent Schrödinger equation. A TDSE calculation (green curve) is compared to the experimental spectrum ($I_0 = 1.3 \times 10^{11} \text{ W cm}^{-2}$ from Fig. 5.1, black curve). The dashed red curve represents the Quantum Orbit Theory result from Fig. 5.3. The calculation parameters are the following: Laser peak field $E_0 = 11 \text{ GV m}^{-1}$, static field $E_{\text{DC}} = -0.4 \text{ GV m}^{-1}$, center wavelength $\lambda = 800 \text{ nm}$, pulse duration $\tau = 5.5 \text{ fs}$ and work function $\phi = 6 \text{ eV}$.

model. High-energy electrons are much more insensitive to the exact shape of the surface potential and other details of the simulation. A similar but more advanced TDSE calculation has recently appeared that shows very good agreement with our data even in the direct part [142].

The TDSE model shows that rescattering at a metal surface can be described by a fully quantum mechanical calculation. It corroborates the results of the semiclassical Quantum Orbit Theory.

Time-dependent density functional theory

The most realistic model presented in this thesis is the time-dependent density functional theory, introduced in subsection 2.4.2. Its main feature compared to the TDSE model is the inclusion of electron-electron correlation and other many-body effects characteristic for a metal. Decent agreement of the experimental data with the atomic physics models above is a good sign, but it is interesting to see what can be learned from a TDDFT simulation applied specifically to our experiment [34, 36].

Carrier-envelope phase averaged spectra calculated with TDDFT are shown in Fig. 5.5. Light pulses with a pulse duration of 6.4 fs and a center wavelength of 800 nm drive the electron dynamics of the model system. The work function ϕ was chosen as 6.2 eV. The Fermi energy with respect to the bottom of the metal pseudopotential well is 9.2 eV. A static field of -0.1 GV m^{-1} is applied to the surface. Calculated spectra are broadened by 0.5 eV to match the experimental spectrometer resolution. The spectra represent a scan of the laser electric peak field with $E_0 = \{4.1, 6.2, 7.7, 8.7, 9.8, 10.8\} \text{ GV m}^{-1}$ at

fixed static field. Clearly, the build-up of a high-energy plateau can be observed with increasing field strength. Rescattering takes place at the atom-like potential corresponding to a lattice site close to the metal-vacuum interface (Eq. 2.58). A good match with the experimental reference spectrum is found for a field strength of $E_0 \approx 10.2 \text{ GV m}^{-1}$ (intensity $I = 1.3 \times 10^{13} \text{ W cm}^{-2}$), in fair agreement with the models above.

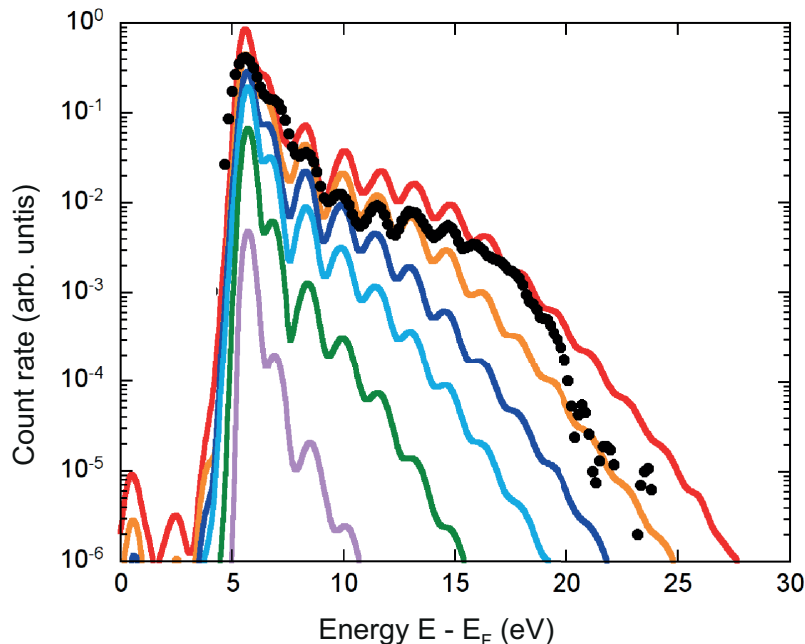


Figure 5.5: Spectra calculated with time-dependent density functional theory. Count rate as a function of electron energy for different laser field amplitudes. From below to above, the peak electric field is $E_0 = \{4.1, 6.2, 7.7, 8.7, 9.8, 10.8\} \text{ GV m}^{-1}$. The dotted black curve indicates the experimental reference spectrum. Best agreement is reached for a field of $\approx 10.2 \text{ GV m}^{-1}$. The calculation parameters are the following: Static field $E_{\text{DC}} = 0.1 \text{ GV m}^{-1}$, center wavelength $\lambda = 800 \text{ nm}$, pulse duration $\tau = 6.4 \text{ fs}$ and work function of $\phi = 6.2 \text{ eV}$. Taken from [36].

In order to explore the physics involved in the “black box” TDDFT calculation, a look at the electronic density $n(z, t)$ is helpful. Fig. 5.6 shows the absolute value of the density change $\Delta n(z, t) = |n(z, t) - n(z, -\infty)|$ as a function of space (spatial coordinate z) and time t in a logarithmic-scale color plot. The parameters are the same as before, with a peak field strength of $E_0 = 10.2 \text{ GV m}^{-1}$ and a carrier-envelope phase of $\phi_{\text{CE}} = \pi$. Also on display is the electric force exerted on the electrons by the laser field. The force is positive when the field has negative sign and pulls electrons out of the metal into the vacuum. The metal-vacuum interface is located at $z = 0$. The emission dynamics can be observed in the vacuum half-space ($z > 0$): Electron density is strongly driven out of the metal half-space when the electric field reaches a maximum, once every cycle. Vertical arrows mark this “pulsed” electron emission. When the laser field changes sign electrons are driven back to the surface where they rescatter approximately at the zero crossing of the field. The rescattered electrons show up as stripes with high slopes in the density plot. High slope corresponds here to a high electron velocity. Photoemission from the metal is dominated by electrons originating from the central two optical cycles of the

pulse. Contributions from these cycles interfere with each other; the stripes indicate interference structures that form the ATP peak structure in the spectrum.

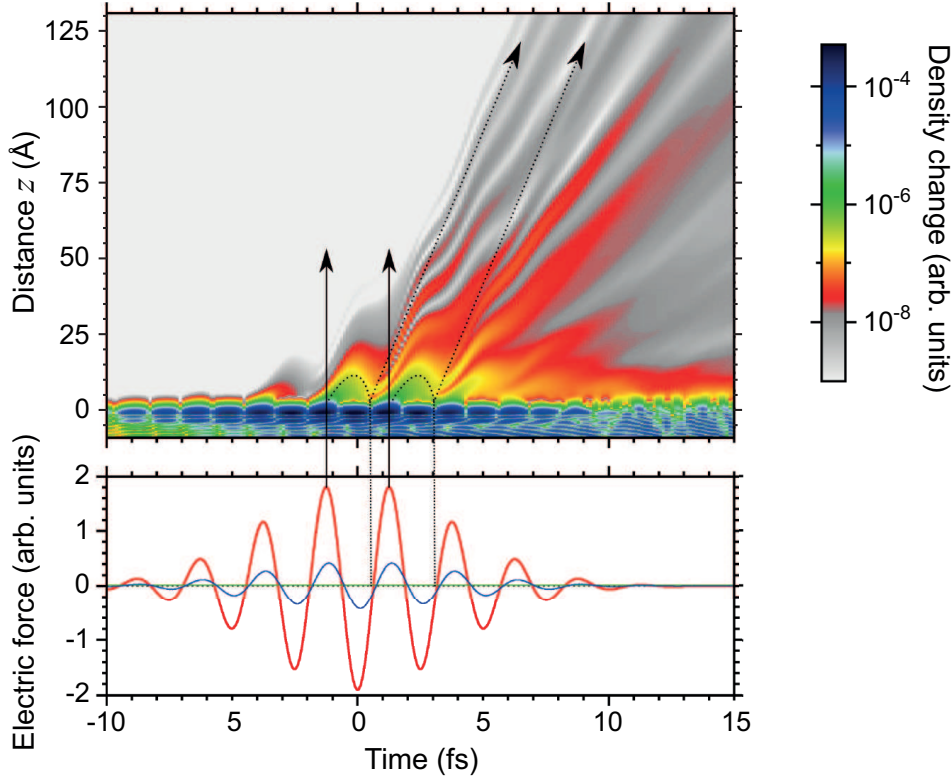


Figure 5.6: Electron density in time and space in a TDDFT calculation. Top panel: Absolute value of the time-dependent induced electron density $n(z, t) - n(z, -\infty)$. The tip is located at $z \leq 0$. Bottom panel: Time-dependent force exerted by the laser electric field (red) and the static field (green), and the induced dipole moment (blue). Emission happens mostly near the maxima of the electric field (solid vertical arrows). Electrons are subsequently driven back to the surface (dashed trajectories) and rescatter. Interferences in position space with increasing slopes (velocities) are detected as equidistant multiphoton peaks in the energy spectra. Taken from [36].

Inside the metal ($z \leq 0$), the laser field induces density fluctuations that screen the external laser field [36]. The induced density inside the solid is approximately 2 to 3 orders of magnitude larger than the emitted part of the density but is still two orders of magnitude smaller than the bulk electron density. Since on the electron time scale set by the Fermi momentum (~ 0.4 fs) the laser field varies slowly (optical cycle duration ~ 2.7 fs), this small fraction of the electron density can almost adiabatically adjust to the external field, screening it within a small surface layer of width ~ 5 Å. This is reflected in the induced dipole moment (blue curve in Fig. 5.6), which is almost in phase with the driving field.

The TDDFT simulation shown here provides valuable insight into the rescattering dynamics at a metal surface. The electron dynamics found in the simulation fully support the trajectory-based interpretation of the photoemission physics with the Quantum Orbit Theory. All theory models presented in this section agree well with the experimental data and with each other.

5.1.3 Influence of a static electric field

In the following, we explore the influence of the static electric field on rescattering. Theoretical investigations of atomic high-harmonic generation suggest a strong influence on electron dynamics and resulting spectra [143, 144, 145]. In contrast to gas-phase experiments, the nanotip system provides the possibility of applying high static fields. In order to avoid significant DC field emission, the maximum applicable absolute field is $\sim 2 \text{ GV m}^{-1}$, which is already close to that of the optical near-field (typically $\sim 10 \text{ GV m}^{-1}$). Fig. 5.7 shows electron spectra recorded at different field strengths $E_{\text{DC}} = -\{0.40, 0.66, 0.93, 1.44\} \text{ GV m}^{-1}$ at a fixed light intensity of $1.1 \times 10^{11} \text{ W cm}^{-2}$.

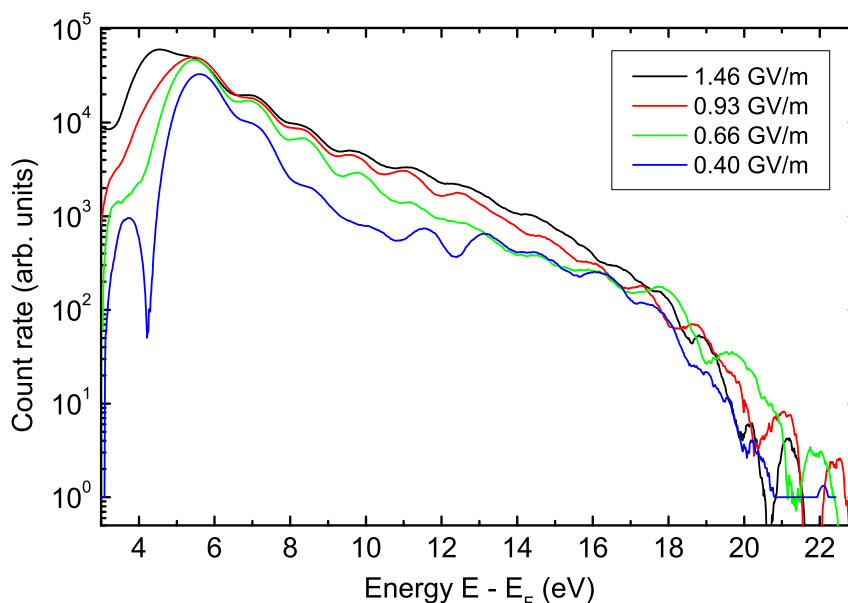


Figure 5.7: Influence of a static field on rescattering spectra. Experimental spectra recorded at different static field strengths at a light intensity of $1.1 \times 10^{11} \text{ W cm}^{-2}$. From bottom to top, the field strength is $E_{\text{DC}} = -\{0.40, 0.66, 0.93, 1.44\} \text{ GV m}^{-1}$. Taken from [34].

Three field-dependent effects are evident from the spectra. First, the plateau appears more and more tilted for increasing field strength. The high energy cut-off is only weakly affected by changes in the static field and has a slight tendency to shift towards lower energies for increasing field. Second, the overall peak visibility (or contrast) decreases with higher field. Third, the spectral cut-on shifts to lower energy and is found at an energy of $\sim 4.3 \text{ eV}$ for the highest static field. The shift of the cut-on is caused by the Schottky effect. An additional multiphoton peak corresponding to the absorption of three photons is observed at 4.5 eV .

We compare the experimental data from Fig. 5.7 to a TDDFT calculation for different static fields $E_{\text{DC}} = -\{0.2, 0.4, 0.6\} \text{ GV m}^{-1}$ (Fig. 5.8). A peak field strength of $E_0 = 10.2 \text{ GV m}^{-1}$ was chosen for the simulation. In agreement with the experiment, the spectral slope of the direct electrons decreases and the plateau appears less pronounced with increasing static field strength. The increasing overall field strength (light field and static field) leads to a broader longitudinal momentum distribution of the direct electrons [146] and hence to a smaller spectral slope of the direct part. Also the shift of

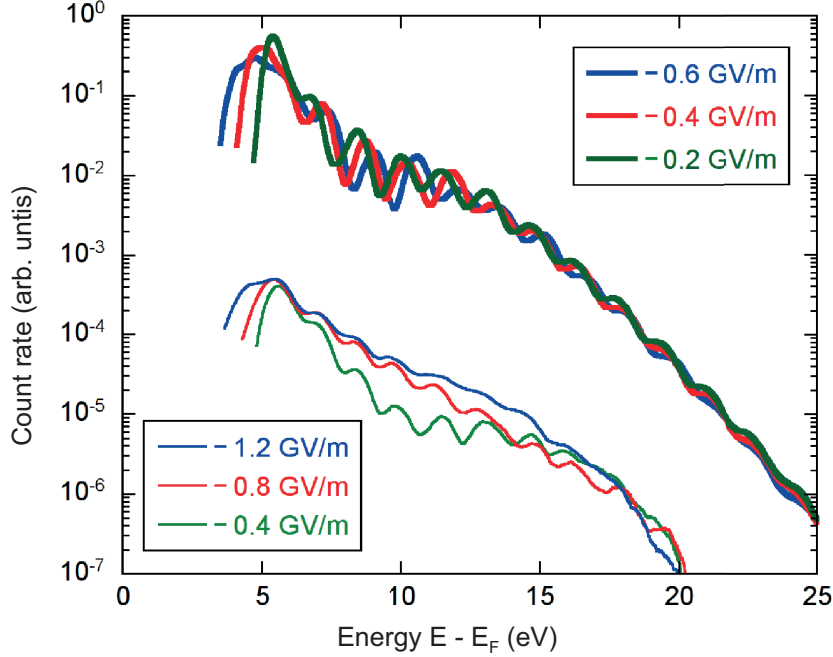


Figure 5.8: Static field dependence of rescattering spectra modeled with TDDFT. Experimental spectra from Fig. 5.7 (thin curves, lower graphs) are compared with TDDFT simulations ($E_{DC} = -\{0.2, 0.4, 0.6\}$ GV m $^{-1}$, upper graphs). The graphs are shifted vertically relative to each other for clarity. Taken from [36].

the cut-on is reproduced in the simulation. We observe, however, a qualitative difference between simulation and experiment. While in the experiment an increasing static field mainly reduces the visibility, in the simulation the main effect of an increased field is a shift in peak positions without a decrease in peak visibility. The origin of this difference remains to be investigated.

The experimental results show that high negative static fields change the characteristic shape of the plateau. The TDDFT model is able to capture most of the observed effects in a qualitative way.

5.1.4 Efficiency of rescattering at a metal surface

Rescattering at tips takes place at an extended surface comprised of many atoms. The efficiency of rescattering, i.e., the ratio in yield of plateau and direct part, is strongly influenced by the properties of the scattering object. For atomic or ionic systems with binding energies comparable to the work function of tungsten, ratios of 10^{-3} to 10^{-2} have been achieved at similar intensities [147, 148]. In our case we find a ratio of ~ 0.05 .

Quasiclassical Monte Carlo simulations in three dimensions were employed by Wachter *et al.* [34] in order to investigate the influence of an extended metal surface on rescattering, here summarized in brief. Ensembles of non-interacting electrons with longitudinal and transversal momenta distributed according to the Ammosov-Delone-Krainov theory of photoemission [74] were propagated along classical trajectories in the laser field of a 6.5 fs pulse. The scattering potential of the surface, here consisting of the topmost

atomic layer, was approximated with a muffin-tin potential and differential scattering cross sections were obtained. Using a transversal momentum width of 2.0×10^{-24} Ns, the electron ensemble spreads to an area of more than ~ 0.6 nm² upon recollision. This equals about 7.5 unit cells on the tungsten W(310) surface, hence rescattering can also take place at the neighboring atoms on the surface. 20 % of the *recolliding* electrons undergo elastic backscattering whereas the remaining 80 % are entering the metal after forward-scattering. According to the simulation results, the high density of scatterers on the surface and the significant large-angle scattering cross section for low-energy electrons are responsible for the high efficiency of rescattering at a metal surface.

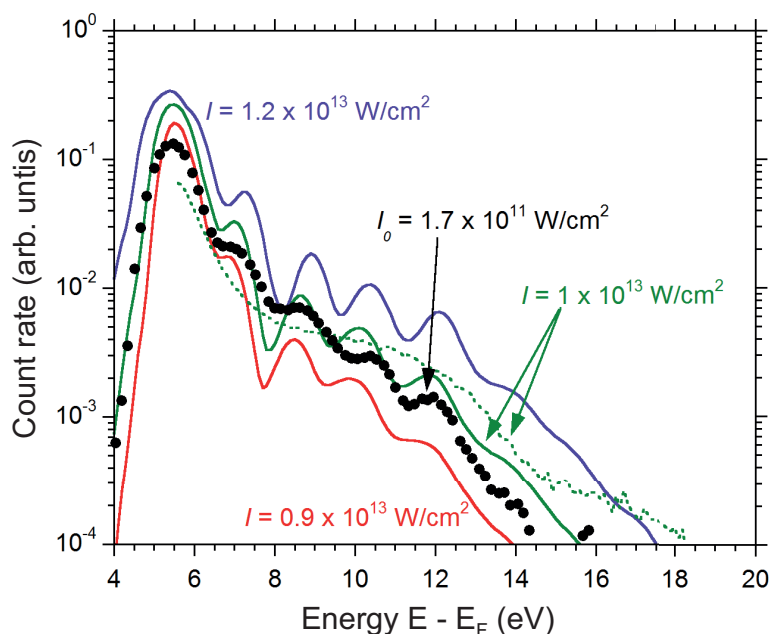


Figure 5.9: Rescattering spectrum modeled with quasiclassical Monte Carlo methods. An experimental spectrum (intensity $I_0 = 1.7 \times 10^{11}$ W cm⁻² and static field $E_{DC} = -0.7$ GV m⁻¹, black dotted curve) is compared with results from the quasiclassical Monte Carlo simulation (green dotted curve) and TDDFT (solid curves). The Monte Carlo simulation agrees well with experiment and TDDFT. Taken from [34].

Fig. 5.9 displays a spectrum calculated with a Monte Carlo simulation together with TDDFT results and an experimental spectrum (intensity $I_0 = 1.7 \times 10^{11}$ W cm⁻² and static field $E_{DC} = -0.7$ GV m⁻¹). The Monte Carlo simulation with peak intensity $I = 1 \times 10^{13}$ W cm⁻² agrees well with the corresponding TDDFT spectrum and the experimental data. The plateau area in the Monte Carlo simulation is even more pronounced than in the experimental spectra. The results clearly show that the structure of an extended metal surface enhances rescattering considerably compared to the atomic case.

5.2 Probing of optical near-fields by electron rescattering

In the following, a novel method to measure optical near-fields at nanostructures is presented and experimentally implemented with metal nanotips. It relies on rescattered electrons as a probe of the local field strength close to the surface of the tip's apex. The electron motion is governed by the spatial and temporal shape of the near-field and is therefore highly sensitive to it. In particular, the high-energy cut-off position is a useful indicator of the field strength since it scales linearly with intensity according to the $10 U_p$ cut-off law (Eq. 2.11). The Quantum Orbit Theory accounts for effects of the binding energy and predicts an approximate cut-off law given by

$$E_{\text{cut-off}} \approx 10.007 U_p + 0.538 \phi, \quad (5.3)$$

which is strictly valid only in the tunneling regime of photoemission [99] (see also the discussion in subsection 2.3.4 about Eq. 2.43). The cut-off position obtained from an exact Quantum Orbit Theory calculation and from the extended Three-Step Model lie within $\pm 12\%$ of this result at a local light intensity of $I = 1 \times 10^{13} \text{ W cm}^{-2}$ (Keldysh parameter $\gamma \sim 2$; see Fig. 2.15). Hence Eq. 5.3 is a reasonable approximation even in this regime. The intensity I can be directly calculated from the ponderomotive energy U_p from Eq. 2.5. In principle, the square root of the ratio of the local tip-enhanced intensity I and the intensity I_0 in the bare laser focus without the tip directly yields the field enhancement factor. However, also the spatial decay of the near-field in the vicinity of the tip surface has to be taken into consideration. At a local intensity of $10^{13} \text{ W cm}^{-2}$, an electron on a rescattering trajectory traverses a region of less than 1 nm distance from the surface and averages over the field distribution in this area. Numerical solutions of Maxwell's equations show that the near-field decays to its $1/e$ value within $L \sim 4 \text{ nm}$ from the tip surface for a gold or tungsten tip with a radius of 5 nm. Even for such a tip size, the maximum excursion of the electron trajectory is much smaller than the near-field decay length L . We can therefore safely assume that the near-field is constant over the electron's path and neglect any spatial variation. The following discussion of the method and its results is based on [37].

Experimental procedure

The aim of the experiment is to measure the field enhancement factor for tips of different material and size. We chose tungsten and gold as tip materials. The experimental implementation of the method is straightforward with our setup. We measure photoelectron spectra and infer the cut-off energy $E_{\text{cut-off}}$ from the intersection point of two exponential decay fits. The average laser power is adjusted in such a way that a particular cut-off energy is reached. We obtain the field enhancement factor from the enhanced intensity I , inferred from $E_{\text{cut-off}}$, and the nominal incident laser intensity I_0 . This procedure is repeated for tips of different size and material. In our experiment, we chose $E_{\text{cut-off}}$ to be 15 eV with respect to the Fermi energy E_F . With an effective barrier height ϕ_{eff} of 5.2 eV, this cut-off energy corresponds to an intensity $I = 1.09 \times 10^{13} \text{ W cm}^{-2}$. For the determination of I_0 from the laser power, the knowledge of the focal spot size w_0

is required. We measure w_0 both with optical microscopy and with an *in-situ* method based on photoemission from the tip. For the latter, we record the photocurrent as a function of tip position in the focus and reconstruct the local intensity profile from the relationship of current and intensity given by the multiphoton power law (Eq. 2.2).

For the investigation of tungsten, we used a single W(310) nanotip. Different tip sizes were achieved by gradual blunting of the tip by field evaporation and, in the final step, by heating the tip to a temperature of more than 1000 K. The tip radius r in each blunting stage was inferred from FIM images with the help of the ring counting method (see Fig. 5.10(a)–(d)). The radius in the last blunting stage could only be determined from a scanning electron microscope image (see Fig. 5.10(e)). In total, rescattering spectra for five different tip radii ranging from 8 to 51 nm could be recorded (see Fig. 5.10(f)).

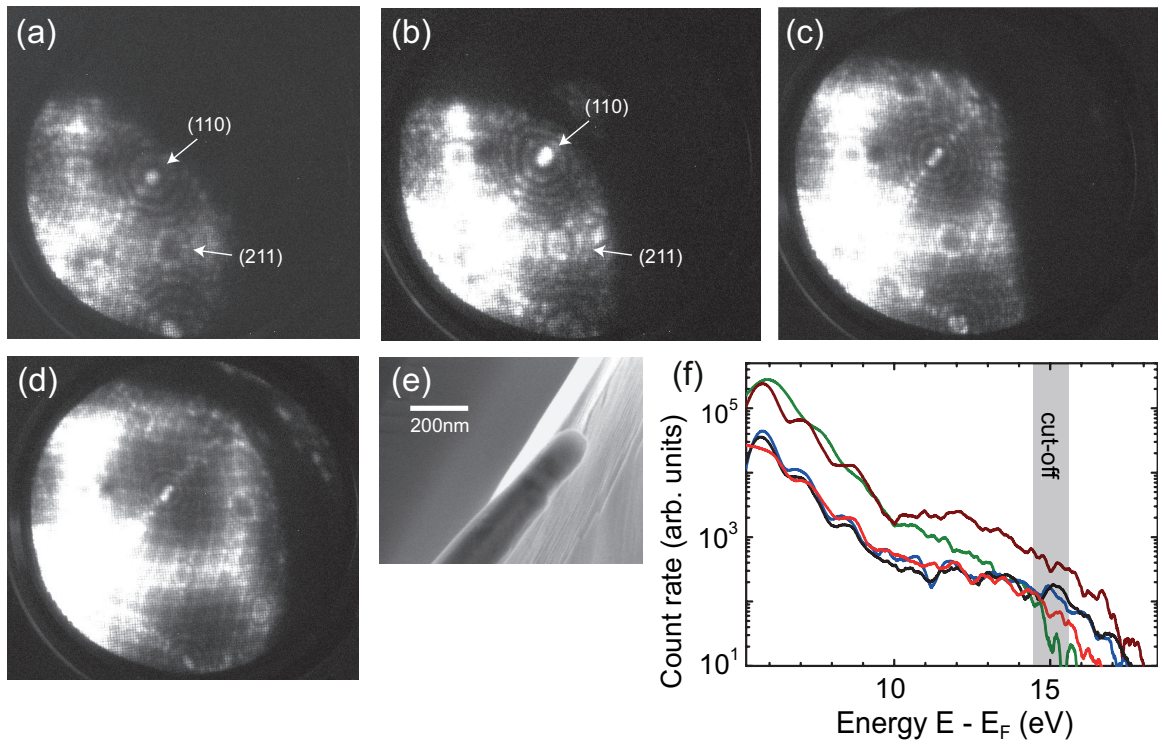


Figure 5.10: Characterization of tungsten tips. (a)–(d) FIM images of a W(310) tip in various blunting stages. The tip radius r is inferred from the ring counting method. (a) $n = 5 \pm 1$ rings, $r = (8.4 \pm 1.7)$ nm. (b) $n = 8 \pm 1$, $r = (13.4 \pm 1.7)$ nm. (c) $n = 9 \pm 1$, $r = (15.0 \pm 1.7)$ nm. (d) $n = 11 \pm 2$, $r = (18.4 \pm 3.4)$ nm. (e) SEM micrograph of the tip in the last blunting stage, $r = (51 \pm 5)$ nm. (f) Corresponding photoelectron spectra (red: 8 nm, black: 13 nm, blue: 15 nm, brown: 18 nm, green: 51 nm).

Controlled gradual blunting and *in-situ* FIM characterization of a gold nanotip is not possible in our setup. Therefore we used three different polycrystalline gold tips and measured their radii with an electron microscope after each individual measurement in order to obtain a reliable value for r . Fig. 5.11 shows SEM images of the gold tips. The tips vary strongly in their shape. While the tip shown in (a) is similar to the tungsten tip in Fig. 5.10(e), the tip in (b) has a much larger opening angle. The gold tip in (c) exhibits an almost spherical protrusion in its apex region with a radius of $r = (28 \pm 4)$ nm.

Fig. 5.11(d) shows photoemission spectra measured with these tips.

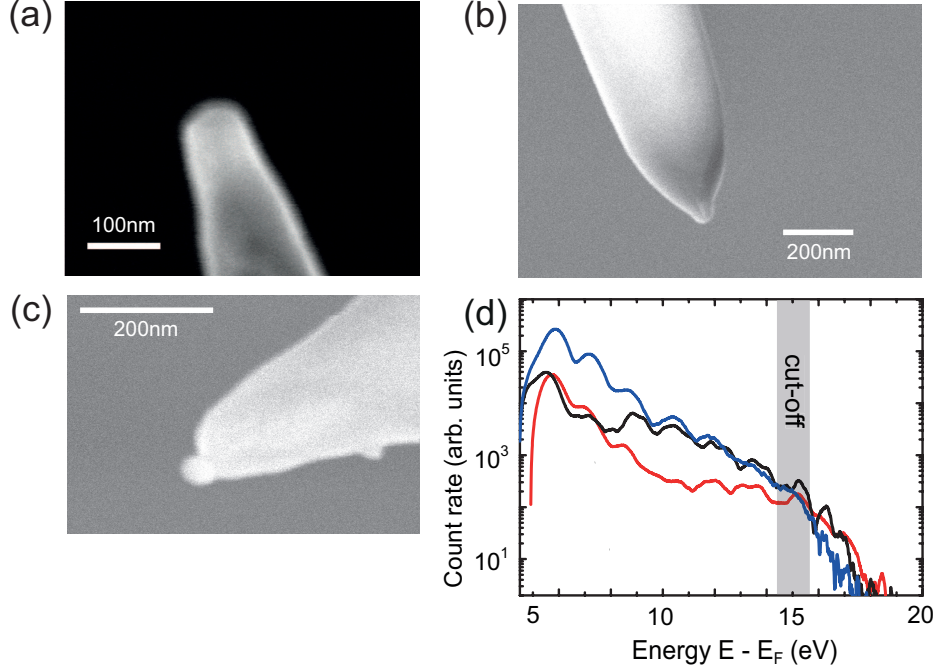


Figure 5.11: Characterization of gold tips. SEM micrographs of gold tips with (a) $r = (46 \pm 3)$ nm, (b) $r = (31 \pm 3)$ nm and (c) $r = (28 \pm 4)$ nm. (d) Corresponding photoelectron spectra (red: $r = (46 \pm 3)$ nm, black: $r = (31 \pm 3)$ nm, blue: $r = (28 \pm 4)$ nm). A plateau and a pronounced high-energy cut-off are observed, very similar to tungsten.

Results

Fig. 5.12 shows the extracted field enhancement factors $\xi = \sqrt{I/I_0}$ for tungsten and gold as a function of tip radius r . For tungsten, the field enhancement factor increases from 2.6 ± 0.6 for $r = (51 \pm 5)$ nm to 5.7 ± 0.6 for $r = (8.4 \pm 1.7)$ nm. For gold, ξ ranges from 3.3 ± 0.6 for $r = (46 \pm 3)$ nm to 3.5 ± 0.5 for $r = (28 \pm 4)$ nm. The uncertainty in ξ is due to an estimated systematic error in the nominal intensity I_0 of $\pm 30\%$.

Fig. 5.12 also displays the results of fully-independent numerical solutions of Maxwell's equations for the different tip geometries and materials (see Section 2.5). 5.5 fs laser pulses at 800 nm wavelength were used in the calculations. The experimental values for ξ agree well with the numerical results within the error bars. Both experiment and theory show that ξ increases smoothly for decreasing tip radii. The smaller the nanostructure size relative to the wavelength the stronger the induced near-field becomes.

A comparison with literature values of field enhancement factor of tungsten tips (experiment [149, 150] and theory [149, 111]) yields good agreement. For gold tips, however, both experimental [30, 150] and theoretical values [111, 151] disagree on ξ . For tip sizes comparable to ours, some authors report on higher enhancement factors ranging from 8 to 25, inferred from field-enhanced second harmonic generation from the tips [30, 150, 151]. Our experimental and theoretical results for gold suggest that the field enhancement is dominated by the geometric effect, just like for tungsten. A possi-

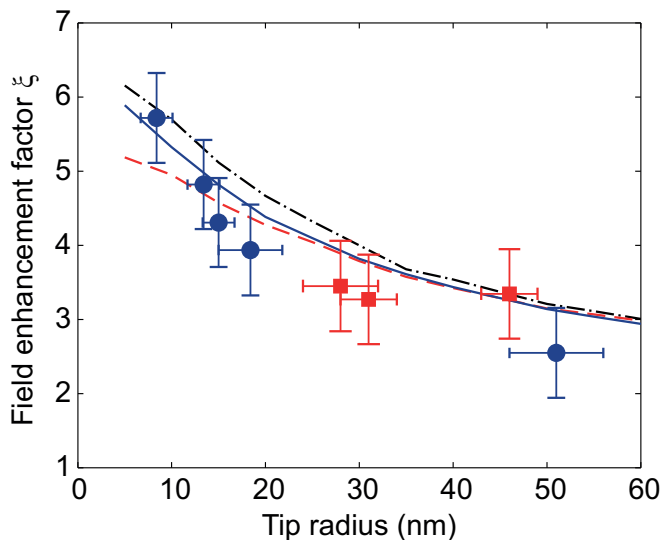


Figure 5.12: Field enhancement factor of tungsten and gold tips with different radii. Experimental results for the field enhancement factor of tungsten tips (blue dots) and gold tips (red squares) as a function of the tip radius. The uncertainty in ξ represents an estimated systematic error due to the uncertainty in laser intensity. The lines are simulation results for 800 nm (W: solid blue line, Au: dashed red line, Ag: dash-dotted black line).

ble explanation for the disagreement with results from other investigations is that the near-field at plasmonic materials like gold is exceptionally sensitive to the geometry of the tip (the opening angle in particular [111, 152]) and its surface condition. This is supported by the large variance in enhancement factors at gold tips reported in [150]. In our experiments with gold tips, we do not observe a large variance of field enhancement factors even though not all the tips had the ideal conical shape assumed in the simulations (see Fig. 5.11). A possible reason for this is that, before any measurement, we use field ion microscopy in conjunction with field evaporation to clean the tip surface and to ensure that the tip is almost ideally spherical in the vicinity of the apex. This is likely not the case in many other experiments. Evidently, more research is needed to fully understand the behavior of tips made of plasmonic materials. Such an investigation is beyond the scope of this thesis.

Simulations of tips with arbitrary dielectric constants ϵ suggest that the field enhancement factor essentially depends on the absolute value of ϵ [37]. $|\epsilon|$ is similar for tungsten and gold, which explains their similar field enhancement factors. An interesting alternative to these materials is aluminum ($\epsilon = -64 + 47i$ at 800 nm): The calculated field enhancement factor is 7.6 for a tip radius of 10 nm. Research on the fabrication of aluminum tips is ongoing in our group. Also tips from any dielectric material should show high field enhancement. This is intriguing in the light of high-harmonic generation in dielectric bulk materials, which has been demonstrated only recently [153].

Implications for Quantum Plasmonics

Recently, theoretical and experimental investigations of quantum effects in nano-optics appeared [154, 155, 156], opening up the field of quantum plasmonics. An effect proposed

by Zuloaga *et al.* [154] could influence the near-field at tips: The metal-vacuum boundary should not be considered as infinitely small, as classical electrodynamics usually assumes. Instead, the excited surface charge density extends several Ångströms over the surface boundary and effectively smears it out. In order to quantify this effect, Zuloaga *et al.* performed self-consistent calculations of the fields around gold spheres with radii < 2 nm. They found that the enhanced near-field is reduced in strength with respect to classical calculation results at distances smaller than 0.5 nm from the surface boundary.

An analysis of the length scales present in our experiment shows that our system is sensitive to potential quantum plasmonic effects. The maximum excursion length of an electron that undergoes rescattering is ~ 1 nm; the electron integrates over the enhanced near-field in close proximity of the surface. Our results (see Fig. 5.12) show that the experimental field enhancement values are not much lower than the results of the classical theory as quantum plasmonics would predict; both experiment and theory agree well within the error bars. This shows that quantum plasmonic effects do not play a big role in our system.

The novel method presented in this section can be extended to a full tomographic reconstruction of the near-field. An intensity scan will lead to a variety of electron excursion lengths. It is then possible to explore the spatial field decay on the axis defined by the tip's pointing direction. Finally, angularly resolved spectral measurements should enable a full three-dimensional scan of the near-field.

6 Attosecond control of electrons with the carrier-envelope phase

In the following, we will perform spectrally-resolved studies of the field dependence of the rescattering process, here for the first time at a metal surface. Well-controlled optical waveforms are provided by carrier-envelope (CE) phase stable laser pulses. The CE phase is defined as the relative phase between carrier field and intensity envelope (see Fig. 6.1).

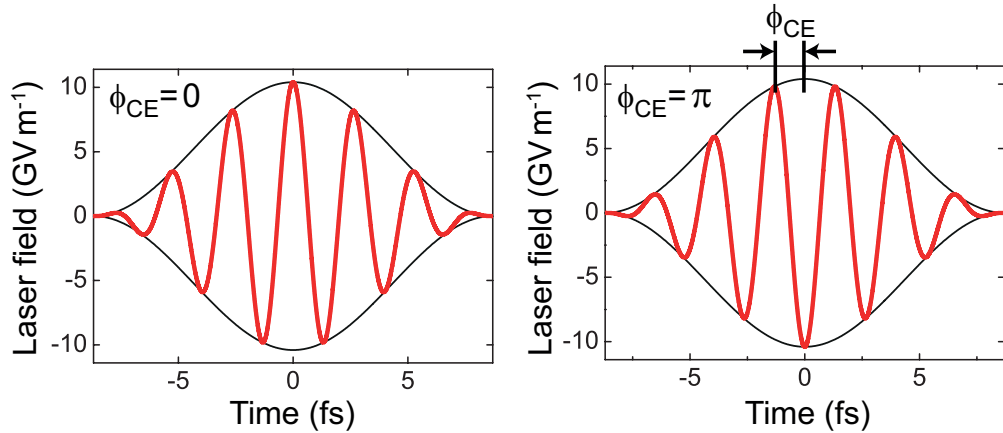


Figure 6.1: Carrier-envelope phase of few-cycle laser pulses. Electric field of a few-cycle pulse (red curve) as a function of time for two different carrier-envelope phases $\phi_{CE} = 0$ (left panel) and $\phi_{CE} = \pi$ (right panel). ϕ_{CE} is defined as the phase shift between the pulse envelope (black) and the underlying carrier wave. The pulse length is 6 fs at a center wavelength of 800 nm.

Tuning the phase does not change the shape of the intensity envelope, but causes a phase shift of the underlying carrier field. For a laser pulse comprised only of a few optical cycles, the CE phase plays a decisive role since it breaks the field symmetry of the pulse in the two opposite directions along the laser polarization axis. In particular, the peak electric field of such a pulse crucially depends on the phase. CE phase effects have been observed in a large variety of strong-field experiments with atomic gases [9, 98, 157], molecules [158], dielectric nanoparticles [102], and also in photoemission from a flat gold cathode [159]. The following investigation represents one of the main results of this thesis. Its discussion is based on [33, 35, 160].

6.1 Phase effects in rescattering

In the following, we investigate the effects of the CE phase on above-threshold photoemission (ATP) spectra from a tungsten tip. The CE phase stabilization (see Section 3.1) of the Ti:sapphire laser oscillator is active here, providing phase-stable 6-fs pulses at 800 nm with a root-mean-square phase variation below 100 mrad/min. The laser light is focused on a W(310) nanotip with a pulse energy of 240 pJ, which corresponds to a cycle-averaged peak intensity of $I_0 = 4 \times 10^{11} \text{ W cm}^{-2}$, not including field enhancement. The chosen intensity is a factor of two smaller than the damage threshold intensity where current instabilities and surface migration of atoms set in. The waveform of the incident laser pulse matches well the waveform of the near-field at the tip up to a constant shift of the CE phase (see Section 2.5). The tip radius of curvature is estimated to be in the range of 10...20 nm, inferred from two methods. *Ex-situ* SEM imaging gives an upper bound of 30 nm. The ring counting method in an *in-situ* FIM image yields a radius of about 10 nm. The tip is biased with -50 V , leading to a static electric field of $\sim -0.4 \text{ GV m}^{-1}$ at the tip apex.

Fig. 6.2(a) shows a phase-averaged photoelectron spectrum. The average electron yield is only about one electron per pulse. In contrast to the spectra shown in the previous chapters, we display here the kinetic energy of the photoelectrons, i.e., it is not referenced to the Fermi energy. Zero kinetic energy (vacuum level) is defined as the position of the spectral cut-on at ϕ_{eff} , reflecting the effective barrier height. The spectrum is very similar to those in the last chapter: After the cut-on we initially find a strong exponential decay of the count rate arising from direct photoelectrons. Starting with a kinetic energy of $\sim 4.5 \text{ eV}$, a plateau structure is observed, a clear sign of rescattering and recollision. The plateau is terminated by a soft cut-off located at $\sim 13 \text{ eV}$ where the count rate rapidly decreases again. All over the spectrum we observe ATP peaks spaced approximately by the photon energy (1.55 eV).

The color plot in Fig. 6.2(b) displays the electron count rate as a function of kinetic energy and CE phase offset. The CE phase offset is defined as the sum of the actual CE phase ϕ_{CE} of the laser-induced near-field and a constant experimental phase difference, which is initially unknown. Here the latter is calibrated to 0, inferred from a comparison to theory (see Section 6.3). We recorded 16 integrated spectra with an energy scan step size of 13 meV and a time window of 5 ms for counting photoelectron events at each energy position. Subsequently we smoothed the resulting spectrum with the Savitzky-Golay algorithm [123] spanning 1.5 eV. Careful smoothing was also applied along the CE phase axis. A second-order Savitzky-Golay smoothing algorithm involves 5 neighboring data points only, balancing successful smoothing with a possible loss of information. The resolution including the smoothing procedures is estimated to be about 500 meV. In total, 2π in the CE phase was covered with a spacing of $\pi/8$. For better visibility, the measured data in the figure is extended over 4π .

When varying the phase the count rate at a given kinetic energy is modulated. Two cuts through the spectrum at energies 2.8 eV and 14.8 eV (Fig. 6.2(c)) reveal that this modulation is approximately sinusoidal in the phase. It is also evident that the count rate reaches its maximum at different CE phase offsets throughout the spectrum. The depth of the modulation as a function of kinetic energy is displayed in Fig. 6.2(a). It is defined as $(N_{\text{max}} - N_{\text{min}})/(N_{\text{max}} + N_{\text{min}})$, where N_{max} is the maximum and N_{min} the

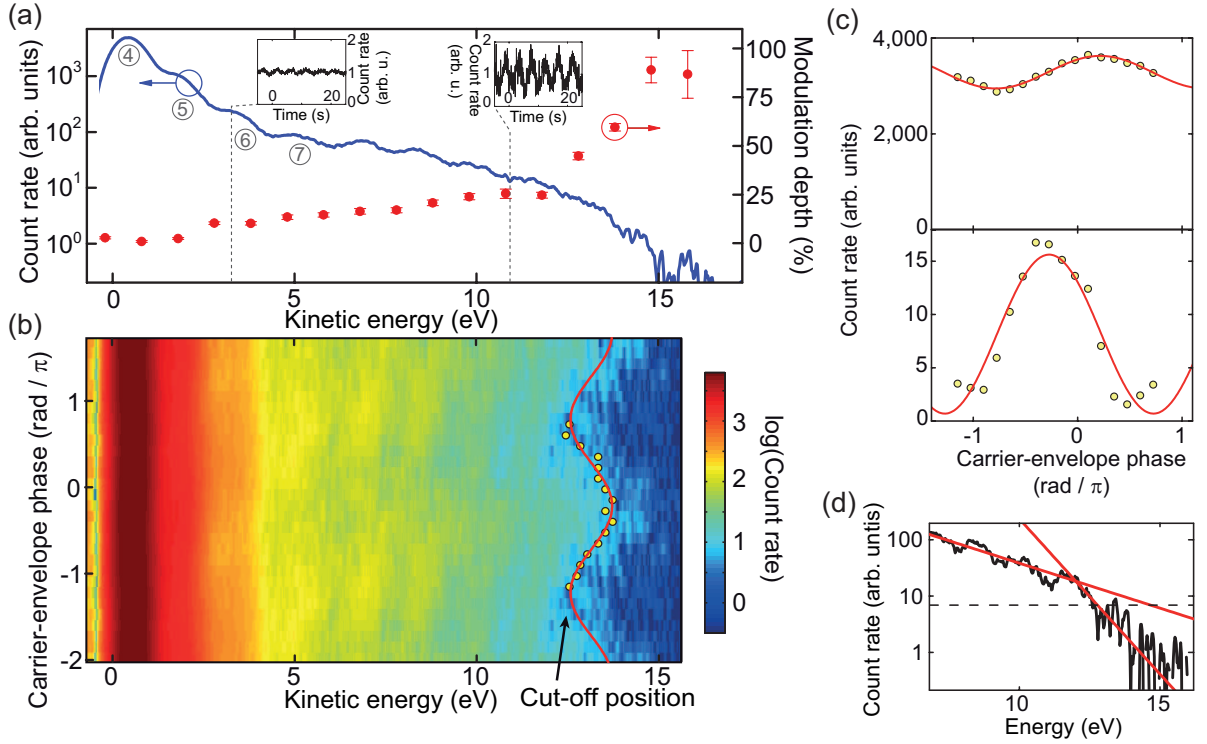


Figure 6.2: Carrier-envelope phase resolved photoelectron spectra. (a) Carrier-envelope phase averaged photoelectron spectrum (solid blue curve). The energy axis reflects the kinetic energy E_{kin} of the photoelectrons (see text). Starting with the four-photon peak (the photon order is indicated by encircled numbers), three multiphoton orders are visible in the direct part. At an energy of ~ 4.5 eV the plateau part begins with five more peaks. The red points show the modulation depth of the count rate at the given energy when changing the carrier-envelope phase. At energies above 14 eV the count rate is almost fully modulated. Insets: Carrier-envelope phase modulation in the photocurrent with the spectrometer acting as an energy high-pass filter at 3 eV (left inset) and 11 eV (right inset; both with the carrier-envelope offset frequency set to $f_{\text{CEO}} = \dot{\phi}_{\text{CE}}/2\pi \sim 0.2$ Hz). (b) Color plot of the electron count rate in logarithmic scale as a function of energy and carrier-envelope phase offset. The phase was changed by $\pi/8$ for each spectrum. The measured data range over 2π and are extended over 4π for better visibility. The circles depict the high-energy cut-off position as a function of carrier-envelope phase (red solid curve: sinusoidal fit). (c) Count rate modulation as a function of the carrier-envelope phase offset at an energy 2.8 eV (upper plot) and 14.8 eV (lower plot) in linear scale. The red curves show sinusoidal fits to the data. (d) Single spectrum recorded at carrier-envelope phase offset -0.9π in logarithmic scale. Two different exponential slopes (red curves) are fitted to the count rate nearby the cut-off. The cut-off position is defined as the intersection of the fit to the steeper slope with a (dashed) horizontal line of constant count rate (7 arb. units).

minimum count rate at a given energy. N_{max} and N_{min} are determined with the help of sinusoidal fits (Fig. 6.2(c)). The modulation depth varies from a few percent at low energy to $\sim 25\%$ in the plateau part and reaches almost 100% in the region after the cut-off at 13 eV. In the latter energy region, the CE phase determines almost completely if photoelectrons are detected or not. In other words, these high-energy electrons are

subject to an ultrafast switching mechanism created by the laser electric field and its temporal structure.

Directly evident from Fig. 6.2(b) is a pronounced modulation of the cut-off position with the CE phase. This modulation is strongly related to the switching mechanism discussed above. In order to quantify this effect we determined the cut-off position for each single spectrum. As already done in the previous chapter, exponential decay curves were fitted to the plateau and the subsequent decay. We found, however, that taking the intersection of the exponential slopes as the cut-off position is not sufficiently robust against noise in the data. Therefore the cut-off was derived from the intersection of the steeper slope with a constant count rate of 7 count rate units (see Fig. 6.2(d)). The result is shown in Fig. 6.2(b) in the form of yellow dots. The cut-off position is approximately sinusoidally modulated and ranges from 12.3 eV at phase offset -0.2π to 13.6 eV at phase offset 0.8π . We will see that modulation of the cut-off position and the related switching behaviour can be explained with classical considerations – photoelectrons moving on classical trajectories in a laser field. The observed effects result from high sensitivity of rescattered electrons to asymmetries in the laser electric field and accordingly to the (CE phase dependent) maximum field strength in the pulse (see also [98]).

6.1.1 Carrier-envelope phase sensing

Phase sensing and stabilization is performed with all-optical f -to- $2f$ interferometers building on the frequency comb technique. The results above show that photoemission from tips can also serve as a meter of the phase due to the high sensitivity of rescattered electrons. Before the advent of the frequency comb, a proposal considered tunneling photoemission from solids as a probe for the CE phase of ultrashort laser pulses [161]. Theoretical studies predicted strong effects in both the multiphoton and the tunneling regime of photoemission from metal surfaces [162, 163]. The first observation of CE phase effects at a metal surface was performed with a flat gold photocathode irradiated with ultrashort near-infrared laser pulses [159]. Despite a pulse duration of only 4 fs, only a very small modulation of the total photocurrent with the phase was detected, whose magnitude and contrast are not even mentioned in the paper. Our spectrally resolved measurements presented here clearly show that much larger phase effects are found in electron rescattering from a metal nanopip. Fig. 6.2(a) shows that a measurement limited to plateau electrons should provide modulation depths of $\sim 25\%$ or higher.

The electron spectrometer with constant filter voltage can act as an energy high-pass filter. The insets of Fig. 6.2 shows two normalized modulation curves recorded at a filter energy of 3 eV and 11 eV, respectively. Here the carrier-envelope offset frequency, the time derivative of the CE phase, is set to $f_{\text{CEO}} = \dot{\phi}_{\text{CE}}/2\pi \sim 0.2$ Hz. An approximately sinusoidal current oscillation is detected. As expected, the modulation depth increases significantly with the filter energy, but at the cost of count rate. For 11 eV, on average $\sim 10^{-6}$ electrons per pulse are detected.

An improvement is provided by the use of a simpler version of the retarding field spectrometer (see [119] for details). Two fine mesh grids facing the tip are used for electron acceleration and subsequent high-pass energy filtering. The resulting photocurrent is recorded with the MCP detector. A photocurrent corresponding to $\sim 10^{-3}$ electrons per pulse could be achieved using a filter energy of about 10 eV. With further improvement

of the count rate, detection and stabilization of the carrier-envelope offset frequency might be possible (see [119] and the outlook in Chapter 7).

Apart from the overall modulation of the count rate and a phase dependent shift of the rescattering cut-off, also the peak structure is strongly influenced by the CE phase. In the following, we will perform a detailed investigation of this effect.

6.2 Attosecond double-slit experiment

In this section, we will leave the classical domain and discuss effects arising from the matter-wave nature of the electron. Among the most beautiful demonstrations of this aspect are electron diffraction at solid crystals, first observed by Davisson and Germer in 1927 [164] and the double-slit experiment with electrons, performed by Jönsson in 1961 [165]. Jönsson found that the double slit causes a fringe pattern on a distant screen, in full analogy to the optical version of Young’s double-slit experiment. The field of electron interferometry was born that explores diffraction and interference effects mostly in the spatial domain (see [166] for a recent review).

Moshinsky proposed a new matter wave effect in 1952, namely diffraction in time [95]. He showed that a temporal analogue to diffraction in space can be constructed. The scenario is the following: A matter wave impinges on a time-dependent shutter that is suddenly opened. Moshinsky showed that the probability density of the transmitted wave function measured at a given spatial position as a function of *time* shows a Fresnel diffraction pattern, in full analogy the pattern obtained from *spatial* diffraction at a straight edge. This effect manifests itself in fringes in the energy domain. Also the spatial double-slit experiment can be transferred into the time domain [96]. Shutters (or slits) that open only for a short time cause interference structures in the energy domain, provided that the released matter waves overlap in time [167]. For a double slit in time, the resulting fringe spacing ΔE of the spectral interference structure is related to the temporal separation Δt of the slits by the Fourier relation $\Delta E \sim h/\Delta t$ (see subsection 2.3.3). Likewise, the width of the envelope of the spectral fringe pattern is governed by the temporal width of a slit via the same relation. All this is reminiscent of the time-energy uncertainty relation $\Delta E \cdot \Delta t \geq \hbar/2$ in quantum mechanics. We do not know which slit the electron has passed through (“which-way scenario”). As a consequence, an interference pattern results in the energy domain. This underlines the intricate relationship of time and energy in quantum mechanics.

Temporal slit experiments have been realized with ultracold atoms [168], neutrons [169] and is explored currently also with large molecular clusters [170]. Closely related to our experiment, temporal slit effects have been also been found in strong-field ionization of atomic gases by CE phase stable laser pulses [171]. Depending on the phase, the waveform of the laser field can create scenarios where the electron passes through one or two slits or even a “grating” in time [94]. We find a similar effect for rescattered electrons in our experiment.

Spectral interference manifests itself in peaks in our experimental photoelectron spectra. The spectra depicted in Fig. 6.2 suggest that the peak structure is strongly affected by the CE phase. In order to show these effects as clearly as possible both in the strongly decaying direct part and in the flat plateau part, we divided the measured count rate

in each of the two regions by an exponential decay curve approximating the respective shape (see Fig. 6.3(a)). The resulting count rate is called normalized count rate. The color plot in Fig. 6.3(b) shows the normalized count rate as a function of energy and phase in a linear plot. Another effect is now more evident: The visibility (or contrast) of the peaks in the plateau varies strongly with the CE phase.

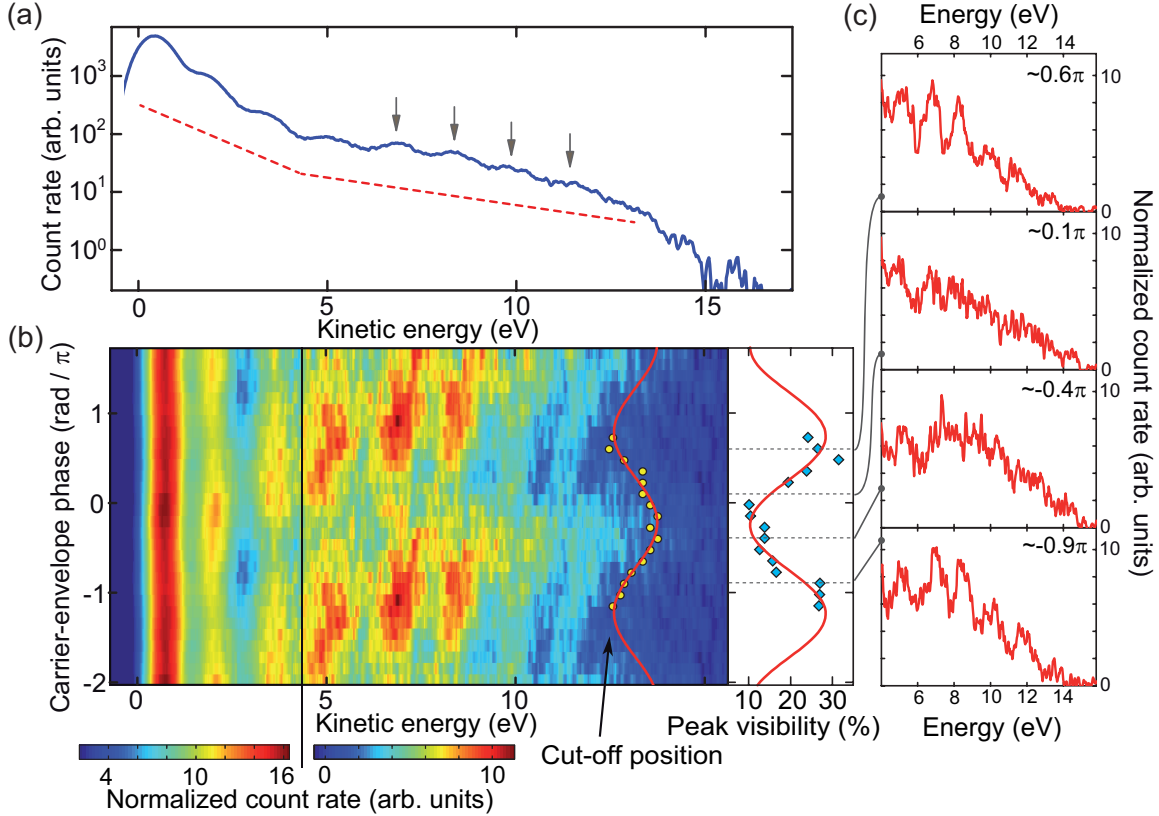


Figure 6.3: Phase-dependent spectral interference effects. (a) Carrier-envelope phase averaged photoelectron spectrum (solid blue curve). The dashed red lines indicate two exponential decay curves used to derive a normalized count rate (see text). Peaks marked with arrows are analyzed for their visibility (or contrast). (b) Color plot of the normalized electron count rate in linear scale as a function of energy and carrier-envelope phase offset. The direct part (energies < 4.3 eV) and the plateau were normalized separately. The visibility of the marked peaks (blue diamonds) is shown along with a sinusoidal fit (red curve). For comparison, also the cut-off modulation from Fig. 6.2 is displayed. Cut-off position and peak visibility are nearly maximally out of phase. (c) Normalized count rate as a function of kinetic energy for four different CE phase offsets. Only the plateau part is shown. Fringes are clearly visible for 0.6π and -0.9π , but almost no fringes are visible for 0.1π and -0.4π .

The average visibility of four selected peaks in the plateau is shown in Fig. 6.3(b). The visibility of a single peak is defined as $(A - B)/(A + B)$ where A is the count rate at the peak's maximum and B is the average of the count rates of the two minima next to the peak. A and B are determined with the help of multiple Gaussian peak fits. For a phase offset of $\sim 0.8\pi$ the visibility is highest ($\sim 30\%$), for $\sim -0.2\pi$ lowest ($\sim 10\%$). The corresponding spectra are shown in Fig. 6.4. Interestingly, the modulation of peak visibility and cut-off position is maximally out of phase; the phase difference is

$\pi + (80 \pm 160)$ mrad.

Our observation can be interpreted as a slits-in-time scenario (see Fig. 6.4): The generation of high-energy (rescattered) photoelectrons is possible only during certain windows or slits in time. Wavepackets are generated that overlap in the spatial domain on the way to the detector and interfere with each other. As already discussed above, the temporal structure of the slits and the energy distribution of the resulting (far-field) matter wave packet are related by Fourier transformation. It is therefore possible to draw conclusions about the time domain with information from the spectral domain. The spacing of the spectral peaks that is approximately the photon energy ($\Delta E \approx 1.55$ eV) translates into the temporal spacing Δt of two (or more) slits in time, $\Delta t \sim \Delta E/h = 2.68$ fs. This value corresponds to the duration of one optical cycle of the laser pulse. Hence plateau electrons are only generated in time windows that are approximately spaced by the duration of an optical cycle. As explained later in the theory considerations of the next section, Δt can be identified with the difference of the rescattering times of two subsequent electron wave packets. With Fourier transformation, one can also estimate the temporal width of the slits in time. Assuming that all plateau electrons originate from rescattering, the spectral width of the plateau (~ 9 eV) translates in the temporal width of a single slit, which can be estimated to ~ 450 as. The interpretation presented here in terms of matter-wave interference in time and energy domain complements the multiphoton picture of ATP.

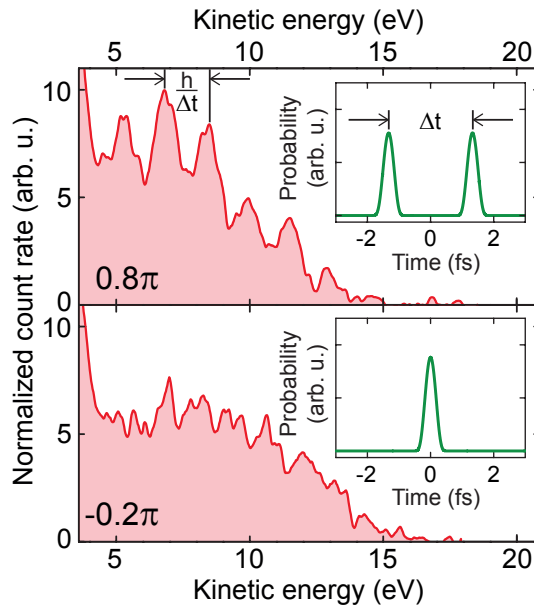


Figure 6.4: Slits-in-time interpretation of spectral interference effects. For a carrier-envelope phase offset of $\sim 0.8\pi$ (upper plot), a pronounced peak structure with a spacing of the photon energy is found due to spectral interference. For the reversed phase offset of $\sim -0.2\pi$ (lower plot), no pronounced peaks are visible. The insets schematically depict the time-domain picture: Depending on the carrier-envelope phase, high-energy plateau electrons are generated by rescattering during two slits or one slit in time (indicated by the solid curves), resulting in the presence or absence of spectral interference. The time axis has an arbitrary offset.

6.2.1 Carrier-envelope phase spectral interferometry

The spectral interference effect suggests that the rescattering process in our system is coherent, meaning that the phase coherence of the electron matter wave packets is conserved throughout the whole process. Wave packets (or actually components of a single wave packet) that are appearing at different time instants interfere with each other; photoelectron spectra represent interferograms that encode the temporal dynamics and quantum phases of the wave packets. Recently, we introduced a spectral interferometry method [160] that is able to decode the temporal information contained in spectra of coherent processes with attosecond precision. In the so-called carrier-envelope phase spectral interferometry (CEPSI) method, spectra are recorded with varying CE phase. The spectral region of interest is then Fourier transformed in order to reveal amplitude and phase information on wave packets and their temporal dynamics. The method was applied to high-harmonic generation, but can also be applied to coherent strong-field photoemission.

Our spectral region of interest is the plateau part starting at 5 eV as shown in Fig. 6.3(b). Fig. 6.5 presents the results of a CEPSI analysis of the plateau [160]. Fourier amplitude and phase are plotted as functions of Fourier time and CE phase. The Fourier time reveals the temporal separation of the wave packets leading to the spectral peaks. A peak is found in the Fourier amplitude plot (Fig. 6.5(a)) at time ~ 2.8 fs, representing the delay of the two wave packets in the temporal double-slit scenario. As expected, this delay agrees fairly well with the optical cycle duration (2.68 fs) at 800 nm wavelength. The absence of the peak for $-0.3\pi < \phi_{\text{CE}} < 0.3\pi$ can be directly interpreted as the single-slit case. Upon a closer look at the peak, the analysis reveals a shift of the temporal delay of the two wave packets, accompanied by a shift of the Fourier phase (see Fig. 6.5(b)). This suggests that the relative quantum phase of the wave packets is constant and independent of their temporal separation.

In order to obtain quantitative information on the shift of the temporal separation, the phase-dependent center-of-mass positions of the peak were determined from Gaussian fits to the Fourier amplitude. We observe that the temporal separation varies from ~ 2.9 fs to ~ 2.5 fs. A linear fit reveals a slope of the shift of (0.35 ± 0.04) fs per π CE phase.

From the results presented in this section, we can draw the following qualitative picture: The observation of CE phase dependent spectral interference in the plateau shows that the recollision mechanism is a phase-coherent process even for our solid-state system. The visibility of the interference peaks in the spectrum varies with the CE phase. Absence of interference can be associated with the case of a single slit in time, its presence with a double slit in time. The CEPSI analysis performed on the rescattered photoelectrons confirms the slits-in-time interpretation of the experiment and provides quantitative information on the timing of the slits with attosecond precision. Bursts of high-energy (rescattered) photoelectrons with sub-optical-cycle durations (~ 500 as) are generated by the interaction of the near-field with the tip surface.

In the following, we will investigate the origin of the temporal slits and the observed cut-off modulation with a model that combines both the classical and the quantum aspect of recollision.

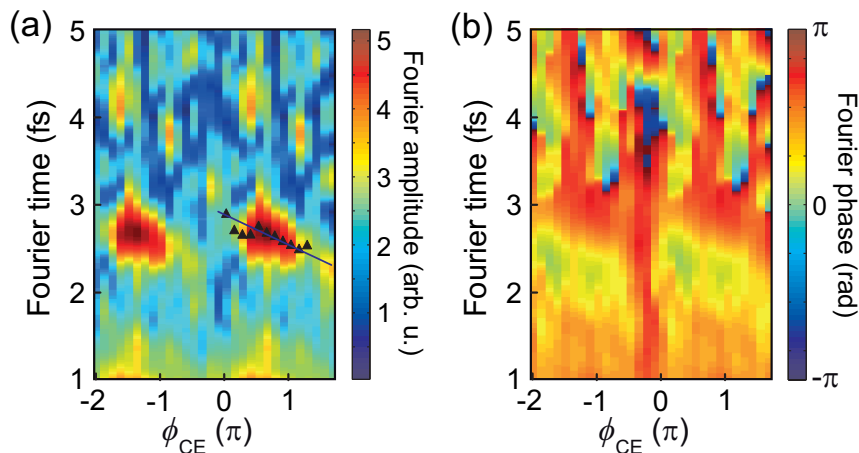


Figure 6.5: Carrier-envelope phase spectral interferometry method. (a) Fourier amplitude and (b) Fourier phase as a function of phase ϕ_{CE} and Fourier time according to the carrier-envelope phase spectral interferometry method. The spectral region under scrutiny is the plateau part of Fig. 6.3. The peak at Fourier time ~ 2.8 fs in (a) corresponds to the temporal spacing of the double-slit scenario ($\phi_{\text{CE}} \sim -1.5\pi$). Also a slight shift of the spacing is evident from the center-of-mass positions of the peak for different carrier-envelope phases (black filled triangles). The line indicates a linear fit to the data with a slope of (0.35 ± 0.04) fs per π carrier-envelope phase. In (b), a phase shift is visible at Fourier time ~ 2.8 fs that follows this slope. Taken from [160].

6.3 Attosecond control of electron motion

In the following, we will apply the extended Three-Step-Model (TSM; see subsection 2.3.4) to the experimental data of the previous sections.

In order to match the experimental data, a cosine-square pulse of duration $\tau = 6.3$ fs (intensity FWHM) and a peak electric field strength of $E_0 = 10.4 \text{ GV m}^{-1}$ has been chosen, following Eqs. 2.41 and 2.50. The central wavelength is $\lambda = 800$ nm. The chosen field strength corresponds to that of the near-field assuming a field enhancement factor of about 6 (compared with the experimental peak field strength of $(1.8 \pm 0.4) \text{ GV m}^{-1}$ in the bare laser focus without tip). The corresponding ponderomotive energy of an electron in the near-field is then 0.86 eV . For simplicity the static electric field of $|E_{\text{DC}}| \sim 0.4 \text{ GV m}^{-1} \ll E_0$ has been neglected in the model, except for the Schottky effect. The work function has been chosen to be the Schottky lowered barrier height of $\phi = 5.2 \text{ eV}$.

Fig. 6.6 illustrates the time dynamics of rescattered electrons in the model for the CE phases 0 and π . We show the tunneling rate (Eq. 2.42) and the final kinetic energy as functions of the time instant of photoemission. As expected for a metal surface, light-induced tunneling (first TSM step) only takes place when the laser electric field is large and negative. Independent of the CE phase, there are maximally two optical cycles that produce rescattered photoelectrons with energies exceeding 5 eV . Two extreme cases are shown in the figure: For $\phi_{\text{CE}} \approx 0$ (“cosine-like pulse”), electrons with an energy $E_{\text{kin}} > 5.5 \text{ eV}$ originate only from a single optical cycle. On the other hand, for $\phi_{\text{CE}} \approx \pi$ (“minus-cosine-like pulse”), trajectories from two optical cycles contribute to almost the whole range of the electron spectrum. High-energy electrons are hence generated either

in one or in two optical cycles. It is the dependence of electron trajectories on the waveform of the field that creates the temporal slits.

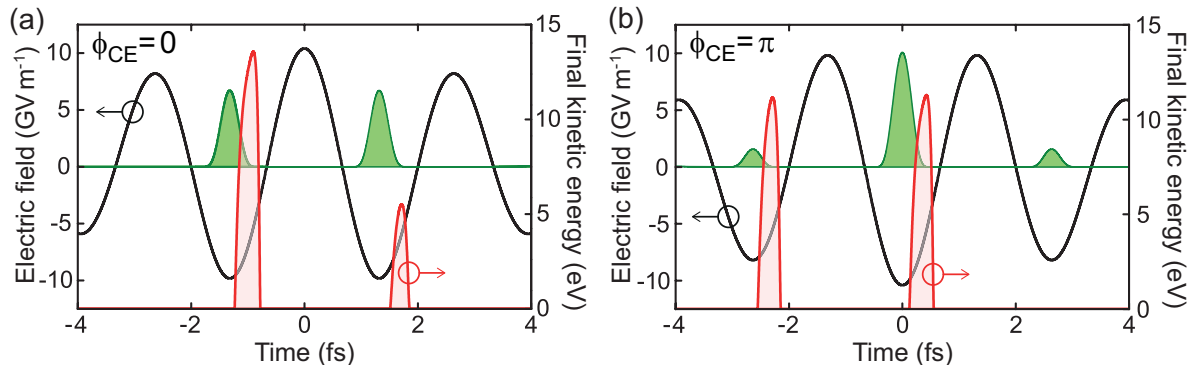


Figure 6.6: Time dynamics of rescattering in the extended Three-Step Model.

(a) Final kinetic energy of a rescattered photoelectron as a function of its emission time t_0 for $\phi_{CE} = 0$ (red curve). Also displayed are the laser electric field (black curve) and the tunneling rate (green curve in the center) that populates the rescattering trajectories. High-energy rescattered electrons can only be generated during one optical cycle. (b) The same for $\phi_{CE} = \pi$. Here two optical cycles are responsible for electrons with high energy. Parameters of the calculation: central wavelength $\lambda = 800$ nm, pulse duration $\tau = 6.3$ fs, peak electric field $E_0 = 10.4$ GV m⁻¹, work function $\phi = 5.2$ eV.

Coherent summation of the individual electron trajectories leading up to a given final energy results in a spectrum with interference structures. Fig. 6.7(a) shows the spectra corresponding to the two extreme cases. The single-slit case ($\phi_{CE} = 0$) shows no interference peaks at energies $E_{\text{kin}} > 5$ eV whereas the double-slit case ($\phi_{CE} = \pi$) does display a fringe pattern with a spacing of the photon energy. On the other hand, we find the highest cut-off energy in the single-slit case ($\phi_{CE} = 0$). Fig. 6.7(b) depicts the plateau part for different CE phases in the same way as the experimental data in Fig. 6.3(b). The TSM thus reproduces and nicely explains the essential features of the experiment, namely the correlated changes in peak visibility and cut-off position.

The experimental results interpreted in the light of the TSM underline the fact that the motion of rescattered electrons is controlled by the waveform of the driving field. Depending on the CE phase, recollision takes place once or twice per pulse. The birth and the motion of electrons can be controlled with a precision of 80 as by changing the carrier-envelope phase, as inferred from the error of the phase offset in the sinusoidal fits to cut-off and visibility (Fig. 6.3). This is closely related to the control mechanism that enables the generation of single isolated attosecond bursts of XUV radiation using recollision [9, 10]. In our experiment, a proper choice of the CE phase enables the generation of single attosecond bursts of (rescattered) photoelectrons.

6.4 Comparison with theory models

In the following, we will take a closer look at the results of the extended TSM and also compare the experimental data with the numerical integration of the time-dependent Schrödinger equation (TDSE).

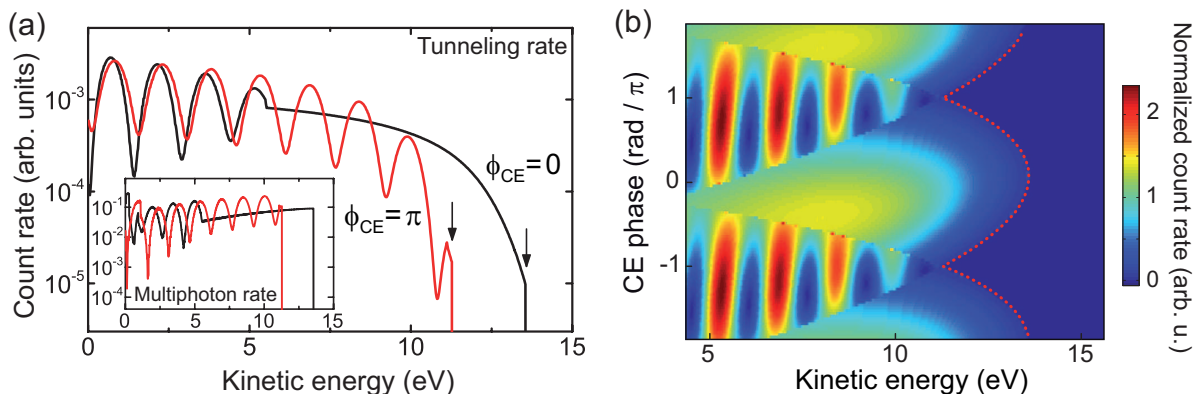


Figure 6.7: Photoelectron spectra calculated with the extended Three-Step Model. (a) Energy spectra calculated from the results of Fig. 6.6 (black curve $\phi_{CE} = 0$, red curve π). The arrows mark the classical cut-off position. The inset shows the same plot assuming a multiphoton photoemission rate instead of the tunneling rate. (b) Color plot of the high-energy part of the spectra as a function of the carrier-envelope phase. The data is handled and displayed in the same way as the experimental data in Fig. 6.3(b). The dotted red curve indicates the classical cut-off position.

Extended Three-Step Model

The color plot in Fig. 6.7(b) allows a direct comparison of the TSM results with the experimental data in Fig. 6.3(b). We find that the peak-to-peak shift of the cut-off position (~ 2.3 eV) is larger than the experimentally determined shift (~ 1.3 eV). Moreover, sharp borders are visible that separate regions where one and where two optical cycles contribute. In a fully quantum mechanical calculation these borders are smoothed out. Despite the simplicity of the model, the agreement with the experimental data is surprisingly good.

In the first step, the TSM assumes tunneling as photoemission mechanism. Tunneling or, more exactly, a tunneling emission rate is not something one *a priori* expects in the parameter range of our experiment. At an electric field strength of ~ 10 GV m^{-1} , the Keldysh parameter γ is about 2. This places our experiment in the transition regime between multiphoton and tunneling photoemission. It has been predicted, however, that with such a Keldysh parameter nonadiabatic tunneling can occur [60]. In this case, the contribution from tunneling to the whole photoemission process is non-negligibly large. Models assuming tunneling ionization at $\gamma \sim 1$ have been successfully applied to experiments, for example to a time-resolved study of electron tunneling [13] and to ionization dynamics inside a solid-state system [172]. We tried other emission rates for the first step of the TSM, namely the nonadiabatic tunneling rate [60] and a multiphoton rate assuming 4-photon-absorption (Eq. 2.2). In the inset of Fig. 6.7(a) we display the multiphoton result. For both rates the overall slope of the spectra does not agree with the experiment, but the general features such as cut-off position and the presence or absence of interference are retained. This shows that the propagation effects after the emission step predominantly determine the outcome of the process. We emphasize therefore that our results are not necessarily a proof for the tunneling process but they seem to favor it. Moreover, we note here that the separation of the emission process into three steps is

not straightforward due to the small classical excursion length α of the electron in the laser field of about 3 \AA [173]. However, the agreement between experimental data and model results seems to justify this treatment. The Quantum Orbit Theory for few-cycle pulses (cf. Section 2.3, see also [76]) is capable of lifting the problems described here, but this is beyond the scope of this thesis and will be part of future work.

Integration of the time-dependent Schrödinger equation

A numerical integration of the time-dependent Schrödinger equation provides an exact quantum mechanical model. It was used to model a photoelectron spectrum with a plateau already in the previous chapter. Here we investigate the CE phase effects.

The parameters of the integration of the TDSE have been chosen in order to match the plateau part of the experimental spectra. The peak electric field is $E_0 = 9.9 \text{ GV m}^{-1}$. This corresponds to a field enhancement of about 6 compared to the peak electric field of $(1.8 \pm 0.4) \text{ GV m}^{-1}$ that is expected in the focal spot without tip. The static electric field strength is -0.4 GV m^{-1} . The work function is chosen as $\phi = 6 \text{ eV}$. This results in an effective barrier height of 5.2 eV due to the Schottky effect. The pulse with a Gaussian envelope has a duration of 5.5 fs (intensity FWHM) at a center wavelength of 800 nm . In the integration procedure the step size of the spatial grid is 0.04 \AA and the time step is 7.2 as .

Fig. 6.8 shows the results of the integration of the TDSE. The displayed plateau part agrees well with the experimental data shown in the same figure. In particular, the agreement of the CE phase effects with the experimental data around $E_{\text{kin}} \sim 11 \text{ eV}$ is remarkable. Moreover, the modulation of the cut-off position and the peak visibility (Fig. 6.8(c)) shows the same tendencies as observed in the experiment. The cut-off position varies between 12.0 and 12.7 eV . The latter value is reached at a CE phase of $(-0.216 \pm 0.005)\pi$. The CE phase offset of the experimental data (see Section 6.1) has been calibrated so that experimental and theoretical phase coincide where the cut-off position reaches the maximum value. The electric field in the experiment is then cosine-like ($\phi_{\text{CE}} \approx 0$) for a CE phase offset of $(0.00 \pm 0.05)\pi$. The cut-off variation (peak-to-peak shift of $\sim 0.7 \text{ eV}$) is less pronounced than in the experimental data (peak-to-peak shift of $\sim 1.3 \text{ eV}$). This is mainly caused by the evaluation procedure of the cut-off position in the TDSE data. The peak structure is very pronounced and had to be strongly suppressed by a smoothing algorithm in order to be able to determine the cut-off.

The peak visibility in the plateau is much higher than observed in the experiment. This can be attributed to the resolution of the spectrometer and the treatment of the experimental data. Hard smoothing had to be applied to the data in order to suppress noise. Moreover, we ignored occupied electronic states located at lower energies than the Fermi energy in our calculation. Their contribution to the final spectrum should cause a significant decrease in peak visibility. A more elaborate time-dependent density functional theory simulation (see subsections 2.4.2 and 5.1.2) with CE phase resolution will be part of future work.

Fig. 6.8(d) shows the time evolution of the ground state population in the simulation. The loss of population and hence photoemission is strongly correlated with times when the laser field is large and negative. A similar behavior is found with the TDDFT simulation (see subsection 5.1.2, Fig. 5.6).

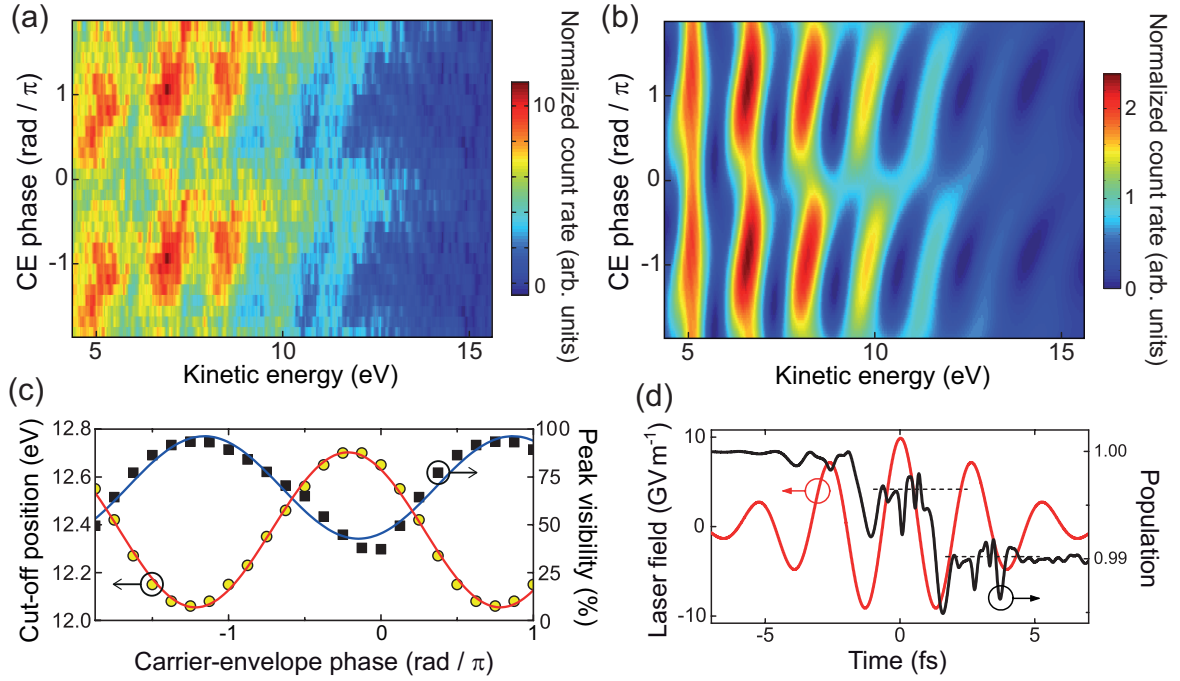


Figure 6.8: Results of the integration of the time-dependent Schrödinger equation. (a) Color plot of the plateau part of the experimental spectra as a function of the CE phase, taken from Fig. 6.3(b). (b) Simulated spectra displayed in the same way as the experimental data. (c) Cut-off position (circles) and peak visibility (squares) as a function of CE phase. The solid curves represent sinusoidal fits. (d) Population of the ground state in the simulation as a function of time (black curve). Photoemission is taking place during the two central laser cycles when the laser electric field (red curve) is large and negative. The dashed horizontal lines indicate the average population after each laser cycle.

Carrier-envelope phase spectral interferometry analysis

The CEPSI method can also be applied to the theory results and assist in the evaluation of their performance [160]. Fig. 6.9 displays the results of the analysis on the extended TSM (part (a)) and the TDSE model (part (b)), with the same region of interest as for the experimental data (see Fig. 6.5). The TSM nicely reproduces the single-slit vs. double-slit behavior observed in the analysis of the experimental data. The temporal shift of the Fourier peak at ~ 2.8 fs with the CE phase is not found in the TSM calculation. The second model, the TDSE, nicely captures the latter feature both in amplitude and phase. On the other hand, the slit behavior is much less pronounced compared to the experimental data. This is due to the fact that the TDSE only takes a single initial state at the Fermi energy E_F into account; occupied electronic states below E_F are ignored.

The TSM shows two major shortcomings compared to the TDSE model. First, it neglects nonadiabatic electron dynamics: Tunneling photoemission in the first TSM step quasistatically follows the laser electric field. At a Keldysh parameter of $\gamma \sim 2$, however, nonadiabatic effects are expected. Second, the image-force potential is absent in the TSM, which is explicitly taken into account in the TDSE model. This suggests that it is possible to uncover effects arising from the shape of the surface potential with the help of CEPSI.

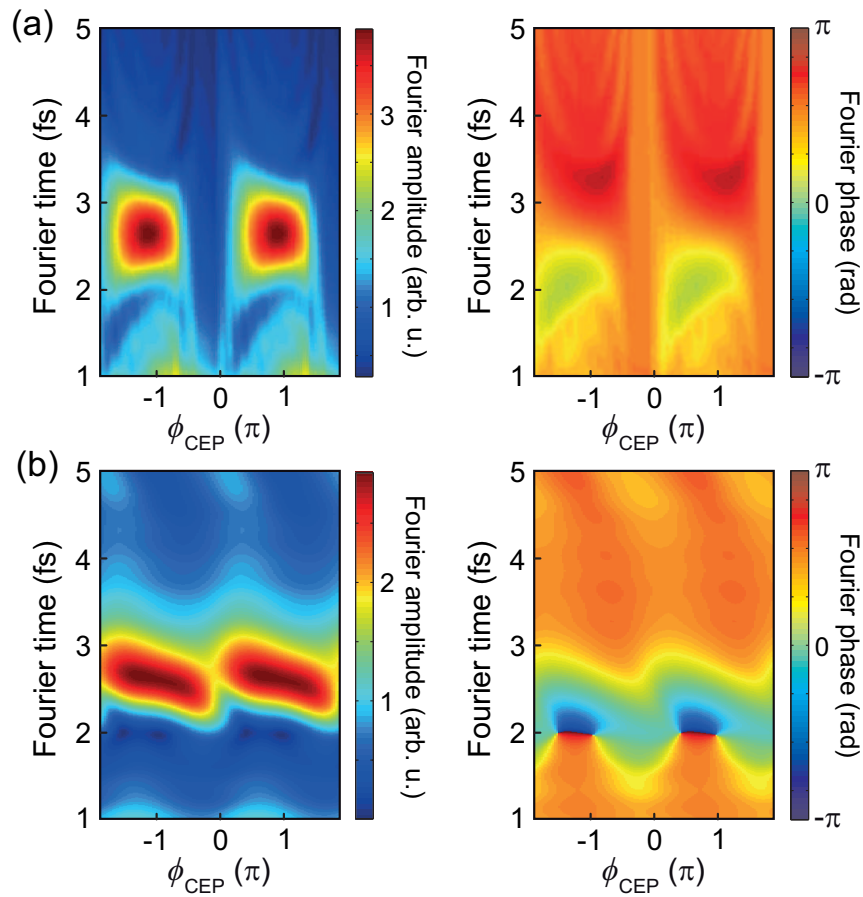


Figure 6.9: Spectral interferometry analysis of theory results. (a) Extended Three-Step Model (Fig. 6.7). (b) Integration of the Schrödinger equation (Fig. 6.8). Taken from [160].

7 Conclusion and outlook

This thesis presented the first experimental and theoretical investigation of strong-field effects, recollision and attosecond physics in strong-field photoemission from a metal. Crucial to the success of the experiment was the ability to perform photocurrent measurements with spectral resolution and the possibility to precisely control the waveform of the optical electric field of ultrashort laser pulses. Under the influence of such a field, the motion of photoemitted electrons can be steered with attosecond precision, leading to a subsequent interaction with the metal surface. The temporal dynamics of the electrons leave characteristic footprints in the energy domain that are accessible by measuring photoelectron spectra.

In the experiment, a sharp metal nanotip is irradiated by near-infrared 6-fs laser pulses from a Ti:sapphire laser oscillator. The incident laser field excites a strongly localized and enhanced optical near-field at the tip's apex. Effective intensities on the order of $10^{13} \text{ W cm}^{-2}$ are reached at the tip surface without damage to the material. This enables studies of the strong-field regime where the force exerted by the light field on an electron in the metal is close to the energy binding it. Photoelectron spectra reveal that at these intensities above-threshold photoemission takes place: Spectral peaks spaced by the photon energy appear that correspond to the absorption of a number of photons from the laser field. With increasing laser intensity the peak at lowest energy starts to disappear and the whole spectral structure shifts towards lower energy. This is a clear signature of strong-field effects: Photoelectrons strongly quiver in the laser field and their mean kinetic energy transiently acquired during this motion is on the order of the photon energy. In consequence, the laser field cannot be regarded as a small perturbation of the system anymore, but strongly drives electron motion.

Furthermore, a plateau structure is found in photoelectron spectra where the count rate stays constant with increasing energy – a hallmark of electron rescattering and recollision, here observed for the first time at a metal surface. A classical description of light-matter interaction is sufficient: An emitted electron propagates in the optical near-field and is eventually driven back to the surface and recollides with it. Elastic (re)scattering at the surface leads to high kinetic energies, much higher than without the additional interaction with the surface. All this takes place on the attosecond time scale within a fraction of the duration of an optical cycle. A semiclassical model based on the notion of field-driven electron motion as well as fully quantum mechanical models provide a satisfying explanation of the observed phenomena including their dependence on laser intensity and static electric field at the tip.

Rescattered electrons are extremely sensitive to the spatial and temporal structure of the optical near-field at the tip's apex. This fact was exploited to measure the strength of the near-field at tungsten and gold tips of different size with a resolution of 1 nm. Regardless of the material choice, the magnitude of field enhancement strongly increases

with decreasing tip size. This suggests that the geometry of the tip predominantly determines the properties of the near-field, in good agreement with numerical simulations of the system using classical electrodynamics.

The attosecond dynamics of the recollision process was explored with the help of carrier-envelope phase stable laser pulses. Depending on the choice of the phase, high-energy electrons are observed or not; here the laser electric field effectively creates an ultrafast switching mechanism. Moreover, the contrast of the spectral peaks in the rescattering plateau is strongly modulated with the carrier-envelope phase. Photoelectron spectra and the peak structure can be regarded as quantum mechanical interferograms of different electron wave packets and hence contain encoded information about the time dynamics of recollision. The absence of interference peaks indicates that the waveform of the laser pulse creates a scenario where only one wave packet from one optical cycle contributes to the plateau. The presence of interference, on the other hand, represents the case of two wave packets generated in subsequent cycles. The latter can be interpreted as double-slit experiment in the time domain, causing interference in the energy domain. These findings along with a fair agreement with theory models show that the recollision process at a metal surface can be coherently controlled by the waveform of the driving field with attosecond precision.

Outlook

Future work will include a deeper investigation of the fundamental physics involved in the photoemission mechanisms and the recollision process. Furthermore, tip-based electron emission bears the prospect of a wide variety of applications detailed below.

Strong-field photoemission at mid-infrared wavelengths. Mid-infrared laser sources driving photoemission from a tip opens up several new possibilities. First, we expect to enter more deeply into the tunneling regime of photoemission than with the present Ti:sapphire laser source. The Keldysh parameter (Eq. 2.4) that defines the photoemission regime scales inversely proportional to the laser wavelength. Second, the excursion length of an electron undergoing rescattering and the mean quiver energy of an electron in the laser field increase considerably with the driving wavelength. Third, the excursion length can be so large so that the electron leaves the region of the strongly localized near-field within a fraction of the optical cycle. Its quiver motion in the field is then strongly suppressed [174], resulting in the absence of recollision and sub-optical-cycle emission of direct electrons.

For this purpose two new laser sources at mid-infrared wavelengths are available in our group. A laser system based on noncollinear optical parametric amplification and difference frequency generation produces sub-two-cycle laser pulses at a tunable center wavelength of $\sim 1.8 \mu\text{m}$ with a repetition rate of 100 kHz [175]. The laser pulses with pulse energies up to 145 nJ are passively CE phase stable and enable phase-sensitive photoemission measurements with nanotips in the tunneling regime. A fiber laser system generates 23-fs pulses at 1700 nm center wavelength, corresponding to 4.1 optical cycles [176]. The low maximum pulse energy of ~ 2 nJ is mitigated by a repetition rate of 100 MHz.

Waveform control beyond the carrier-envelope phase. An alternative to the carrier-envelope phase stable laser pulses is a bichromatic laser field. The simplest implementation of such a field is the combination of a fundamental laser beam with its second harmonic (“ $\omega+2\omega$ pulse”). Varying the relative phase $\phi_{\omega-2\omega}$ of the two fields can result in highly asymmetric waveforms while conserving the average light intensity. $\omega+2\omega$ pulses are expected to induce high phase contrast in the total photoemission current from a tip, which will enable more insight into the photoemission mechanism. A corresponding experiment was already carried out with atomic gases [177] where the total photocurrent was found to be strongly suppressed with an appropriate choice of $\phi_{\omega-2\omega}$. In our case, an implementation of such an experiment is currently underway using mid-infrared laser sources. Full control over optical fields and their waveform can be provided by an optical field synthesizer [178]. Pulses with arbitrary shapes and durations of less than an optical cycle can be generated in a well-controlled fashion. It will be insightful to explore the dynamics of nanotip photoemission and electron recollision in these pulses. Single isolated attosecond bursts of direct electrons from a tip are feasible with the synthesizer.

Carrier-envelope phase and offset frequency stabilization. Our experiment can function as a sensing device for the carrier-envelope phase. It is also feasible to measure and stabilize the carrier-envelope offset frequency f_{CEO} of a train of few-cycle pulses with the help of tip photoemission. f_{CEO} is given by the pulse-to-pulse carrier-envelope phase slip over time. This application was discussed in detail in [119]: The main challenge for such an application is the low electron count rate. At a pulse energy of 240 nJ, on average only about one electron per laser pulse is emitted from the tip and only 10^{-2} undergo rescattering. With the current detectors in the setup, the detection efficiency is 0.1 at best, resulting in 10^{-3} detected electrons per pulse. However, in order to reach a signal-to-noise ratio of 30 dB at a frequency bandwidth of 100 kHz (typical fluctuation of f_{CEO} in an oscillator), a signal of about one electron per pulse is required under the assumption of shot-noise limited photoelectron statistics. More efficient detection and the use of an array of nanoscale emitters (see, e.g. [179]) might lift the current limitations. Moreover, higher photoelectron currents can be obtained from a blunt tip at the cost of efficient field enhancement. For example, a stable photocurrent of ~ 2000 electrons per pulse was achieved from a tungsten tip with a pulse energy of 2.3 nJ. A tip material with higher field enhancement such as aluminum might compensate for the larger tip size.

With such a sensor device, carrier-envelope phase and offset frequency detection would be possible with much smaller laser pulse energy (~ 200 pJ) than with a conventional all-optical f -to- $2f$ interferometer (~ 1 nJ). The setup consisting of a nanotip, a simplified version of a retarding field spectrometer and an electron multiplier could be miniaturized and accommodated in a small vacuum glass cell of 1 cm^3 volume.

Nanoscale field sensor. Photoemission from a nanotip can be used to probe the optical near-field at the tip. As a first demonstration, we measured the strength of the near-field within a distance of ~ 1 nm for different tips. This method can be extended towards a full tomographic reconstruction of the near-field using laser pulses of different wavelengths and intensities and an electron spectrometer with angular resolution. The pronounced sensitivity of rescattering to the phase of the near-field can be used

to determine the phase shift of the near-field with respect to the incident laser field. A comparison of phase-resolved spectra from a nanotip and an atomic gas should enable such a measurement.

Nanotip photoemission can not only sense the near-field, but also the incident field inside the laser focal spot. The nanometer-sized tip apex can be used to scan and measure the local electric field in amplitude (scaling of the photocurrent with intensity) and phase (carrier-envelope phase sensitivity). This enables a complete three-dimensional characterization of the optical field in a focused broadband Gaussian beam, including the Gouy phase shift.

Attosecond field effect transistor. The field-controlled switching mechanism demonstrated with high-energy electrons can be used to implement a proof-of-principle attosecond field effect transistor. In such a device, the electric field of light directly switches electron currents between two electrodes on an attosecond time scale. Conduction electrons typically move with velocities on the order of 1 nm per fs. Hence if electronics shall be driven at optical (petahertz) frequencies (“lightwave electronics”, in analogy to semiconductor electronics involving microwave frequencies), nanostructured electrodes are required. We plan to build such a device using two tip electrodes facing each other at a distance of less than 10 nm. Illumination of the tips with carrier-envelope phase stable pulses should result in a net current in the gap between the tips. We expect that the phase will determine magnitude and direction of this current. The proposed device bears much similarity to tube technology that preceded the transistor.

Time-resolved imaging of matter. Electrons that undergo rescattering interact again with the parent matter, the metal surface. It is feasible that these electrons can be used to image the structural dynamics of the surface on an attosecond time scale. A time-resolved low-energy electron diffraction method might result in the spirit of high-harmonic spectroscopy of molecules [180]. Furthermore, we expect to be sensitive to sub-fs solid-state effects such as the formation of a hole upon photoemission of an electron.

Bibliography

- [1] Bohr, N. On the constitution of atoms and molecules, Part I. *Philosophical Magazine and Journal of Science* **26**, 1–25 (1913).
- [2] Corkum, P. B. & Krausz, F. Attosecond science. *Nat. Phys.* **3**, 381–387 (2007).
- [3] Krausz, F. & Ivanov, M. Attosecond physics. *Rev. Mod. Phys.* **81**, 163–234 (2009).
- [4] Corkum, P. B. Plasma perspective on strong field multiphoton ionization. *Phys. Rev. Lett.* **71**, 1994–1997 (1993).
- [5] Lewenstein, M., Balcou, P., Ivanov, M. Y., L’Huillier, A. & Corkum, P. B. Theory of high-harmonic generation by low-frequency laser fields. *Phys. Rev. A* **49**, 2117–2132 (1994).
- [6] McPherson, A., Gibson, G., Jara, H., Johann, U., Luk, T. S., McIntyre, I. A., Boyer, K. & Rhodes, C. K. Studies of multiphoton production of vacuum-ultraviolet radiation in the rare gases. *J. Opt. Soc. Am. B* **4**, 595–601 (1987).
- [7] Li, X. F., L’Huillier, A., Ferray, M., Lompré, L. A. & Mainfray, G. Multiple-harmonic generation in rare gases at high laser intensity. *Phys. Rev. A* **39**, 5751–5761 (1989).
- [8] Holzwarth, R., Udem, T., Hänsch, T. W., Knight, J. C., Wadsworth, W. J. & Russell, P. S. J. Optical frequency synthesizer for precision spectroscopy. *Phys. Rev. Lett.* **85**, 2264–2267 (2000).
- [9] Baltuška, A., Udem, T., Uiberacker, M., Hentschel, M., Goulielmakis, E., Gohle, C., Holzwarth, R., Yakovlev, V. S., Scrinzi, A., Hänsch, T. W. & Krausz, F. Attosecond control of electronic processes by intense light fields. *Nature* **421**, 611–616 (2003).
- [10] Kienberger, R., Goulielmakis, E., Uiberacker, M., Baltuška, A., Yakovlev, V., Bammer, F., Scrinzi, A., Westerwalbesloh, T., Kleineberg, U., Heinzmann, U., Drescher, M. & Krausz, F. Atomic transient recorder. *Nature* **427**, 817–821 (2004).
- [11] Sansone, G., Benedetti, E., Calegari, F., Vozzi, C., Avaldi, L., Flammini, R., Poletto, L., Villoresi, P., Altucci, C., Velotta, R., Stagira, S., Silvestri, S. D. & Nisoli, M. Isolated single-cycle attosecond pulses. *Science* **314**, 443–446 (2006).
- [12] Zhao, K., Zhang, Q., Chini, M., Wu, Y., Wang, X. & Chang, Z. Tailoring a 67 attosecond pulse through advantageous phase-mismatch. *Optics Lett.* **37**, 3891–3893 (2012).

- [13] Uiberacker, M., Uphues, T., Schultze, M., Verhoef, A. J., Yakovlev, V., Kling, M. F., Rauschenberger, J., Kabachnik, N. M., Schroder, H., Lezius, M., Kompa, K. L., Muller, H. G., Vrakking, M. J. J., Hendel, S., Kleineberg, U., Heinzmann, U., Drescher, M. & Krausz, F. Attosecond real-time observation of electron tunnelling in atoms. *Nature* **446**, 627–632 (2007).
- [14] Cavalieri, A. L., Müller, N., Uphues, T., Yakovlev, V. S., Baltuška, A., Horvath, B., Schmidt, B., Blümel, L., Holzwarth, R., Hendel, S., Drescher, M., Kleineberg, U., Echenique, P. M., Kienberger, R., Krausz, F. & Heinzmann, U. Attosecond spectroscopy in condensed matter. *Nature* **449**, 1029–1032 (2007).
- [15] Schultze, M., Fieß, M., Karpowicz, N., Gagnon, J., Korbman, M., Hofstetter, M., Neppl, S., Cavalieri, A. L., Komninos, Y., Mercouris, T., Nicolaides, C. A., Pazourek, R., Nagele, S., Feist, J., Burgdörfer, J., Azzeer, A. M., Ernstorfer, R., Kienberger, R., Kleineberg, U., Goulielmakis, E., Krausz, F. & Yakovlev, V. S. Delay in photoemission. *Science* **328**, 1658–1662 (2010).
- [16] Paulus, G. G., Nicklich, W., Xu, H., Lambropoulos, P. & Walther, H. Plateau in above threshold ionization spectra. *Phys. Rev. Lett.* **72**, 2851–2854 (1994).
- [17] Paulus, G. G., Becker, W., Nicklich, W. & Walther, H. Rescattering effects in above-threshold ionization: a classical model. *J. Phys. B: At. Mol. Opt. Phys.* **27**, L703–L708 (1994).
- [18] Shafir, D., Soifer, H., Bruner, B. D., Dagan, M., Mairesse, Y., Patchkovskii, S., Ivanov, M. Y., Smirnova, O. & Dudovich, N. Resolving the time when an electron exits a tunnelling barrier. *Nature* **485**, 343–346 (2012).
- [19] Müller, E. W. Versuche zur Theorie der Elektronenemission unter der Einwirkung hoher Feldstärken. *Zeitschrift für technische Physik* **37**, 838–842 (1936).
- [20] Müller, E. W. Das Feldionenmikroskop. *Zeitschrift für Physik* **131**, 136–142 (1951).
- [21] Müller, E. W. & Bahadur, K. Field ionization of gases at a metal surface and the resolution of the field ion microscope. *Phys. Rev.* **102**, 624–631 (1956).
- [22] Binnig, G., Rohrer, H., Gerber, C. & Weibel, E. Surface studies by scanning tunneling microscopy. *Phys. Rev. Lett.* **49**, 57–61 (1982).
- [23] Binnig, G., Quate, C. F. & Gerber, C. Atomic force microscope. *Phys. Rev. Lett.* **56**, 930–933 (1986).
- [24] Heinzlmann, H. & Pohl, D. Scanning near-field optical microscopy. *Appl. Phys. A* **59**, 89–101 (1994).
- [25] Novotny, L. & Hecht, B. *Principles of Nano-Optics* (Cambridge University Press, 2006).

- [26] Merschdorf, M., Pfeiffer, W., Thon, A. & Gerber, G. Hot electron tunneling in femtosecond laser-assisted scanning tunneling microscopy. *Appl. Phys. Lett.* **81**, 286–288 (2002).
- [27] Hommelhoff, P., Sortais, Y., Aghajani-Talesh, A. & Kasevich, M. A. Field emission tip as a nanometer source of free electron femtosecond pulses. *Phys. Rev. Lett.* **96**, 077401 (2006).
- [28] Hommelhoff, P., Kealhofer, C. & Kasevich, M. A. Ultrafast electron pulses from a tungsten tip triggered by low-power femtosecond laser pulses. *Phys. Rev. Lett.* **97**, 247402 (2006).
- [29] Hommelhoff, P., Kealhofer, C. & Kasevich, M. A. Femtosecond laser meets field emission tip – a sensor for the carrier envelope phase? In *Proceedings of the 2006 IEEE International Frequency Control Symposium and Expositions, Vols 1 and 2*, 470–474 (2006).
- [30] Ropers, C., Solli, D. R., Schulz, C. P., Lienau, C. & Elsaesser, T. Localized multiphoton emission of femtosecond electron pulses from metal nanotips. *Phys. Rev. Lett.* **98**, 043907 (2007).
- [31] Caprez, A., Barwick, B. & Batelaan, H. Macroscopic test of the Aharonov-Bohm effect. *Phys. Rev. Lett.* **99**, 210401 (2007).
- [32] Schenk, M., Krüger, M. & Hommelhoff, P. Strong-field above-threshold photoemission from sharp metal tips. *Phys. Rev. Lett.* **105**, 257601 (2010).
- [33] Krüger, M., Schenk, M. & Hommelhoff, P. Attosecond control of electrons emitted from a nanoscale metal tip. *Nature* **475**, 78–81 (2011).
- [34] Wachter, G., Lemell, C., Burgdörfer, J., Schenk, M., Krüger, M. & Hommelhoff, P. Electron rescattering at metal nanotips induced by ultrashort laser pulses. *Phys. Rev. B* **86**, 035402 (2012).
- [35] Krüger, M., Schenk, M., Förster, M. & Hommelhoff, P. Attosecond physics in photoemission from a metal nanotip. *J. Phys. B: At. Mol. Opt. Phys.* **45**, 074006 (2012).
- [36] Krüger, M., Schenk, M., Hommelhoff, P., Wachter, G., Lemell, C. & Burgdörfer, J. Interaction of ultrashort laser pulses with metal nanotips: a model system for strong-field phenomena. *New J. Phys.* **14**, 085019 (2012).
- [37] Thomas, S., Krüger, M., Förster, M., Schenk, M. & Hommelhoff, P. Probing of optical near-fields by electron rescattering on the 1 nm scale. *Nano Lett.* **13**, 4790–4794 (2013).
- [38] Schenk, M., Krüger, M. & Hommelhoff, P. Carrier-envelope phase dependent photoemission from a nanometric metal tip. In *Frequency Control and the European Frequency and Time Forum (FCS), 2011 Joint Conference of the IEEE International*, 404–406 (2011).

- [39] Hertz, H. Ueber einen Einfluss des ultravioletten Lichtes auf die elektrische Entladung. *Annalen der Physik* **267**, 983–1000 (1887).
- [40] Einstein, A. Über einen die Erzeugung und Verwandlung des Lichtes betreffenden heuristischen Gesichtspunkt. *Annalen der Physik* **322**, 132–148 (1905).
- [41] Kaiser, W. & Garrett, C. G. B. Two-photon excitation in CaF_2 : Eu^{2+} . *Phys. Rev. Lett.* **7**, 229–231 (1961).
- [42] Sonnenberg, H., Heffner, H. & Spicer, W. Two-photon photoelectric effect in Cs_3Sb^1 . *Appl. Phys. Lett.* **5**, 95–96 (1964).
- [43] Göppert-Mayer, M. Über Elementarakte mit zwei Quantensprüngen. *Annalen der Physik* **9**, 273–294 (1931).
- [44] Faisal, F. H. M. *Theory of multiphoton processes* (Plenum Press, New York, 1987).
- [45] Keldysh, L. V. Ionization in the field of a strong electromagnetic wave. *Sov. Phys. JETP* **20**, 1307–1314 (1965).
- [46] Bunkin, F. V. & Fedorov, M. V. Cold emission of electrons from the surface of a metal in a strong radiation field. *Sov. Phys. JETP* **21**, 896–899 (1965).
- [47] Reiss, H. R. Limits on tunneling theories of strong-field ionization. *Phys. Rev. Lett.* **101**, 043002 (2008).
- [48] Augst, S., Meyerhofer, D. D., Strickland, D. & Chint, S. L. Laser ionization of noble gases by Coulomb-barrier suppression. *J. Opt. Soc. Am. B* **8**, 858–867 (1991).
- [49] Perelomov, A. M., Popov, V. S. & Terent'ev, M. V. Ionization of atoms in an alternating electrical field. *Sov. Phys. JETP* **23**, 924–928 (1966).
- [50] Perelomov, A. M., Popov, V. S. & Terent'ev, M. V. Ionization of atoms in an alternating electrical field: II. *Sov. Phys. JETP* **24**, 207–217 (1967).
- [51] Tóth, C., Farkas, G. & Vodopyanov, K. L. Laser-induced electron emission from an Au surface irradiated by single picosecond pulses at $\lambda = 2.94 \mu\text{m}$. The intermediate region between multiphoton and tunneling effect. *Appl. Phys. B* **53**, 221–225 (1991).
- [52] Fowler, R. H. & Nordheim, L. Electron emission in intense electric fields. *Royal Society of London Proceedings Series A* **119**, 173–181 (1928).
- [53] Oppenheimer, J. R. Three notes on the quantum theory of aperiodic effects. *Phys. Rev.* **31**, 66–81 (1928).
- [54] Landau, L. D. & Lifshitz, E. M. *Quantum Mechanics (non-relativistic theory)*, 3rd revised edition (Pergamon Press, Oxford, 1977).

- [55] Agostini, P., Fabre, F., Mainfray, G., Petite, G. & Rahman, N. K. Free-free transitions following 6-photon ionization of xenon atoms. *Phys. Rev. Lett.* **42**, 1127–1130 (1979).
- [56] Luan, S., Hippler, R., Schwier, H. & Lutz, H. O. Electron-emission from polycrystalline copper surfaces by multi-photon absorption. *Europhys. Lett.* **9**, 489–494 (1989).
- [57] Muller, H. G., van Linden van den Heuvell, H. B., Agostini, P., Petite, G., Antonetti, A., Franco, M. & Migus, A. Multiphoton ionization of xenon with 100-fs laser-pulses. *Phys. Rev. Lett.* **60**, 565–568 (1988).
- [58] Bucksbaum, P. H., Freeman, R. R., Bashkansky, M. & McIlrath, T. J. Role of the ponderomotive potential in above-threshold ionization. *J. Opt. Soc. Am. B* **4**, 760–764 (1987).
- [59] Jönsson, L. Energy shifts due to the ponderomotive potential. *J. Opt. Soc. Am. B* **4**, 1422–1425 (1987).
- [60] Yudin, G. L. & Ivanov, M. Y. Nonadiabatic tunnel ionization: Looking inside a laser cycle. *Phys. Rev. A* **64**, 013409 (2001).
- [61] Bormann, R., Gulde, M., Weismann, A., Yalunin, S. V. & Ropers, C. Tip-enhanced strong-field photoemission. *Phys. Rev. Lett.* **105**, 147601 (2010).
- [62] Yalunin, S. V., Gulde, M. & Ropers, C. Strong-field photoemission from surfaces: Theoretical approaches. *Phys. Rev. B* **84**, 195426 (2011).
- [63] Eberly, J. H., Javanainen, J. & Rzażewski, K. Above-threshold ionization. *Phys. Rep.* **204**, 331–383 (1991).
- [64] Lee, M. J. G. Field emission of hot electrons from tungsten. *Phys. Rev. Lett.* **30**, 1193–1196 (1973).
- [65] Rethfeld, B., Kaiser, A., Vicanek, M. & Simon, G. Ultrafast dynamics of nonequilibrium electrons in metals under femtosecond laser irradiation. *Phys. Rev. B* **65**, 214303 (2002).
- [66] Yanagisawa, H., Hengsberger, M., Leuenberger, D., Klöckner, M., Hafner, C., Greber, T. & Osterwalder, J. Energy distribution curves of ultrafast laser-induced field emission and their implications for electron dynamics. *Phys. Rev. Lett.* **107**, 087601 (2011).
- [67] Kealhofer, C., Foreman, S. M., Gerlich, S. & Kasevich, M. A. Ultrafast laser-triggered emission from hafnium carbide tips. *Phys. Rev. B* **86**, 035405 (2012).
- [68] Fittinghoff, D. N., Bolton, P. R., Chang, B. & Kulander, K. C. Observation of nonsequential double ionization of helium with optical tunneling. *Phys. Rev. Lett.* **69**, 2642–2645 (1992).

- [69] Paulus, G. G., Lindner, F., Walther, H. & Milošević, D. Phase-controlled single-cycle strong-field photoionization. *Physica Scripta* **T110**, 120–125 (2004).
- [70] Kuchiev, M. Y. Atomic antenna. *JETP Lett.* **45**, 404–406 (1987).
- [71] van Linden, van den Heuvel, H. B. & Muller, H. G. Limiting cases of excess-photon ionization. In Smith, S. J. & Knight, P. L. (eds.) *Studies in Modern Optics No 8, Multiphoton Processes*, 25–34 (Cambridge University Press, Cambridge, 1988).
- [72] Gallagher, T. F. Above-threshold ionization in low-frequency limit. *Phys. Rev. Lett.* **61**, 2304–2307 (1988).
- [73] Corkum, P. B., Burnett, N. H. & Brunel, F. Above-threshold ionization in the long-wavelength limit. *Phys. Rev. Lett.* **62**, 1259–1262 (1989).
- [74] Ammosov, M., Delone, N. & Krainov, V. Tunnel ionization of complex atoms and atomic ions in an electromagnetic field. *Sov. Phys. JETP* **64**, 1191–1194 (1986).
- [75] Becker, W., Grasbon, F., Kopold, R., Milošević, D., Paulus, G. & Walther, H. Above-threshold ionization: From classical features to quantum effects. In Beder-son, B. & Walther, H. (eds.) *Advances in Atomic, Molecular, and Optical Physics*, vol. 48, 35–98 (Academic Press, 2002).
- [76] Milošević, D. B., Paulus, G. G., Bauer, D. & Becker, W. Above-threshold ionization by few-cycle pulses. *J. Phys. B: At. Mol. Opt. Phys.* **39**, R203–R262 (2006).
- [77] Becker, W., McIver, J. K. & Confer, M. Total multiphoton-ionization rates for an extremely short-ranged potential. *Phys. Rev. A* **40**, 6904–6912 (1989).
- [78] Gribakin, G. F. & Kuchiev, M. Y. Multiphoton detachment of electrons from negative ions. *Phys. Rev. A* **55**, 3760–3771 (1997).
- [79] Bergues, B., Ansari, Z., Hanstorp, D. & Kiyani, I. Y. Photodetachment in a strong laser field: An experimental test of Keldysh-like theories. *Phys. Rev. A* **75**, 063415 (2007).
- [80] Faisal, F. H. M., Kamiński, J. Z. & Saczuk, E. Photoemission and high-order harmonic generation from solid surfaces in intense laser fields. *Phys. Rev. A* **72**, 023412 (2005).
- [81] Faisal, F. H. M. Multiple absorption of laser photons by atoms. *J. Phys. B: At. Mol. Phys.* **6**, L89–L93 (1973).
- [82] Reiss, H. R. Effect of an intense electromagnetic field on a weakly bound system. *Phys. Rev. A* **22**, 1786–1813 (1980).
- [83] Volkov, D. M. Über eine Klasse von Lösungen der Diracschen Gleichung. *Zeitschrift für Physik* **94**, 250–260 (1935).
- [84] Kopold, R. *Atomare Ionisationsdynamik in starken Laserfeldern*. Ph.D. thesis, Technische Universität München (2001).

- [85] Becker, W., Lohr, A. & Kleber, M. Effects of rescattering on above-threshold ionization. *J. Phys. B: At. Mol. Opt. Phys.* **27**, L325–L332 (1994).
- [86] Salières, P., Carré, B., Le Déroff, L., Grasbon, F., Paulus, G. G., Walther, H., Kopold, R., Becker, W., Milošević, D. B., Sanpera, A. & Lewenstein, M. Feynman’s path-integral approach for intense-laser-atom interactions. *Science* **292**, 902–905 (2001).
- [87] Popov, V. S. Imaginary-time method in quantum mechanics and field theory. *Physics of Atomic Nuclei* **68**, 686–708 (2005).
- [88] Chirilă, C. C. & Lein, M. High-order above-threshold ionization in stretched molecules. *Phys. Rev. A* **74**, 051401 (2006).
- [89] Smirnova, O. & Ivanov, M. Y. Multielectron High Harmonic Generation: simple man on a complex plane (2013). To appear in Vrakking, M. & Schulz, T. (eds.) *Attosecond and XUV science*, preprint at arXiv:1304.2413v1.
- [90] Sansone, G., Vozzi, C., Stagira, S. & Nisoli, M. Nonadiabatic quantum path analysis of high-order harmonic generation: Role of the carrier-envelope phase on short and long paths. *Phys. Rev. A* **70**, 013411 (2004).
- [91] Soifer, H., Dagan, M., Shafir, D., Bruner, B. D., Ivanov, M. Y., Serbinenko, V., Barth, I., Smirnova, O. & Dudovich, N. Spatio-spectral analysis of ionization times in high-harmonic generation. *Chem. Phys.* **414**, 176–183 (2013).
- [92] Kawano, H. Effective work functions for ionic and electronic emissions from mono- and polycrystalline surfaces. *Progr. Surf. Sci.* **83**, 1–165 (2008).
- [93] Figueira de Morisson Faria, C., Schomerus, H. & Becker, W. High-order above-threshold ionization: The uniform approximation and the effect of the binding potential. *Phys. Rev. A* **66**, 043413 (2002).
- [94] Arbó, D. G., Persson, E. & Burgdörfer, J. Time double-slit interferences in strong-field tunneling ionization. *Phys. Rev. A* **74**, 063407 (2006).
- [95] Moshinsky, M. Diffraction in time. *Phys. Rev.* **88**, 625–631 (1952).
- [96] Paulus, G. G. & Bauer, D. Double-slit experiments in the time domain. *Lect. Notes Phys.* **789**, 303–339 (2009).
- [97] Schumacher, D. W., Weihe, F., Muller, H. G. & Bucksbaum, P. H. Phase dependence of intense field ionization: A study using two colors. *Phys. Rev. Lett.* **73**, 1344–1347 (1994).
- [98] Paulus, G. G., Lindner, F., Walther, H., Baltuška, A., Goulielmakis, E., Lezius, M. & Krausz, F. Measurement of the phase of few-cycle laser pulses. *Phys. Rev. Lett.* **91**, 253004 (2003).

- [99] Busuladžić, M., Gazibegović-Busuladžić, A. & Milošević, D. B. High-order above-threshold ionization in a laser field: Influence of the ionization potential on the high-energy cutoff. *Las. Phys.* **16**, 289–293 (2006).
- [100] Lai, X. Y., Quan, W. & Liu, X. Tunneling-induced shift of the cutoff law for high-order above-threshold ionization. *Phys. Rev. A* **84**, 025401 (2011).
- [101] Hickstein, D. D., Ranitovic, P., Witte, S., Tong, X.-M., Huismans, Y., Arpin, P., Zhou, X., Keister, K. E., Hogle, C. W., Zhang, B., Ding, C., Johnsson, P., Toshima, N., Vrakking, M. J. J., Murnane, M. M. & Kapteyn, H. C. Direct visualization of laser-driven electron multiple scattering and tunneling distance in strong-field ionization. *Phys. Rev. Lett.* **109**, 073004 (2012).
- [102] Zherebtsov, S., Fennel, T., Plenge, J., Antonsson, E., Znakovskaya, I., Wirth, A., Herrwerth, O., Süßmann, F., Peltz, C., Ahmad, I., Trushin, S., Pervak, V., Karsch, S., Vrakking, M., Langer, B., Graf, C., Stockman, M., Krausz, F., Rühl, E. & Kling, M. F. Controlled near-field enhanced electron acceleration from dielectric nanospheres with intense few-cycle laser fields. *Nat. Phys.* **7**, 656–662 (2011).
- [103] Crank, J. & Nicolson, P. A practical method for numerical evaluation of solutions of partial differential equations of the heat-conduction type. *Advances in Computational Mathematics* **6**, 207–226 (1996).
- [104] Press, W. H., Teukolsky, S. A., Vetterling, W. T. & Flannery, B. P. *Numerical Recipes: The Art of Scientific Computing, Third Edition* (Cambridge University Press, Cambridge, 2007).
- [105] Kang, D. & Won, E. Precise numerical solutions of potential problems using the Crank–Nicolson method. *Journal of Computational Physics* **227**, 2970–2976 (2008).
- [106] Ohwaki, T., Ishida, H. & Liebsch, A. First-principles calculation of field emission from metal surfaces. *Phys. Rev. B* **68**, 155422 (2003).
- [107] Runge, E. & Gross, E. K. U. Density-functional theory for time-dependent systems. *Phys. Rev. Lett.* **52**, 997–1000 (1984).
- [108] Maitra, N. T., Burke, K., Appel, H., Gross, E. K. U. & van Leeuwen, R. Ten Topical Questions in Time Dependent Density Functional Theory. In Sen, K. D. (ed.) *A celebration of the contributions of Robert Parr*, 1186–1225 (World Scientific, Singapore, 2002).
- [109] Wachter, G. (2011). Unpublished manuscript.
- [110] Novotny, L. & van Hulst, N. Antennas for light. *Nat. Phot.* **5**, 83–90 (2011).
- [111] Martin, Y. C., Hamann, H. F. & Wickramasinghe, H. K. Strength of the electric field in apertureless near-field optical microscopy. *J. Appl. Phys.* **89**, 5774–5778 (2001).

- [112] Novotny, L. & Stranick, S. J. Near-field optical microscopy and spectroscopy with pointed probes. *Annual Review of Physical Chemistry* **57**, 303–331 (2006).
- [113] Hartschuh, A. Tip-enhanced near-field optical microscopy. *Angewandte Chemie International Edition* **47**, 8178–8191 (2008).
- [114] Stöckle, R. M., Suh, Y. D., Deckert, V. & Zenobi, R. Nanoscale chemical analysis by tip-enhanced Raman spectroscopy. *Chem. Phys. Lett.* **318**, 131–136 (2000).
- [115] Thomas, S. *Electric Field Enhancement and Strong-Field Effects at Sharp Metal Tips Investigated with Few-Cycle Pulses from an Erbium-Doped Fiber Laser*. Master's thesis, Technische Universität München (2011).
- [116] Taflove, A. & Hagness, S. *Computational Electrodynamics: the Finite-Difference Time-Domain Method*. Artech House antennas and propagation library (Artech House, 2005).
- [117] Yabana, K., Sugiyama, T., Shinohara, Y., Otobe, T. & Bertsch, G. F. Time-dependent density functional theory for strong electromagnetic fields in crystalline solids. *Phys. Rev. B* **85**, 045134 (2012).
- [118] Krüger, M. *Laser-Triggered Electron Emission From Tungsten Tips*. Master's thesis, Ludwig-Maximilians-Universität München (2009).
- [119] Schenk, M. *Starkfeldeffekte und Attosekundendynamik in Photoemission von Metallnanospitzen*. Ph.D. thesis, Ludwig-Maximilians-Universität München (2012).
- [120] Foreman, S. M. Useful relations for optical fields Gaussian in space and time (2008). Unpublished.
- [121] Udem, T., Holzwarth, R. & Hänsch, T. W. Optical frequency metrology. *Nature* **416**, 233–237 (2002).
- [122] Fuji, T., Rauschenberger, J., Apolonski, A., Yakovlev, V. S., Tempea, G., Udem, T., Gohle, C., Hänsch, T. W., Lehnert, W., Scherer, M. & Krausz, F. Monolithic carrier-envelope phase-stabilization scheme. *Optics Lett.* **30**, 332–334 (2005).
- [123] Savitzky, A. & Golay, M. J. E. Smoothing and differentiation of data by simplified least squares procedures. *Analytical Chemistry* **36**, 1627–1639 (1964).
- [124] Young, R. D. Theoretical total-energy distribution of field-emitted electrons. *Phys. Rev.* **113**, 110–114 (1959).
- [125] Klein, M. & Schwitzgebel, G. An improved lamellae drop-off technique for sharp tip preparation in scanning tunneling microscopy. *Rev. Sci. Instr.* **68**, 3099–3103 (1997).
- [126] Lopesa, M., Toury, T., de La Chapelle, M. L., Bonaccorso, F. & Gucciardi, P. G. Fast and reliable fabrication of gold tips with sub-50 nm radius of curvature for tip-enhanced Raman spectroscopy. *Rev. Sci. Instr.* **84**, 073702 (2013).

- [127] Eisele, M., Krüger, M., Schenk, M., Ziegler, A. & Hommelhoff, P. Note: Production of sharp gold tips with high surface quality. *Rev. Sci. Instr.* **82**, 026101 (2011).
- [128] Lucier, A.-S. *Preparation and Characterization of Tungsten Tips Suitable for Molecular Electronics Studies*. Master's thesis, Center for the physics of materials, McGill University (2004).
- [129] Gomer, R. *Field Emission and Field Ionization* (Harvard University Press, Cambridge, Massachusetts, 1961).
- [130] Tsong, T. T. *Atom-probe field ion microscopy* (Cambridge University Press, Cambridge, 1990).
- [131] Müller, E. W. & Tsong, T. T. *Field Ion Microscopy* (American Elsevier Publishing Company, Inc., New York, 1969).
- [132] Murphy, E. L. & Good, R. H. Thermionic emission, field emission, and the transition region. *Phys. Rev.* **102**, 1464–1473 (1956).
- [133] Fursey, G. *Field Emission in Vacuum Microelectronics* (Kluwer Academic/Plenum, New York, 2005).
- [134] Forbes, R. G. Simple good approximations for the special elliptic functions in standard Fowler-Nordheim tunneling theory for a Schottky-Nordheim barrier. *Appl. Phys. Lett.* **89**, 113122 (2006).
- [135] Binh, V. T., Garcia, N. & Purcell, S. T. Electron field emission from atom-sources: Fabrication, properties, and application of nanotips. *Adv. Imag. Elect. Phys.* **95**, 63–153 (1996).
- [136] Yanagisawa, H., Hafner, C., Doná, P., Klöckner, M., Leuenberger, D., Greber, T., Hengsberger, M. & Osterwalder, J. Optical control of field-emission sites by femtosecond laser pulses. *Phys. Rev. Lett.* **103**, 257603 (2009).
- [137] Schottky, W. Über den Einfluß von Strukturwirkungen, besonders der Thomson'schen Bildkraft, auf die Elektronenemission der Metalle. *Physikalische Zeitschrift* **15**, 872–878 (1914).
- [138] Plummer, E. W. & Gadzuk, J. W. Surface states on tungsten. *Phys. Rev. Lett.* **25**, 1493–1495 (1970).
- [139] Yamamoto, S., Saitou, N. & Fukuhara, S. Field emission current instability induced by migrating atoms on W(310) surface. *Surf. Sci.* **71**, 191–198 (1978).
- [140] Christensen, N. E. & Feuerbacher, B. Volume and surface photoemission from tungsten. I. Calculation of band structure and emission spectra. *Phys. Rev. B* **10**, 2349 (1974).
- [141] Saathoff, G., Miaja-Avila, L., Aeschlimann, M., Murnane, M. M. & Kapteyn, H. C. Laser-assisted photoemission from surfaces. *Phys. Rev. A* **77**, 022903 (2008).

- [142] Yalunin, S. V., Herink, G., Solli, D. R., Krüger, M., Hommelhoff, P., Diehn, M., Munk, A. & Ropers, C. Field localization and rescattering in tip-enhanced photoemission. *Annalen der Physik* **525**, L12–L18 (2013).
- [143] Bao, M.-Q. & Starace, A. F. Static-electric-field effects on high harmonic generation. *Phys. Rev. A* **53**, R3723–R3726 (1996).
- [144] Lohr, A., Becker, W. & Kleber, M. High-harmonic generation affected by a static electric field. *Las. Phys.* **7**, 615–622 (1997).
- [145] Odžak, S. & Milošević, D. B. High-order harmonic generation in the presence of a static electric field. *Phys. Rev. A* **72**, 033407 (2005).
- [146] Popov, V. Energy and angular distributions of photoelectrons in multiphoton ionization. *JETP Lett.* **70**, 502–507 (1999).
- [147] Schätzel, M. G. *Mehrphotonen-Ionisationsprozesse mit intensiven Laserpulsen*. Ph.D. thesis, Ludwig-Maximilians-Universität München (2006).
- [148] Gazibegović-Busuladžić, A., Milošević, D. B., Becker, W., Bergues, B., Hultgren, H. & Kiyani, I. Y. Electron rescattering in above-threshold photodetachment of negative ions. *Phys. Rev. Lett.* **104**, 103004 (2010).
- [149] Yanagisawa, H., Hafner, C., Doná, P., Klöckner, M., Leuenberger, D., Greber, T., Osterwalder, J. & Hengsberger, M. Laser-induced field emission from a tungsten tip: Optical control of emission sites and the emission process. *Phys. Rev. B* **81**, 115429 (2010).
- [150] Neacsu, C. C., Reider, G. A. & Raschke, M. B. Second-harmonic generation from nanoscopic metal tips: Symmetry selection rules for single asymmetric nanostructures. *Phys. Rev. B* **71**, 201402 (2005).
- [151] Bouhelier, A., Beversluis, M., Hartschuh, A. & Novotny, L. Near-field second-harmonic generation induced by local field enhancement. *Phys. Rev. Lett.* **90**, 013903 (2003).
- [152] Zhang, W., Cui, X. & Martin, O. J. F. Local field enhancement of an infinite conical metal tip illuminated by a focused beam. *Journal of Raman Spectroscopy* **40**, 1338–1342 (2009).
- [153] Ghimire, S., DiChiara, A. D., Sistrunk, E., Agostini, P., DiMauro, L. F. & Reis, D. A. Observation of high-order harmonic generation in a bulk crystal. *Nat. Phys.* **7**, 138–141 (2010).
- [154] Zuloaga, J., Prodan, E. & Nordlander, P. Quantum plasmonics: Optical properties and tunability of metallic nanorods. *ACS Nano* **4**, 5269–5276 (2010).
- [155] Marinica, D., Kazansky, A., Nordlander, P., Aizpurua, J. & Borisov, A. G. Quantum plasmonics: Nonlinear effects in the field enhancement of a plasmonic nanoparticle dimer. *Nano Lett.* **12**, 1333–1339 (2012).

- [156] Ciraci, C., Hill, R. T., Mock, J. J., Urzhumov, Y., Fernández-Domínguez, A. I., Maier, S. A., Pendry, J. B., Chilkoti, A. & Smith, D. R. Probing the ultimate limits of plasmonic enhancement. *Science* **337**, 1072–1074 (2012).
- [157] Paulus, G. G., Grasbon, F., Walther, H., Villoresi, P., Nisoli, M., Stagira, S., Priori, E. & Silvestri, S. D. Absolute-phase phenomena in photoionization with few-cycle laser pulses. *Nature* **414**, 182–184 (2001).
- [158] Kling, M. F., Siedschlag, C., Verhoef, A. J., Khan, J. I., Schultze, M., Uphues, T., Ni, Y. F., Uiberacker, M., Drescher, M., Krausz, F. & Vrakking, M. J. J. Control of electron localization in molecular dissociation. *Science* **312**, 246–248 (2006).
- [159] Apolonski, A., Dombi, P., Paulus, G. G., Kakehata, M., Holzwarth, R., Udem, T., Lemell, C., Torizuka, K., Burgdörfer, J., Hänsch, T. W. & Krausz, F. Observation of light-phase-sensitive photoemission from a metal. *Phys. Rev. Lett.* **92**, 073902 (2004).
- [160] Ott, C., Schönwald, M., Raith, P., Kaldun, A., Sansone, G., Krüger, M., Hommelhoff, P., Patil, Y., Zhang, Y., Meyer, K., Laux, M. & Pfeifer, T. Strong-field spectral interferometry using the carrier-envelope phase. *New J. Phys.* **15**, 073031 (2013).
- [161] Xu, L., Spielmann, C., Poppe, A., Brabec, T., Krausz, F. & Hänsch, T. W. Route to phase control of ultrashort light pulses. *Optics Lett.* **21**, 2008–2010 (1996).
- [162] Lemell, C., Tong, X.-M., Krausz, F. & Burgdörfer, J. Electron emission from metal surfaces by ultrashort pulses: Determination of the carrier-envelope phase. *Phys. Rev. Lett.* **90**, 076403 (2003).
- [163] Stockman, M. I. & Hewageegana, P. Absolute phase effect in ultrafast optical responses of metal nanostructures. *Appl. Phys. A* **89**, 247–250 (2007).
- [164] Davisson, C. & Germer, L. H. Diffraction of electrons by a crystal of nickel. *Phys. Rev.* **30**, 705–740 (1927).
- [165] Jönsson, C. Elektroneninterferenzen an mehreren künstlich hergestellten Feinspalten. *Zeitschrift für Physik* **161**, 454–474 (1961).
- [166] Hasselbach, F. Progress in electron- and ion-interferometry. *Rep. Progr. Phys.* **73**, 016101 (2010).
- [167] Brukner, Č. & Zeilinger, A. Diffraction of matter waves in space and in time. *Phys. Rev. A* **56**, 3804–3824 (1997).
- [168] Szriftgiser, P., Guéry-Odelin, D., Arndt, M. & Dalibard, J. Atomic wave diffraction and interference using temporal slits. *Phys. Rev. Lett.* **77**, 4–7 (1996).
- [169] Hils, T., Felber, J., Gähler, R., Gläser, W., Golub, R., Habicht, K. & Wille, P. Matter-wave optics in the time domain: Results of a cold-neutron experiment. *Phys. Rev. A* **58**, 4784–4790 (1998).

- [170] Haslinger, P., Dörre, N., Geyer, P., Rodewald, J., Nimmrichter, S. & Arndt, M. A universal matter-wave interferometer with optical ionization gratings in the time domain. *Nat. Phys.* **9**, 144–148 (2013).
- [171] Lindner, F., Schätzel, M. G., Walther, H., Baltuška, A., Goulielmakis, E., Krausz, F., Milošević, D. B., Bauer, D., Becker, W. & Paulus, G. G. Attosecond double-slit experiment. *Phys. Rev. Lett.* **95**, 040401 (2005).
- [172] Mitrofanov, A. V., Verhoef, A. J., Serebryannikov, E. E., Lumeau, J., Glebov, L., Zheltikov, A. M. & Baltuška, A. Optical detection of attosecond ionization induced by a few-cycle laser field in a transparent dielectric material. *Phys. Rev. Lett.* **106**, 147401 (2011).
- [173] Ivanov, M. Y. (2011). Private communication.
- [174] Herink, G., Solli, D. R., Gulde, M. & Ropers, C. Field-driven photoemission from nanostructures quenches the quiver motion. *Nature* **483**, 190–193 (2012).
- [175] Homann, C., Bradler, M., Förster, M., Hommelhoff, P. & Riedle, E. Carrier-envelope phase stable sub-two-cycle pulses tunable around $1.8\ \mu\text{m}$ at 100 kHz. *Optics Lett.* **37**, 1673–1675 (2012).
- [176] Thomas, S., Holzwarth, R. & Hommelhoff, P. Generating few-cycle pulses for nanoscale photoemission easily with an erbium-doped fiber laser. *Optics Expr.* **20**, 13663–13668 (2012).
- [177] Schumacher, D. W., Weihe, F., Muller, H. G. & Bucksbaum, P. H. Phase dependence of intense field ionization: A study using two colors. *Phys. Rev. Lett.* **73**, 1344–1347 (1994).
- [178] Wirth, A., Hassan, M. T., Grguraš, I., Gagnon, J., Moulet, A., Luu, T., Pabst, S., Santra, R., Alahmed, Z. A., Azzeer, A. M., Yakovlev, V. S., Pervak, V., Krausz, F. & Goulielmakis, E. Synthesized light transients. *Science* **334**, 195–200 (2011).
- [179] Dombi, P., Hörl, A., Rácz, P., Marton, I., Trügler, A., Krenn, J. R. & Hohenester, U. Ultrafast strong-field photoemission from plasmonic nanoparticles. *Nano. Lett.* **13**, 674–678 (2013).
- [180] Niikura, H., Légère, F., Hasbani, R., Bandrauk, A. D., Ivanov, M. Y., Villeneuve, D. M. & Corkum, P. B. Sub-laser-cycle electron pulses for probing molecular dynamics. *Nature* **417**, 917–922 (2002).

Danksagung

Einer der schönsten und meistgelesenen Abschnitte einer Doktorarbeit ist die Danksagung. Forschung lebt nicht in erster Linie von Apparaturen und Maschinen oder von Formeln und Fachwissen, sondern von Menschen, die dahinter stehen. Bevor ich nun aber zu den Menschen komme, möchte ich an allererster Stelle Gott danken, der mir täglich neu begegnet und mein Leben mit so viel Gutem erfüllt. Ohne ihn und seine Treue wäre ich nie bis hierher gekommen und hätte so manche schwierige Situation nicht überstanden. Mit Freude blicke ich zurück auf den weiten Weg, den ich mit ihm schon zurückgelegt habe, und schaue voll Zuversicht auf das, was kommt. Maranatha.

Bei den Menschen steht an erster Stelle mein Betreuer Peter Hommelhoff, der mir nicht nur diese Doktorarbeit, sondern auch schon die vorausgegangene Diplomarbeit ermöglicht hat. Das Vertrauen, das er mir in letzten fünf Jahren entgegengebracht hat, und seine offene und unkomplizierte Art sind keineswegs selbstverständlich. Seine Begeisterung für Physik, für Kreativität und neue Ideen haben mich sehr ermutigt und angesteckt.

Großer Dank gilt natürlich auch allen gegenwärtigen und ehemaligen Mitgliedern der Hommelhoff-Gruppe. Hier möchte ich mich zuerst bei Markus Schenk bedanken, dem "Spitzenforscher" der ersten Stunde. Mit ihm war die Zusammenarbeit, die fast den gesamten Inhalt dieser Doktorarbeit umfasst, ungewöhnlich fruchtbar und hat sehr viel Spaß gemacht. Auch Johannes Hoffrogge bin ich zu viel Dank verpflichtet. Er hat auf indirektem Wege mir und der ganzen Gruppe mit Rat und Tat sehr unter die Arme gegriffen. Ähnliches gilt auch für John Breuer, der nun endlich sein schwieriges Experiment mehr als gemeistert hat.

Michael "Michi" Förster hat schon vor einiger Zeit sich dem Team angeschlossen und forscht nun auch an Photoemission an Spitzen. Ihm danke ich für die unermüdliche Unterstützung vor allem in letzter Zeit, z.B. bei der Massenfabrikation von Metallspitzen. Sebastian Thomas darf auch nicht unerwähnt bleiben, der nicht zuletzt durch seine Maxwell-Simulationen wesentlich zu dieser Arbeit beigetragen hat.

Jakob Hammer, der nun die spannenden Experimente mit den Mikrofallen für Elektronen fortsetzt, danke ich für seine Unterstützung. Zu einem guten Atmosphäre in der Gruppe haben auch Takuya Higuchi, Péter Dombi, Anoush Aghajani-Talesh, Dominik Ehberger, Stephan Heinrich, Sebnem Tuncay, Alexander Lang, Andreas Liehl, Alexander Hirler, Lothar Maisenbacher, Jan-Paul Stein, Konstantin Holzner, Tobias Sattler, Roman Fröhlich, Max Eisele, Hanno Kaupp und viele andere beigetragen. Ohne die Unterstützung der Techniker Charlie Linner und Wolfgang Simon und dem Elektroniker Helmut Brückner wäre meine Arbeit gar nicht möglich gewesen. Ihnen und allen Mitgliedern der Hänsch-Gruppe danke ich für interessante, inspirierende und vor allem auch lustige fünf Jahre am MPQ. Die einzigartige Atmosphäre am Institut hat mich sehr geprägt.

Außerhalb des MPQs geht mein Dank zunächst nach Wien zu den Theoretikern Georg Wachter und Christoph Lemell in der Gruppe von Joachim Burgdörfer, die uns sehr stark unterstützt haben. Aus ihrer Feder stammt u.a. das Modell, das auf der zeitabhängigen Dichtefunktionaltheorie aufbaut. Matthias Kling, Misha Ivanov und unbekannterweise auch Fabrizio Lindner danke ich für das Verständnis von Starkfeldphysik, das ich durch ihre Arbeiten gewinnen konnte. Christian Ott und Thomas Pfeifer und seine ganze Gruppe am Max-Planck-Institut für Kernphysik in Heidelberg haben einen nicht unwesentlichen Teil dieser Arbeit inspiriert. Schlaflose Nächte in einem fensterlosen Labor an der Universität Jena haben mich mit Dominik Hoff vom Lehrstuhl Paulus und auch mit dem oben schon erwähnten Lothar Maisenbacher verbunden. Die harte Arbeit zusammen mit den beiden Physikern an meinem "Zweitwohnsitz" Jena (wie manche schon meinten) hat sich am Ende Gott sei Dank doch ausgezahlt.

Ein großes Dankeschön richte ich an meine Freunde und Geschwister, die ihr – ob nah oder fern – mir zur Seite gestanden seid. In München geht mein Dank an meine Mitbewohner und an die vielen Geschwister in meiner Gemeinde und meinem Hauskreis und dem Montagsgebetstreffen und anderswo. Yvonne, Tabea, Benedikt und Hannah, Friedrich und Sandra, Dorit, Eva, Lena, Heide und Lothar, Elke, Casey und viele andere haben mich mit Gebet und Tat unterstützt und mich durch diese Zeit getragen. Auch meine ehemaligen Kommilitonen Markus, Rhea, Bässem und Caro möchte ich nicht missen. Aus der Ferne haben mich Daniel, Fabian, Martina, Luci und Ivan, Andrea, Maria N., Mária F., Elina, Przemek, Frania und einige andere unterstützt und mit mir und meiner Arbeit mitgefiebert. Möge Gott euch alles reichlich vergelten.

Zu guter Letzt möchte ich meinen Eltern und meiner ganzen Familie von Herzen ein großes Danke sagen; eure Liebe, eure Unterstützung und auch eure Geduld ist mit nichts aufzuwiegen.

Danke! – Thank you! – Dzięk!